UNIVERSITY
OF TRENTO - Italy

Department of Materials Engineering
and Industrial Technologies

XXVI cycle

Doctoral School in Materials Science and Engineering

Dry sliding and contact fatigue behavior of different high density Ni-Cu-Mo PM Steels

Ibrahim Metinöz

June 2014

Dry sliding and contact fatigue behavior of different high density Ni-Cu-Mo PM Steels

Ibrahim Metinöz

(ibrahimmetinoz@hotmail.com)

Tutors:

Prof. Ilaria Cristofolini

Department of Industrial Engineering

University of Trento, Italy

Prof. Alberto Molinari

Department of Industrial Engineering

University of Trento, Italy

PhD Commission:

Prof. Vincenzo Sglavo

Department of Industrial Engineering

University of Trento, Italy

Prof. Rajesh Prasad

Department of Applied Mechanics

Indian Institute of Technology New Delhi, India

Prof. Lorella Ceschini

Department of Industrial Engineering

University of Bologna, Italy

To my family

**University of Trento - Department of
Industrial Engineering**

Doctoral Thesis

**Ibrahim Metinöz- 2014
Published in Trento (Italy) – by University of Trento**

ISBN:

Table of Contents

1. Introduction

Powder metallurgy (PM) is a net shape and cost effective technology used for the production of steel parts having good mechanical properties and excellent dimensional and geometrical precision. This technology allows to produce parts with geometrical features required by many different applications without any need of post sintering operations regarding to the dimensional and geometrical features. Even in the cases where additional operations such as machining or sizing are required, because of its cost effectiveness PM technology is the first option considered for production, when the size and the shape of the parts is compatible with the compaction limitations.

In the past years, the mechanical properties of PM steels were not as good as wrought steels because of the remaining residual porosity after conventional press and sinter process. However, deep and continuous research has been done to improve the mechanical properties up to the level of the corresponding wrought steels. This continuous development in PM is supported by new powders, innovative compaction and sintering processes, new furnaces etc. These improvements have made PM a reliable and technically competitive technology.

By combining good mechanical properties and geometrical precision, PM technology has started to play a key role in the production of special parts for important industries such as automotive and aerospace.

The usage of PM steels in these industries, claims for continuous efforts in research and development. For this purpose, the world biggest part manufacturer, GKN Sinter Metals and the Department of Industrial Engineering of University of Trento started a cooperation to investigate the wear and contact fatigue properties of PM steels.

Wear is one of the most important factors that limit the life of engineering components in different ways. In this research two very common phenomena, dry sliding and contact fatigue behavior of PM parts have been investigated.

In the first part of the work dry sliding behavior of one Fe-Mo-Cu-C and three Fe-Mo-Cu-Ni-C steels was investigated. The study was made firstly on two steels differing for the presence of nickel (Ni), which leads to the formation in the sinter-hardened microstructure of a Ni-rich constituent, softer than martensite and bainite. This Ni-rich constituent is expected to decrease wear resistance somehow, due to a localized plastic deformation which reduces the load bearing capacity of the surface. Once the effect of the presence of Ni has been assessed, in the second part of the work dry sliding wear resistance of two Ni-alloyed sintered steels, differing for Ni content, was investigated to highlight any effect due to the amount of this alloying element.

The design approach for parts subject to dry sliding wear is frequently empirical, based on hardness. However, such an approach does not consider the influence of the microstructural peculiarities of sintered steels, i.e. porosity and inhomogeneous microstructures, which affect the contact stresses and the mechanical properties of the material. Based on experimental results, a procedure for the design of dry sliding wear resistant parts was proposed. Following the classical approach of functional design, the case of dry rolling-sliding was used as the basis for the design criteria developed for the case of PM parts subject to dry sliding wear. A failure criterion is defined and the performance of parts in different load and sliding speed conditions is evaluated, considering a hypothesized working life. The effect of hardness (material parameter) and contact length (geometrical parameter) was also evaluated.

In the second part of the work the contact fatigue behavior of three different steels was investigated.. The aim was the proposal of a conservative approach to predict the contact fatigue behavior of different sintered and heat treated steels, based on the nucleation of the fatigue crack. It is based on the assumption that the nucleation of fatigue cracks is anticipated by the local plastic deformation of the material, so that, in absence of such a deformation, the fatigue cracks will not nucleate. This approach can be considered a conservative approach, since it does not consider the eventuality that crack does not propagate to predict safe working conditions; it focuses the attention on crack nucleation. Plastic deformation occurs when the maximum local stress exceeds the yield strength of the matrix. The model is developed by calculating the maximum local stress from the theory of the elastic contact and the matrix yield strength from the microhardness of the steels, under different mean Hertzian pressures.

The microstructure of the investigated steels, resulting from the powders used for their production, is heterogeneous and such an inhomogeneity influences the mechanical resistance. Therefore in this study the model was developed by considering the mean properties of the steels (average approach) and the properties of the single microstructural constituents where the large pores, responsible for the nucleation of the contact fatigue crack, are localized (local approach). The results of theoretical predictions were validated through rolling-sliding tests.

In the last part of the work the effect of shot peening on contact fatigue behavior was investigated. The same three materials that were used to investigate contact fatigue behavior were taken into consideration. Two different types of shot peening, ceramic or steel+ceramic, were considered. Stress and strength calculations were made based on the local approach on contact fatigue, which was validated in the second part of the work.

2. Scientific Context

2.1 Wear

Wear is one of the main damage mechanisms limiting the life and performance of engineering components and systems. Wear occurs when the surfaces of components are subject to sliding and/or rolling motion under the application of a contact force [1].

All engineering surfaces are rough and wear takes place through a change in their profiles. Roughness is an important characteristic of engineering surfaces, since when two parts are in contact they touch only over a very small part of their apparent area of contact. By time, wear is progressive in that it increases with usage or increasing motion, and as a result of this, wearing action results in material lost, displacement or damage [2].

Wear occurs with different mechanisms and processes. Therefore, there are different types of classification of wear regarding to the various forms. Different methods can be used to categorize a wear process such as:

- lubricated wear and unlubricated wear

- severe wear and mild wear

- sliding wear, rolling contact wear and impact wear [3]

All wear processes involve either one or a combination of wear mechanisms.

There are four main wear mechanisms: adhesive, abrasive, surface fatigue and oxidative wear [4,5].

Adhesive or adhesion wear is a type of wear occurring when two surfaces adhere to each other through the welding of the asperities in contact. When the two surfaces move relatively each other, wear occurs by the pulling out of material from one of the two surfaces, due to the fracture of the welds.

Abrasive wear occurs when hard particles or protuberances are forced against a moving surface and produce a groove, scratch or indentation.

Surface fatigue occurs when a cyclic contact between surfaces is accompanied by high local stresses; after a large number of either pure rolling or rolling-sliding contacts, cracks nucleate and propagate to form a loose particle.

Oxidative wear is the wear of dry unlubricated metals in presence of oxygen. In this type of wear, a surface layer of a chemically reacted species is formed, such as iron oxide, and then wear occurs by one of the three other mechanisms either in reacted layer or at the interface between the layer and the parent material. The wear rate is influenced, and possibly controlled, by the growth and the stability of that layer. [4]

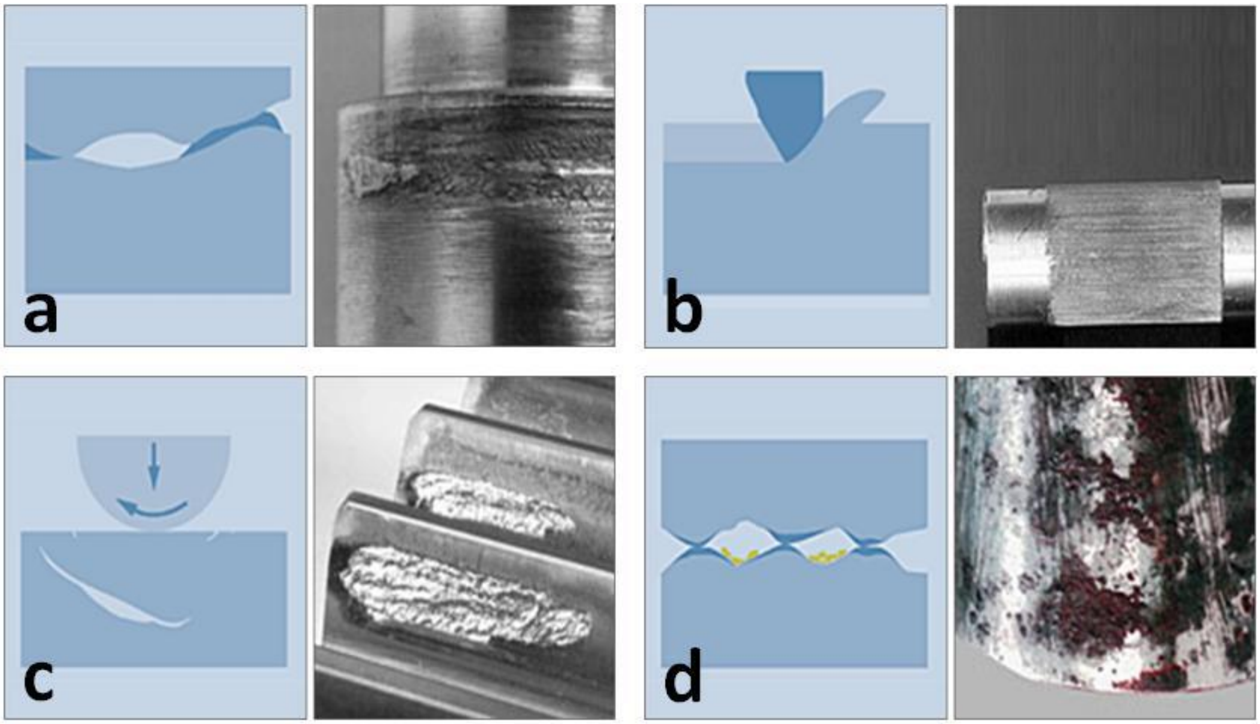

Figure 2.1.1. Wear mechanisms: a) Adhesive Wear, b) Abrasive Wear, c) Surface Fatigue and d) Oxidative Wear [6]

In applications that are subject to wear, the knowledge of the wear mechanism taking place under the working conditions is of a great importance, in order to predict the life of the components. It is also important to know the key working conditions in order to keep wear rate under safe limits.

There are many key working conditions related to wear such as time, load, velocity, temperature and film thickness [1].

Time can also be thought as the working life of the component and it has a great importance for the operations. In usual process where wear occurs, a "run in" occurs initially with a high wear rate. As the contact area grows and the surface finish is modified by run-in wear, the wear rate decreases to a steady value. After operating for a given period of time, wear rate increases. This transition can be attributed to a number of causes such as a change in the type of wear, the increase in the surface temperature above a critical value, the lubricant contamination.

Another key parameter which affects wear is the load applied to the system. All engineering components facing wear are working under an either constant or a varying load. As load increases, the wear rate may either decrease or increase in unlubricated bearings. The frictional heat may favor the formation of a stable oxide layer, promoting a severe-to-mild wear transition. Alternatively, it may soften the material and/or cause the surface oxide to breakdown, giving rise to a mild-to-severe transition. In case of lubricated contacts, the increase in load tends to enhance wear.

Velocity is another important factor for components such as gears and cams. With reference to phenomena correlated to frictional heat, the effect of an increasing velocity is similar to that of an increased load, and the two transitions above described may be observed in dry sliding contacts. On the other hand, in lubricated wear, lubricant with proper additives will decrease wear rate, until a limit temperature is reached, where the lubricant no longer completely separates the surfaces; moreover, the increased number of cycles at higher velocity causes a transition to a fatigue type wear.

Temperature is another key factor in working conditions when wear is considered. For example, for an unlubricated bearing, the wear rates are usually constant, but if temperature rises to a critical temperature, material softens and wear rate increases dramatically. This is the same transition, which occurs when the load and velocity increase, and cause an increase in the temperature due to frictional heat.

In lubricated wear, the increase in the temperature will cause a transition to a boundary lubrication because of the viscosity decrease, causing a decrease in the film thickness. Further increase will cause an unlubricated sliding as the lubricant fails due to desorption, melting, decomposition etc [7].

Figure 2.1.2 illustrates how wear rate behaves regarding to the change in time, load, velocity, temperature and the film thickness. The figure does not contemplate the possible decrease of wear rate due to the severe-to-mild wear transition when load is increased. Such a transition, indeed, occurs in the low load ranges.

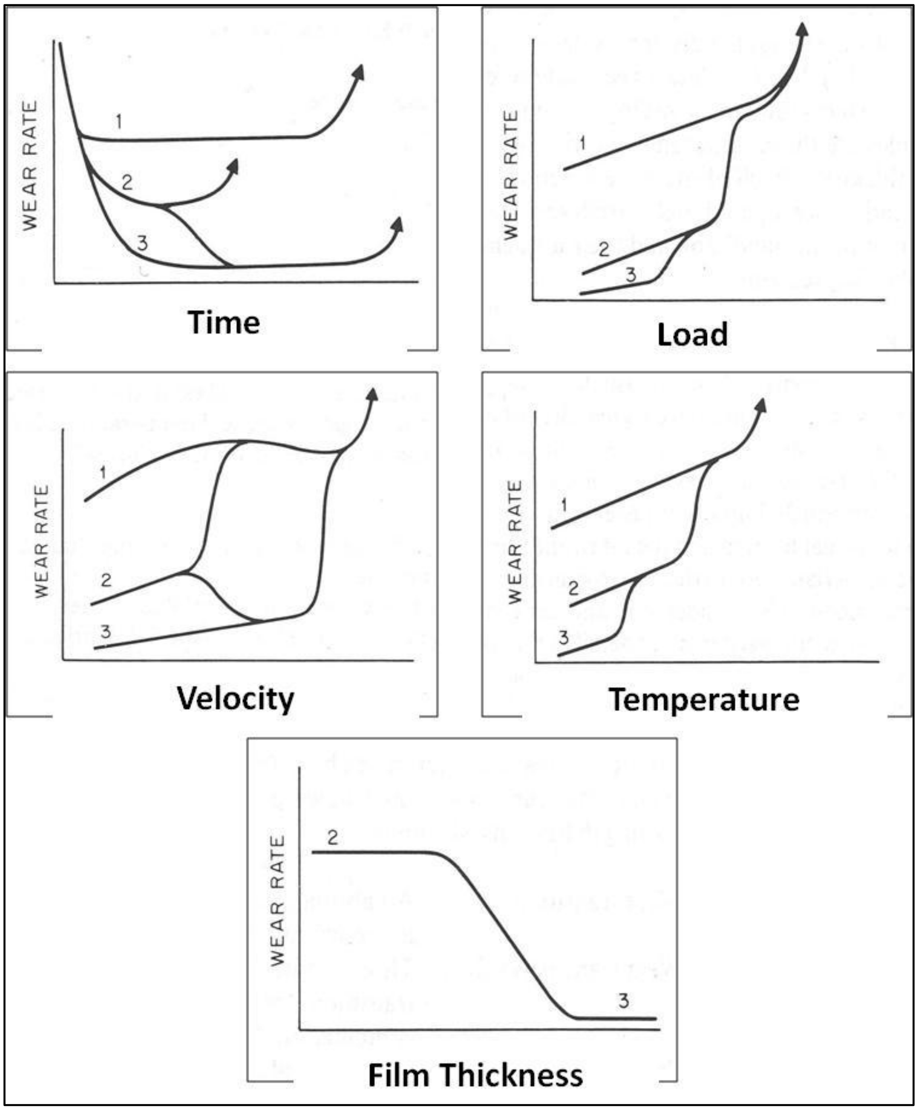

Figure 2.1.2. Wear rate vs. Time, load, velocity, temperature and film thickness [1]

In addition to the wear mechanisms and the key factors to control wear rate, other parameters have to be considered. They are related to the chemical composition and roughness of the materials, lubricant properties and humidity.

The selection of appropriate materials for the type of wear being engaged is important for effective wear control. The selection of the material should be made carefully, by knowing the properties and by considering its performances under similar conditions [8].

Surface finishing is also very important, especially when soft materials are working against harder materials. If the roughness of the harder material is higher than that of the softer one, the latter will be abraded easily. Sharp edges also should be avoided to prevent a failure related to undesirable contact in those regions. Another important characteristic of the surface finishing is the ability to promote the fluid film lubrication in both sliding and rolling contacts. If surface finishing of the material is improved, lubrication will be more effective and prevent the metal-to-metal contact.

Lubricant is also essential to control wear, since the main function of the lubricant is to reduce the wear. The type of lubricant has to be chosen properly with reference to its viscosity. Less flow of the lubricant between the metals can result in a metal-to-metal contact, which can cause failure of the system.

The contact area is a geometrical parameter of great importance, since it defines the contact pressure for a given contact force. On increasing the contact area, the contact pressures decrease. In principle, the different contact conditions have to be compared with reference to the contact pressure instead of the contact force. All the phenomena associated to the contact force in the previous paragraphs occur in dependence on the actual contact pressure. Under the same contact pressure, the increase in the contact area results in a smaller wear depth, since the same volume will be removed from a larger area. As another positive effect, larger areas mean greater film thickness and lower local temperatures, due to the larger sectional area for heat dissipation. However larger areas result in some negative effects, such as difficulty of uniform lubricant distribution, higher cost and larger volumes of the parts.

The alignment of the system is also decisive for wear rate. A wrongly assembled system can cause changes in load, relative velocity, temperature and effective contact area. Any change of the contact area yields a new "run in", which increases wear rate.

2.2 Dry Sliding Wear of PM materials

Many powder metallurgy (PM) parts are exposed to sliding wear in applications. These parts play an increasing role and they are expected to exhibit a good wear resistance in industries such as in automotive or aerospace where PM parts are used in heavy-duty component like gears, pistons, connecting rods or cam lobes. [9-12]

A wide literature exists on dry wear mechanisms and wear resistance of PM parts [9, 13-15, just as examples]. The effect of porosity in materials produced by the conventional PM process, i.e. cold compaction and sintering, is highlighted: porosity reduces the area of load bearing surface, increases local plastic deformation and leads to wear debris entrapment [16-18]; the global effect is the decrease of the wear resistance.

The effect of porosity on plastic deformation at the pore edges is influenced by the yield strength of the metallic matrix [19,20]. Heat treatments (through hardening, carburizing) increase wear resistance as a result of the increased hardness and improved resistance to localized damage at the pore edges.

One of the peculiarities of PM steels is the presence of a significant amount of Ni as alloying element. Ni improves ductility and toughness of steel parts. Since it forms less stable oxides than iron, sintering atmospheres, which are reducing for iron oxide, will also be reducing for Ni, thus avoiding any limitations related to the reduction of surface oxides. [21, 22]

In most cases Ni is added to the base powder by diffusion bonding, a process where very fine Ni powders are bonded to the iron particles by partial interdiffusion which involves only a very small portion of the iron particle. As a consequence, the iron powder maintains its excellent compressibility (which is generally reduced by the dissolution of alloying elements) and, on the other side, the risk of gravimetric segregation during handling and processing of the powder is fully prevented. The chemical inhomogeneity is maintained even after sintering under the common conditions of the industrial production; as a consequence, the final microstructure contains some Ni-rich austenitic regions, which are softer than the martensitic/bainitic matrix.

Due to the chemical compositions of the investigated steels in this work, they can be cold compacted to a high green density, and they can develop a hardened microstructure by sinter-hardening [23, 24] with no need of post-sintering heat treatments. In principle the high density (7.3 g/cm^3, the upper limit of cold compaction and sintering for these steels) combined with a hardened microstructure, makes these steels very attractive for the production of parts using the press and sinter method to be used in sliding wear applications.

However, the Ni-rich austenite is expected to decrease wear resistance due to a localized increase in plastic deformation and the nucleation and propagation of cracks [25-27].

The large amount of results related to dry wear of PM steels make reference to different contact conditions as a consequence of the variety of the wear tests configuration used. For this reason, it’s rather difficult to merge them within a sort of normalized knowledge system to support the designer in the selection of the material and the processes for any specific application. The classical approach of functional design [28,29], already implemented in the case of dry rolling-sliding [30,31] may be a good guideline for the design of PM parts subject to dry sliding wear.

2.3 Contact Fatigue of PM materials

PM steels may replace wrought steels in several applications such as vehicle transmission, power train gears, oil pumps, cams and rolling bearings, which involve cyclic loading. All these applications are highly demanding in terms of dimensional/geometrical precision and mechanical properties, in particular the resistance to contact fatigue. Contact fatigue is a well known failure mode for components subject to cyclic contact stresses. The contact stresses distribution in the subsurface layers causes the nucleation of a crack and its propagation under the cyclic loading, which leads to the generation of debris [32-35]. Contact fatigue behavior of porous sintered steels is being investigated since many years [36-41], and the effect of porosity, which is the peculiar microstructural characteristics of these materials, has been highlighted in several papers [42-44].

In PM materials pores behave as discontinuities in the metallic matrix. They have a major influence on the mechanical fatigue as shown, for instance, in some studies [45-47]. Fatigue crack nucleates in correspondence of the larger pores, and propagates easily through the network of interconnected porosity. Similarly to mechanical fatigue, in case of contact fatigue porosity has to be taken into account carefully.

The mechanical properties of the PM materials were mostly considered as a function of density [48, 49]. Even in the competitions between the PM material producers to conquer and replace traditionally manufactured wrought steel components with PM materials, it was considered that increased density is the only way to increase mechanical properties. This is not definitely right, since porosity characteristics, and in particular their morphology, have a significant effect on mechanical properties [50-53].

To examine porosity and the morphology of the pores some parameters should be discussed. These are total porosity, porosity distribution, pore size, pore shape; they contribute to the definition of the fraction of the load bearing section.

The total porosity is the fraction of empty space in the sample; it is one of the most frequently used parameter to characterize sintered materials [54, 55]. The most common method to measure the total porosity is the water displacement method. The fraction of the load bearing section increases on decreasing porosity.

Porosity distribution is another parameter that needs to be considered. By press and sinter method, it is not possible to have uniform pores distribution in the material due to the inhomogeneous distribution of the compaction pressure in the powder [56]. In addition to these foreseeable but ordinary pores, there are some irregular pores caused by inhomogeneous die filling or bridging during compaction. These irregularities cannot be eliminated during sintering [57]. The fraction of the load bearing section is larger in the regions with the higher porosity.

Pore size is a function of powder particle size and compacting pressure. In addition, during sintering the mean pore size may slightly grow up since the small pores tend to shrink in favor of large ones during the final stage of sintering. The fraction of the load bearing section is not significantly affected by the pore size, which instead has a direct influence on the nucleation of the fatigue crack.

Pore shape is one of the main parameters which influence the load bearing section and, in turn, the mechanical properties of the materials. Pore shape depends on the powder morphology, the compaction pressure (the higher the compaction pressure, the large the elongation of pores in the transversal direction), the sintering temperature (the higher the sintering temperature, the better the pore morphology) and on the occurrence of a liquid phase sintering mechanisms, that makes the pore profile smoother and rounded. The improvement of the pore morphology improves the fraction of the load bearing section.

In addition to porosity, other two parameters related to the matrix have to be considered, due to their influence on contact fatigue.

Yield strength is the stress at which material starts to deform plastically. When the applied stress is higher than the yield strength, it causes a damage in the material, which anticipates and causes the nucleation of the fatigue crack. It can be also considered as the maximum stress that can be applied to avoid crack initiation. [58, 59]

Elastic Modulus is the other important parameter; it affects the elastic deformation of the material and determines the extension of the contact area in case of elastic contact. It depends on porosity [60].

The microstructure of PM materials is frequently heterogeneous [61-65]. A very common heterogeneous microstructure can be seen Figure 2.3.1, where pearlitic and bainitic areas (brown) are surrounded by an almost continuous network of martensite (white).

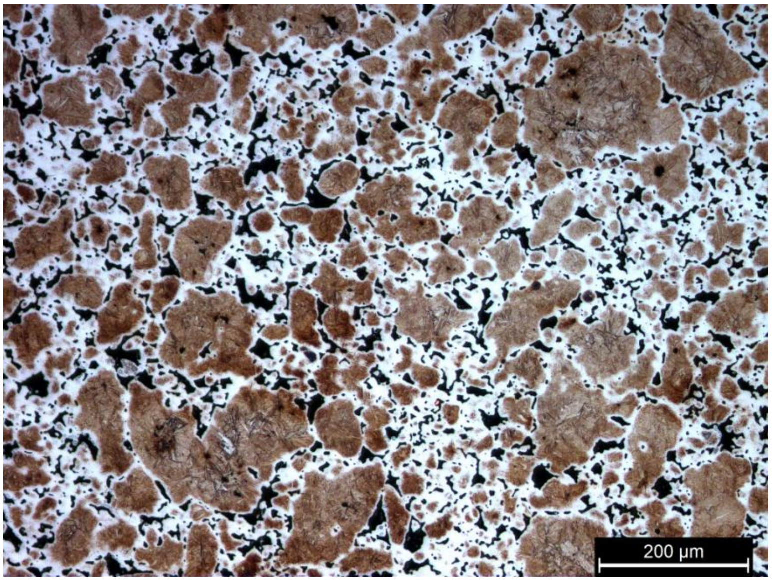

Figure 2.3.1. Heterogeneous microstructure of a PM steel

These heterogeneous microstructures result in different local yield strength in the material depending on the microhardness of the constituents.

It's therefore important to verify if mechanical properties, and in particular the fatigue resistance, may be reliably predicted considering the mean characteristics of the microstructure. A local approach, which considers the localization of the larger pores, where crack nucleates, in the different constituents may result more appropriate. The prediction of the contact fatigue resistance from the microstructural characteristics of the material may be a helpful tool for the selection of the most appropriate steel for any specific applications and for the designers.

The approach proposed in the present thesis for this purpose is based on a recent work by Donzella et al. [66]. These authors showed that cracks will nucleate in case of local plastic deformation and plastic deformation occurs when the maximum local stress exceeds the yield strength of the matrix. The model in this work is developed by calculating the maximum local stress from the theory of the elastic contact and the matrix yield strength from the microhardness of the steels, under different mean Hertzian pressures [32], using both a mean approach and a localized approach which considers the yield strength of the microstructural constituents separately, instead of the mean yield strength of the matrix.

2.4 Shot Peening

Among the different methods proposed to improve the fatigue resistance of PM steels [67-72], shot peening is a cold working localized on the surfaces, which introduces compressive residual stresses in the exposed surface layers of metallic parts by the impingement of a stream of shot at high velocity under controlled conditions [73]. Each shot striking the material acts like a tiny hammer and creates a small indentation. Overlapping indentations cause a plastic deformation of the subsurface layer and consequently produce a compressive residual stress field, useful to prevent crack nucleation, or to stop crack propagation.

Since shot peening is relatively economic, it became one of the most common method to improve fatigue behavior [74-77]. An additional effect of shot peening in porous steels is the densification of the surface layers due to plastic deformation [78-81].

On the other hand the effect of shot peening on the contact fatigue behavior of PM parts has not been investigated as much as that on their mechanical fatigue performances. Only in two works the positive effect of shot peening on the contact fatigue behavior of PM parts has been shown [82, 83]

3. Experimental Procedure

The materials investigated in this research, their chemical compositions, states and sintering temperatures are reported in Table 3.1.

Material	**Chemical Composition**	**State**	**Sintering Temperature °C**
73-DDH2-HD	Fe-1.5Mo-2Cu-0.65C	Sinterhardened + Tempered	1120
73-DHP2-HD	Fe-1.5Mo-2Cu-4Ni-0.65C	Sinterhardened + Tempered	1120
73-DAE1-HD	Fe-0.5Mo-1.5Cu-4Ni-0.3C	Sintered + Case hardened + Tempered	1150
73-DAB1-HD	Fe-0.5Mo-1.5Cu-1.8Ni-0.3C	Sintered + Case hardened + Tempered	1120
73-DAE2-HD	Fe-0.5Mo-1.5Cu-4Ni-0.5C	Sintered + Heat treated + Tempered	1150
73-AS4300C75	Fe-1Ni-0.75C-1Cr-0.6Si-0.1Mn	Sinterhardened + Tempered	1250

Table 3.1. Chemical Compositions, states and sintering temperatures of the investigated materials

Rings with a height of 10 mm, external diameter of 40 mm and internal diameter of 16 mm were compacted in a double action uniaxial press. Compacted discs were sintered/sinterhardened at different temperatures (Table 3.1) and then heat treated. All the production process was carried out in an industrial plant.

Density of the discs was measured by water displacement method and porosity was calculated from theoretical densities; results are reported in Table 3.2.

Material	**Measured Density (g/cm^3)**	**Theoretical Density (g/cm^3)**	**Porosity (%)**
73-DDH2-HD	7.32	7.79	6.08
73-DHP2-HD	7.40	7.82	5.35
73-DAE1-HD	7.36	7.87	6.53
73-DAB1-HD	7.36	7.85	6.23
73-DAE2-HD	7.37	7.83	5.91
73-AS4300C75	7.14	7.60	6.41

Table 3.2. Measured, theoretical density and the porosity of the materials

HV10 hardness was measured by Emco M4U-025 hardness tester on the compaction surface of the discs; twenty measurements were made for each material and the results are listed in Table 3.3. Along with the hardness which is measured, elastic modulus and the Poisson's coefficient of the materials which are also reported in the basis of Höganäs Iron and Steel Powders for Sintered Components [82].

Material	HV10	Elastic Modulus (GPa)	ν
73-DDH2-HD	525 ± 30	155	0.27
73-DHP2-HD	495 ± 19	145	0.27
73-DAE1-HD	450 ± 21	145	0.27
73-DAB1-HD	430 ± 20	150	0.27
73-DAE2-HD	404 ± 27	145	0.27
73-AS4300C75	533 ± 14	150	0.27

Table 3.3. Hardness, elastic modulus and Poisson's ratio of the investigated materials

Both dry sliding and lubricated rolling-sliding tests were carried out on an Amsler tribometer in a disc on disc configuration. Tests were done at room temperature and 30-35% relative humidity. For both dry sliding and lubricated rolling-sliding tests a counterface disc made of 52100 bearing steel with a height of 10 mm and with 40 mm outer and 16 mm inner diameter was used. The properties of the counterface disc are reported in Table 3.4.

Material	Chemical Composition	Elastic Modulus (GPa)	Density (g/cm^3)	HRc	ν
52100 Bearing Steel	Fe-1.5Cr-1C	210	7.81	63	0.3

Table 3.4. Properties of Counterface disc

During sliding tests, sintered discs were fixed while counterface disc was rotating. Figure 3.1 shows the tribometer configuration during dry sliding tests.

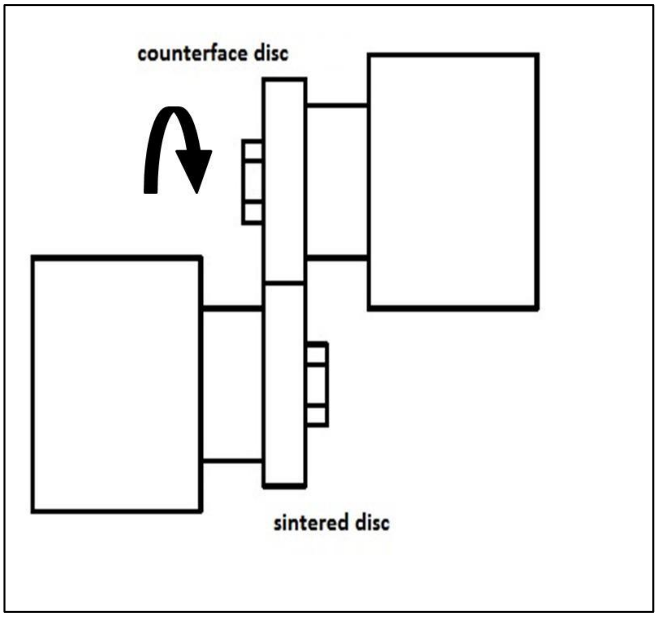

Figure 3.1. Tribometer Configuration during dry sliding tests

Dry sliding tests were carried out at four different loads, 50 N, 100 N 150 N and 200 N and two different revolution speeds 150 rpm, 300 rpm. The resulting sliding speeds were 0.314 m/s and 0.628 m/s, respectively. The total sliding distance was 1260 m for both velocities.

Three tests for each load and speed condition were carried out with the maximum difference in weight loss being within 10% of the mean weight loss for each group. The wear volume of the samples was calculated from the mass loss according to the actual density of the sintered materials. In order to draw the mass loss vs. sliding distance curve the sintered discs were dismounted from the tribometer to measure the mass loss with a precision balance (0.0001 g). After every weighing, disks were remounted on the tribometer, and the previous contact conditions were established by controlling the alignment with the counterface disk, which was not removed from the tribometer. The friction coefficients recorded during all the steps did not show differences suggesting that the weighing procedure did not influence the wear significantly. To investigate the wear mechanisms, wear tracks were observed by both optical and scanning electron microscopy (SEM).

On the other hand, for lubricated rolling contact fatigue tests, the maximum applicable force of 2000 N represented a limit to the maximum Hertzian pressure relevant to the discs with the geometry previously described. To increase the Hertzian pressure, the geometry of the discs was changed by decreasing their contact length. Some of the counterface discs were machined and contact height was reduced down to 3 mm and further down to the point contact. Figure 3.2 illustrates the geometries of the discs used in rolling-sliding tests.

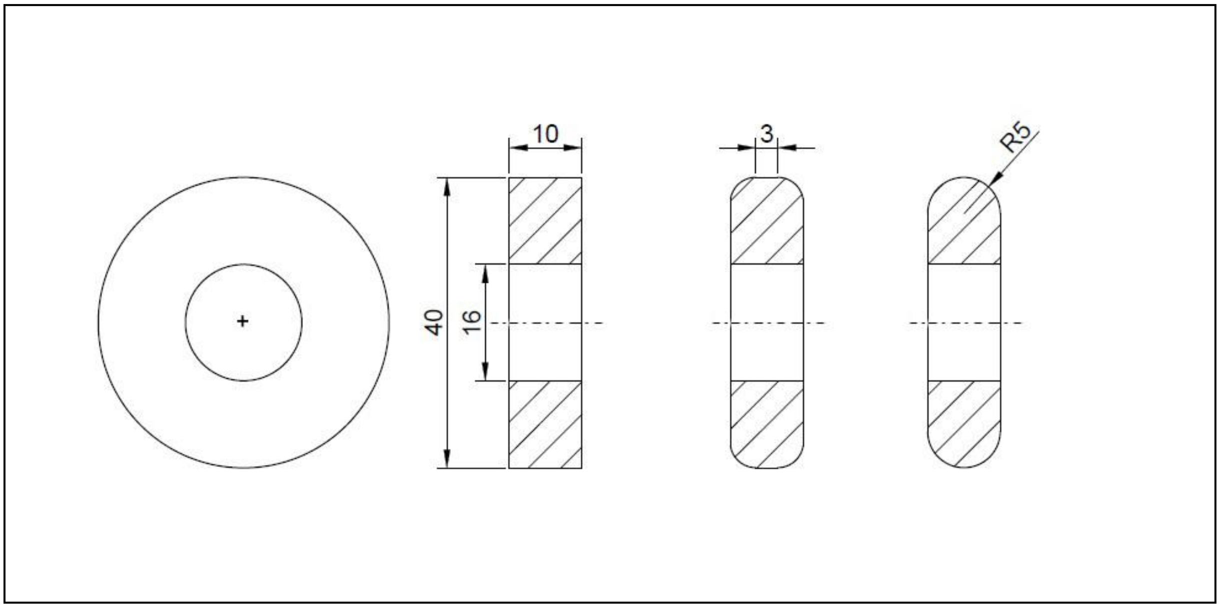

Figure 3.2. Disc geometries as sintered and after machining

Rolling-sliding tests were carried out under lubrication; elastohydrodynamic regime was provided in order to generate a film that separates surfaces. As a lubricant Castrol Edge 5W-30 was used.

Lubrication was provided to the contact region by chain that carries the conveyed oil that was supplied from a case located below the two discs. Figure 3.3 displays the tribometer configuration during rolling sliding tests.

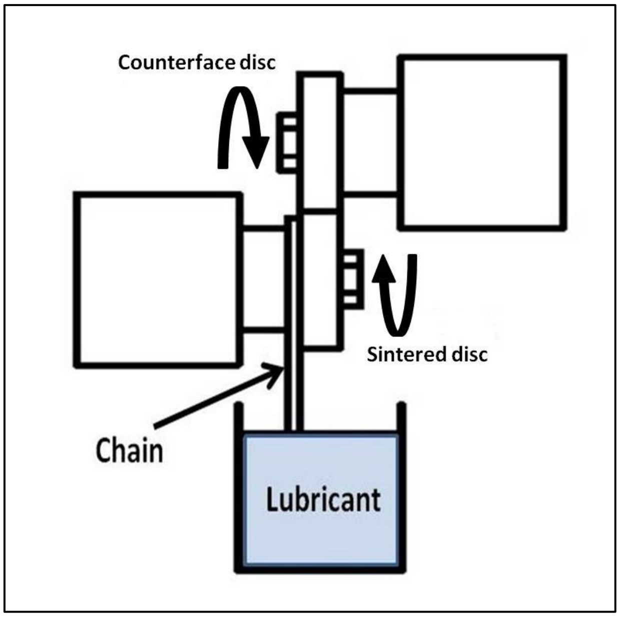

Figure 3.3. Tribometer configuration during rolling sliding tests

During rolling-sliding tests discs were rotating with a revolution speed difference of 10% which results in sliding. The maximum rotating speed of the machine was 400 rpm, 0.838 m/s, for the counterface disc and 360 rpm, 0.754 m/s, for the sintered disc.

Rolling-sliding tests were done by considering one million of cycles as a working life of the component. During all test friction coefficient was recorded and was kept in acceptable range for lubricated tests. After completing one million of cycles, sintered samples were prepared for the metallographic analysis to check any possible crack nucleation or propagation on or close to the surface of the disc.

Two different shot peening treatments were carried out in a preliminary test:

1-) one step ceramic shot peening;

2-) two steps shot peening: first step with steel shots followed by a second step with ceramic shots.

Table 3.5 reports the characteristics of the ceramic and steel shots.

Shot type	Chemical Composition	Density [g/cm^3]
Ceramic	70% Y_2O_3 + 30% ZrO_2	3.85
Steel	1%C – 1%Mn	7.8

Table 3.5. Characteristics of shots

Shot peening was performed by an air blast shot peening machine with an intensity of 4 Almen A for ceramic shots and 12 Almen A for steel shots.

After shot peening, residual stresses were measured by X-ray diffraction and the measurement conditions are listed in Table 3.6.

Incident Radiation	Cr Kα	Elementary Cell	Cubic
Filter	Vanadium	Miller's Index (hkl)	211
Diffractometer configuration	ω	Multi-regression	Yes
Detector type	30°	Background subtraction	Polynomial
Detector's angle range	Strip	2θ position	Free
Acquisition time	30 s	2θ angle	156.33°
Oscillation range	+/-40°	Young modulus	208000 MPa
Number of Ψangles used	7	Poisson coefficient	0.28
Selection of Ψ	Automatic	Power supply	33 kV
Measurements method	Static	Tube's current	85 µA
Materials	Steel	Collimator's diameter	1 mm

Table 3.6. Residual stress measurement conditions

Both shot peening and the analysis of the residual stresses were carried out by 2Effe Engineering, Soiano al lago (BS), Italy.

4. Results and discussion

4.1 Dry Sliding

In case of the disk-on-disk configuration, at the beginning of the tests a line contact was established. Its width, b, was calculated from the theory of the elastic contact [33] by equation (1)

$$b= (4FR' / \pi lE')^{1/2} \qquad (1)$$

where F is the force [N], R' [m] is the reduced radius of curvature of the two discs given by equation (2), l is the contact length [m], and E' [Pa] is the reduced Elastic Modulus given by equation (3)

$$R'=(1/R_1+1/R_2)^{-1} \qquad (2)$$

$$1/E'=0.5[(1-\nu_1^2)/E_1+(1-\nu_2^2)/E_2] \qquad (3)$$

For a generalized use of the results, loading conditions have been expressed in terms of the mean pressure P_0. The mean pressure P_0 was calculated from equation (4)

$$P_0=0.78\ P_{max} \qquad (4)$$

where P_{max} is the maximum contact pressure given by the equation (5)

$$P_{max} = F/(\pi bl) \qquad (5)$$

Wear of the sintered discs quickly promoted the widening of the contact area, whose width was measured by stopping the test every 130 m sliding. The mean pressure was then calculated from equation (6)

$$P_0=F/A \qquad (6)$$

where A [mm^2] is the contact area given by equation (7)

$$A = bl \qquad (7)$$

being b [m] the measured width and l [m] the contact length as before.

The wear rate was calculated from equation (8)

$$W = V/d \qquad (8)$$

where W is wear rate (mm^3/mm), V is the wear volume (mm^3) and d is the sliding distance (mm).

After experiments, calculations and observations, a design procedure was proposed. This proposal was based on the results of the wear tests, in order to evaluate the practical significance of the differences between the materials.

The proposed failure criterion refers to wear depth and defines the maximum value, which can be accepted without impairing functionality. In absence of specific existing requirements, here the maximum tolerable wear depth corresponds to the tolerance of the dimension perpendicular to the wear surface, as defined by the International Organization for Standardization, ISO [84,85].

The wear volume V is the volume of a ring with external diameter R, internal diameter R-h and height l, where R is the radius of the disk, l is the length of the contact area, h is the wear depth, and V is given by the following equation:

$$V = \pi R^2 l - \pi (R-h)^2 l = \pi l(2Rh - h^2) \qquad (9)$$

Since R>>h, the equation may be simplified as

$$V = 2\pi Rlh \qquad (10)$$

By combining equations (8) and (10), the wear rate W results in

$$W=2\pi Rlh/d \qquad (11)$$

Since wear rate is related to the normal force F and hardness H by the Archard law [86]

$$W=KF/H \qquad (12)$$

where K is the dimensionless wear coefficient, the wear depth is given by the following equation

$$h=KFd/2\pi RlH \qquad (13)$$

A failure criterion was defined, in terms of maximum allowable wear thickness, with reference to the dimensional tolerances of the parts considered. In the case of PM parts produced by the conventional press and sintering process, typical ISO IT tolerance classes are decided as IT9, IT10 and IT11. For a part with 40 mm diameter, as the discs used in this study, the dimensional tolerances corresponding to the three aforesaid IT classes are reported in Table 4.1.1. Since tolerances refer to diameters, the maximum acceptable wear depth corresponding to the three classes has been derived by dividing the tolerance by two. The resulting values are reported in Table 4.1.1 as well.

ISO IT class	Tolerance (mm)	Maximum wear depth (mm)
IT 9	0.062	0.031
IT 10	0.100	0.050
IT 11	0.160	0.080

Table 4.1.1 The tolerances for 40 mm diameter PM parts

By considering the values reported in Table 4.1.1, working life of the materials and methods to improve working life were proposed.

4.1.1 Influence of Ni on dry sliding behavior of PM steels

To study the influence of Ni on dry sliding behavior of PM steels two materials were investigated. These materials were 73-DDH2-HD and 73-DHP2-HD, since the only difference in their chemical compositions is Ni. Figure 4.1.1 shows the microstructure of the investigated materials after etching with 50% Nital - 50% Picral solution. After etching it can be seen that 73-DDH2-HD is a mixture of martensitic (white) and bainitic (brown) structure, while 73-DHP2-HD consists of martensite (brown) and Ni-rich austenite (white).

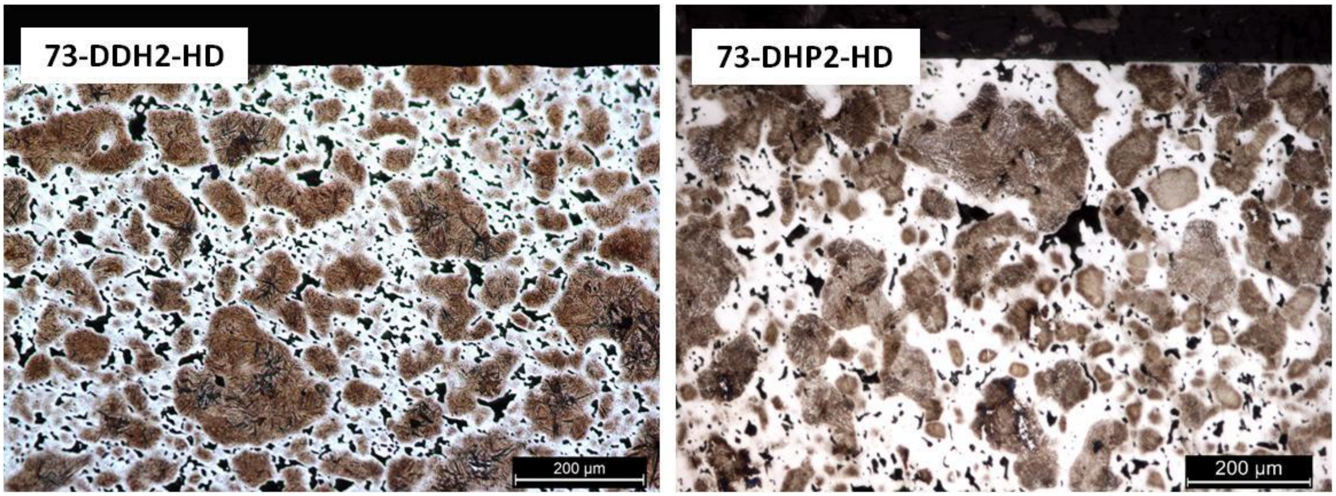

Figure 4.1.1. Microstructure of 73-DDH2-HD and 73-DHP2-HD [87]

4.1.1.1 Wear tests

Due to an increase in contact width by time, the mean pressure P_0 decreased during the test according to the trend shown in Figure 4.1.2, which reports P_0 vs. sliding distance for all possible conditions.

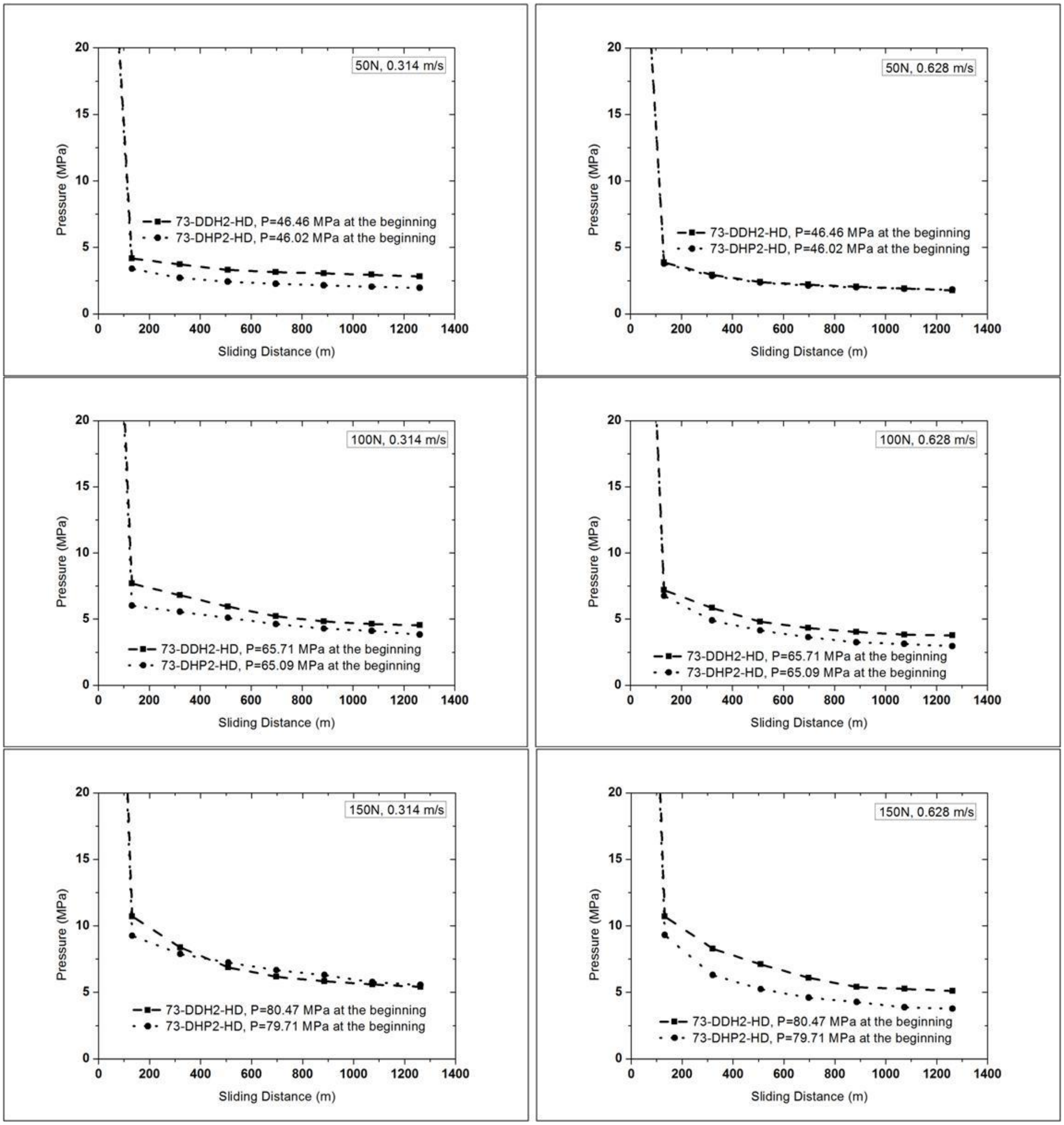

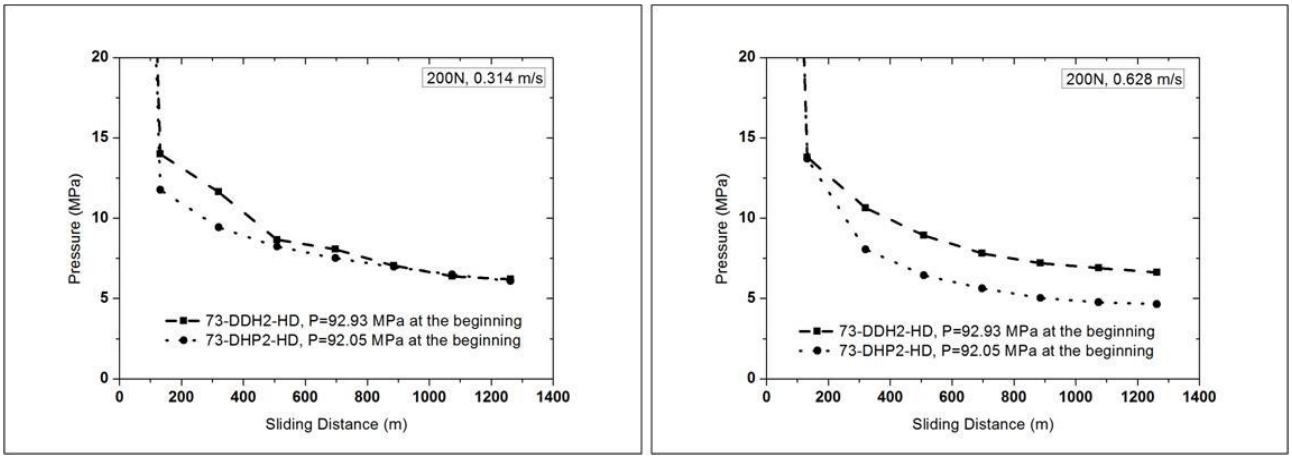

Figure 4.1.2. Mean pressure vs. sliding distance at four different loads and two different speeds

The mean pressure was high at the beginning but it decreased quickly and tended to stabilize on lower values due to the enlargement of the contact area. For further calculations, a constant mean pressure will be used corresponding to the mean value of the seven experimental points, while neglecting the first one. The extension of the contact area was not the same for the two materials subject to the same wear conditions (load, sliding speed and sliding distance), resulting in different mean pressures. This difference was due to the different wear resistance of the two materials as it will be shown in the following.

The mean pressure and the corresponding wear rate are reported in Table 4.1.2, while the relationship between W vs. P_0 is plotted in Figure 4.1.3. No measurable wear was detected on the counterface disc.

Load (N)	Sliding speed (m/s)	73-DDH2-HD		73-DHP2-HD	
		P_0 (MPa)	W (mm^3/mm)	P_0 (MPa)	W (mm^3/mm)
50	0.314	3.3	0.00014	2.4	0.00072
100	0.314	5.7	0.00023	4.8	0.00095
150	0.314	7.0	0.00100	7.0	0.00106
200	0.314	8.9	0.00136	8.1	0.00142
50	0.628	2.4	0.00095	2.4	0.00098
100	0.628	4.8	0.00097	4.1	0.00206
150	0.628	6.9	0.00100	5.3	0.00312
200	0.628	8.1	0.00113	6.9	0.00331

Table 4.1.2. Mean pressure, P_0, and wear rate, W, for all conditions.

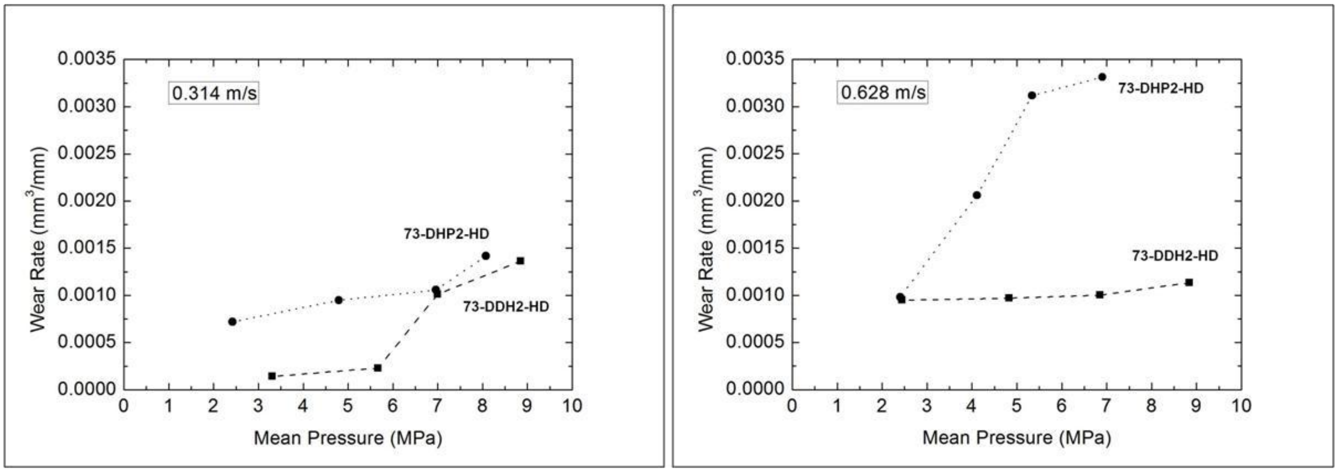

Figure 4.1.3 Wear rate, W, versus mean pressure, P_0, at a) 0.314 m/s and b) 0.628 m/s.

73-DDH2-HD showed a higher wear resistance than 73-DHP2-HD in all the conditions investigated. Wear rate increased with P_0 but with different behaviors depending on the material and the sliding speed. In 73-DDH2-HD the increase in wear rate was well pronounced at the lower speed and almost negligible at the highest speed. In 73-DHP2-HD the increase in wear rate was significant at the lowest speed and even more pronounced at the highest speed. The comparison between the two figures shows that increasing sliding speed results in an increase of wear rate, with the exception of 73-DDH2-HD at higher mean pressures.

4.1.1.2 Characterization of the wear surfaces and profiles

As an example of the characterization performed on the worn specimens, the back scattered electron (BSE) images of the wear surfaces of 73-DDH2-HD after tests at 0.314 m/s for different pressures are shown in Figure 4.1.4.

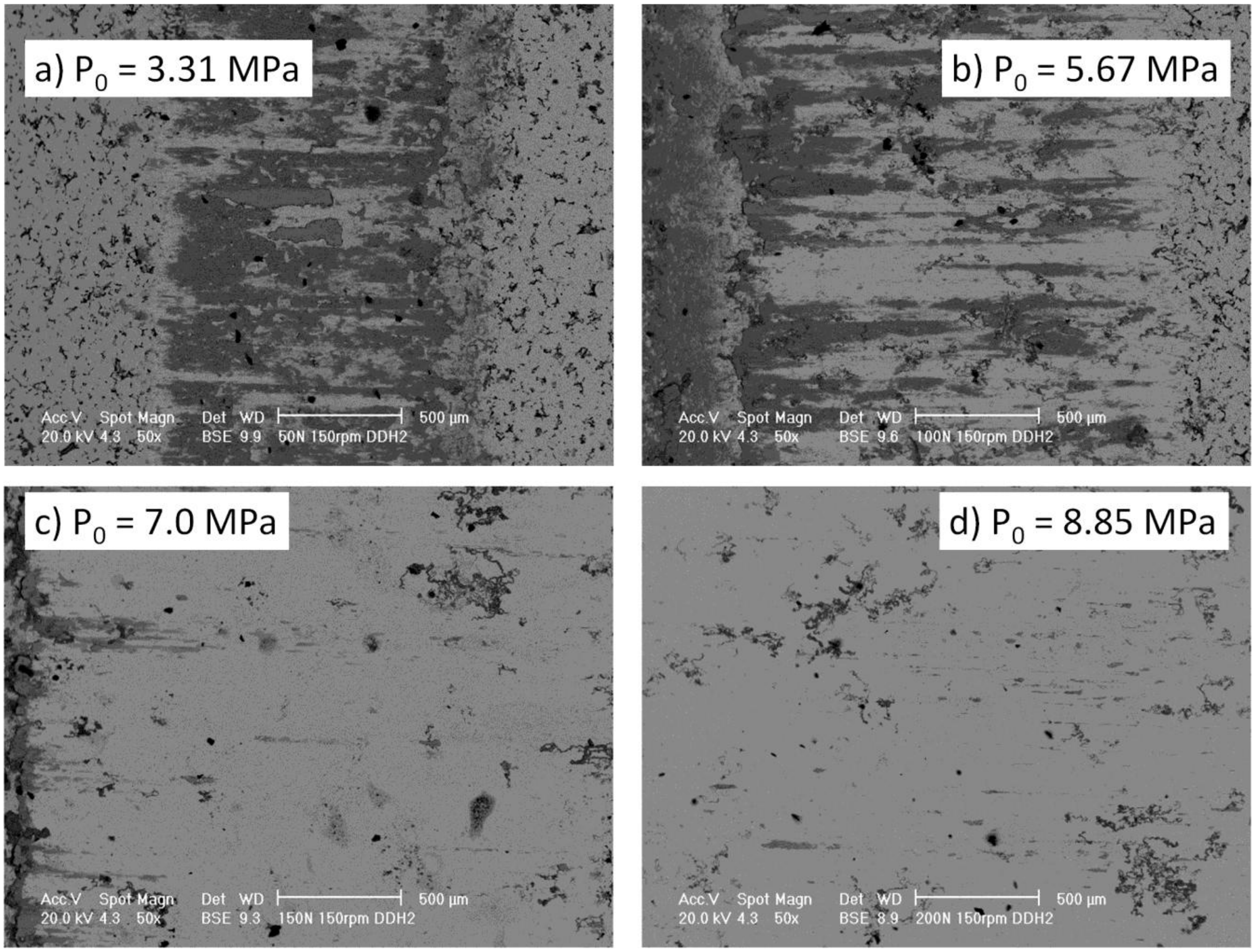

Figure 4.1.4. BSE images of 73-DDH2-HD after wear test at 0.314 m/s and different mean pressure.

The dark areas are iron oxide, as confirmed by EDXS analysis shown in Figure 6. Light areas are unoxidized steel, again confirmed by EDXS in Figure 4.1.5.

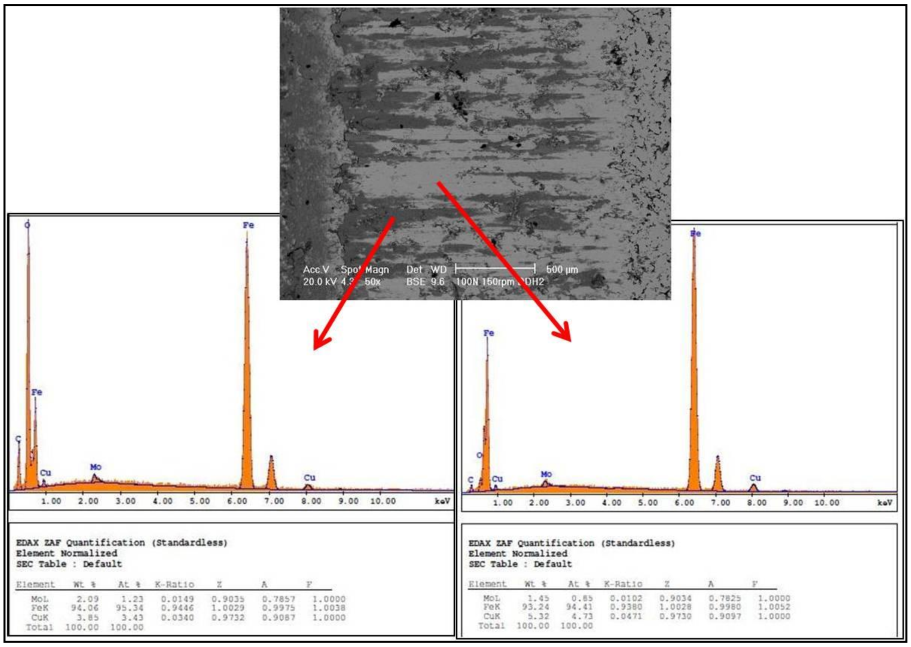

```
EDAX ZAF Quantification (Standardless)
Element Normalized
SEC Table : Default

Element    Wt %    At %   K-Ratio     Z        A        F
   MoL     2.09    1.23   0.0149   0.9035   0.7857   1.0000
   FeK    94.06   95.34   0.9446   1.0029   0.9975   1.0038
   CuK     3.85    3.43   0.0340   0.9732   0.9087   1.0000
 Total   100.00  100.00
```

```
EDAX ZAF Quantification (Standardless)
Element Normalized
SEC Table : Default

Element    Wt %    At %   K-Ratio     Z        A        F
   MoL     1.45    0.85   0.0102   0.9034   0.7825   1.0000
   FeK    93.24   94.41   0.9380   1.0028   0.9980   1.0052
   CuK     5.32    4.73   0.0471   0.9730   0.9097   1.0000
 Total   100.00  100.00
```

Figure 4.1.5. EDXS spectra on different regions of the wear surface.

The wear surface is almost fully covered by an oxide layer at the lowest pressure (a) and slightly less at the second lowest pressure (b). On the contrary, at high pressures there is almost no oxide layer on the wear track, (c) and (d). The oxidation of the wear surface is typical of “low sliding velocity oxidative wear” proposed by Stott [88]. In these conditions, wear leads to the formation of an oxide layer through the compaction and sintering of oxidized wear fragments [89]. Under certain conditions, as the two low pressures in Figure 4.1.4, such a layer is protective and reduces wear rate as confirmed by the low wear rate at those pressure. The absence of any evident oxidation in the images corresponding to the higher mean pressures is in agreement with the higher measured wear rate. The sharp increase in the wear rate at 0.314 m/s was due to the instability of the protective oxide layer under the higher applied loads.

Figure 4.1.6 shows the wear surface of 73-DHP2-HD after tests in the same conditions as for 73-DDH2-HD in Figure 4.1.4.

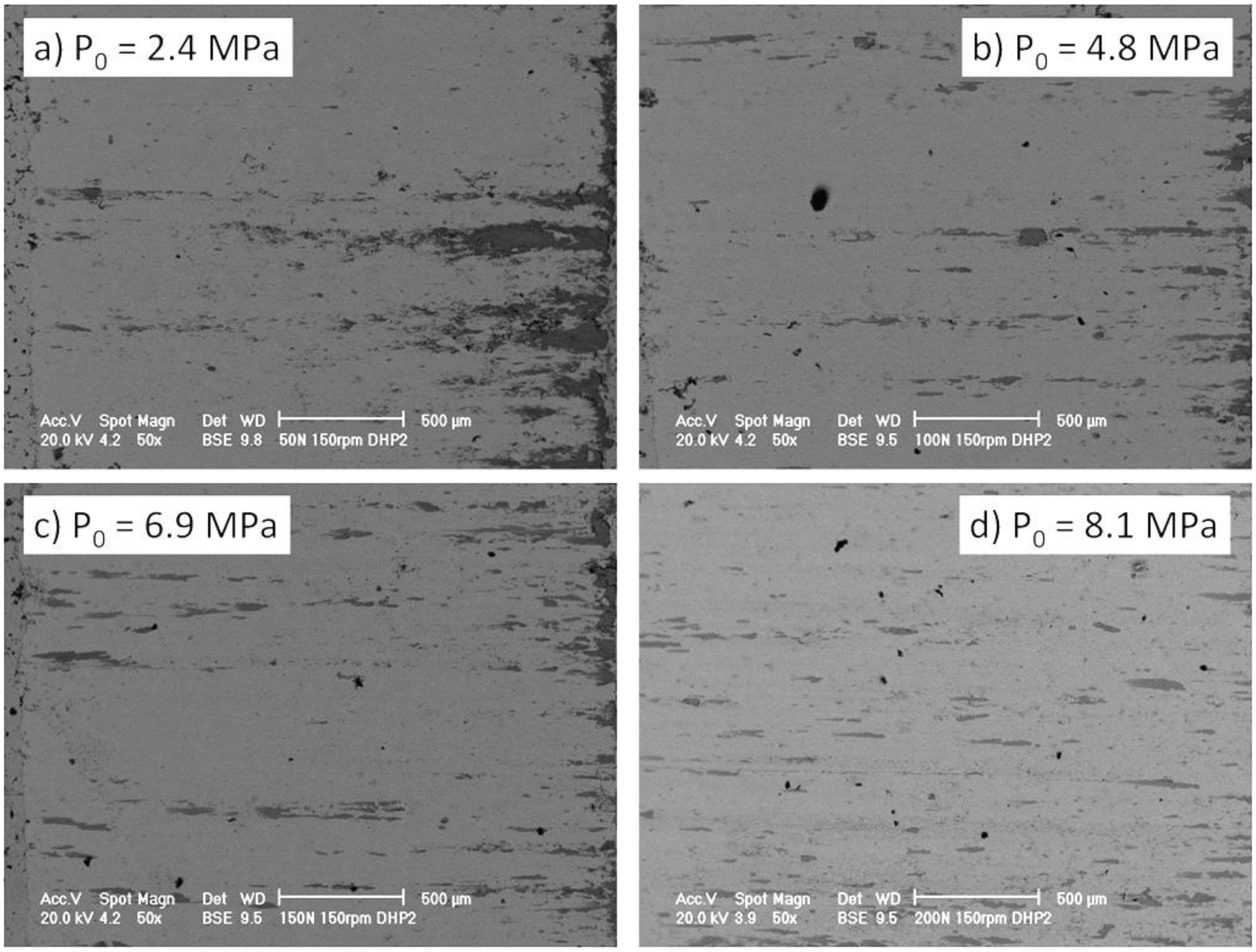

Figure 4.1.6. BSE images of 73-DHP2-HD after wear test at 0.314 m/s and different mean pressure.

No surface oxidation can be observed, indicating that a protective layer did not form in any of the test conditions. This corresponds with the measured wear rates. This means that a stable and protective oxide layer is formed only on the surface of 73-DDH2-HD at the two lower pressures.

At the higher speed, the wear track did not show the protective oxide layer in either of the materials, as shown by Figure 4.1.7, where the wear surface of both 73-DDH2-HD and 73-DHP2-HD at the highest and lowest mean pressures is presented, as an example.

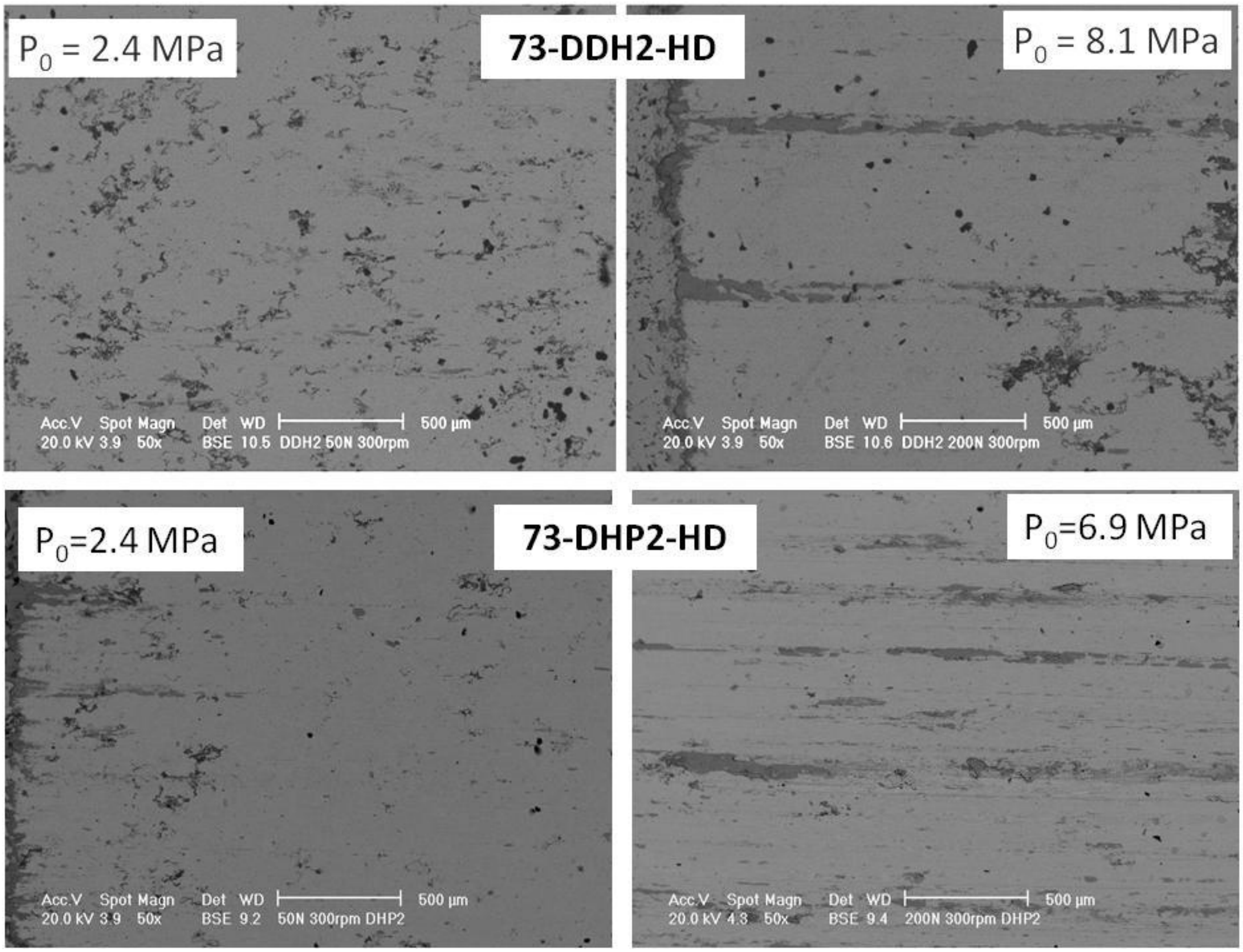

Figure 4.1.7. BSE images of 73-DDH2-HD and 73-DHP2-HD after wear test at 0.628 m/s and different mean pressure.

The increase in the surface temperature caused by the higher sliding speed was responsible for lack of stability of the oxide layer. As seen in Figure 4.1.3 wear rate of 73-DDH2-HD at high sliding does not depend on the mean pressure and the wear rate is similar to that measured at low speed and high pressures, where no stable oxide layer was detected. In 73-DHP2-HD, however, wear rate increased with mean pressure. Figure 4.1.8 shows the wear profile of the two materials at 0.628 m/s and 200 N, corresponding to 8.84 MPa and 6.90 MPa for 73-DDH2-HD and 73-DHP2-HD, respectively. In 73-DHP2-HD, a slight plastic deformation of the surface and subsurface layer can be observed.

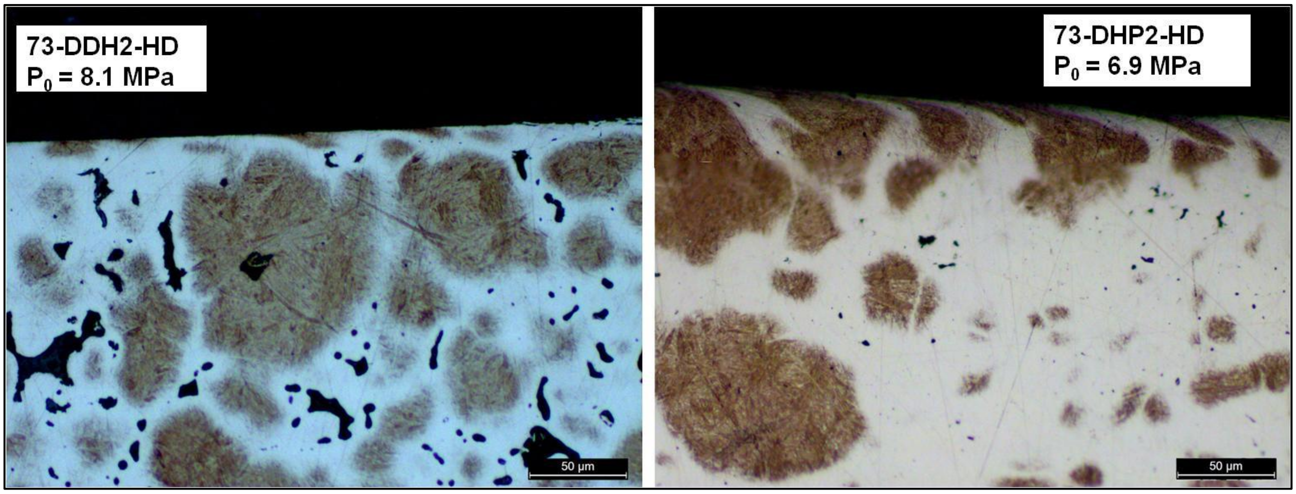

Figure 4.1.8. The surface deformation of the materials investigated after tests at 0.628 m/s

Even when the mean pressure was lower in 73-DHP2-HD, the thickness of the deformed surface layer was larger than in 73-DDH2-HD. This may be attributed to the presence of the soft Ni-rich constituent which is subject to localized plastic deformation and so enhances the wear process.

In conclusion, wear resistance of the two materials depends on their ability to form a stable protective oxide layer and to resist surface plastic deformation. The formation of the oxide layer occurred in 73-DDH2-HD at low speed and low pressure and the increase in both parameters affected the stability of the oxide layer negatively. In 73-DHP2-HD, the presence of the Ni-rich constituent caused localized deformation which impeded the formation of a protective oxide layer at the lower speed and enhances the wear process at the higher speed. Because of the oxide layer never formed, the increase of mean pressure caused increased wear.

The results of the wear tests and their interpretation on the basis of the wear phenomena demonstrate that 73-DDH2-HD performs much better than 73-DHP2-HD under dry sliding conditions. Therefore, in the following section only 73-DDH2-HD will be considered.

4.1.1.3 Failure Criterion and Design Guideline

To investigate the working life of 73-DDH2-HD under tested conditions, wear thickness, h, had to be calculated. For this purpose, wear coefficients K calculated from equation (12) for the different test conditions are reported in Table 4.1.3 for 73-DDH2-HD.

Load (N)	**Sliding speed (m/s)**	**73-DDH2-HD**	
		P_0 (MPa)	**K x 10^{-5}**
50	0.314	3.31	1.46
100	0.314	5.67	1.18
150	0.314	7.00	3.48
200	0.314	8.85	3.51
50	0.628	2.45	9.77
100	0.628	4.83	4.99
150	0.628	6.85	3.44
200	0.628	8.84	2.92

Table 4.1.3 Wear coefficients of 73-DDH2-HD

As an example of dry sliding contact between two parts, the counterface steel used in the wear experiments and 73-DDH2-HD are considered. The geometry of the parts is assumed to form a rectangular contact area with the following dimensions: l = 10 mm, b = 2 mm. If forces of 70 N and 130 N are applied, mean pressures of 3.5 MPa and 6.5 MPa will be obtained respectively. Two different sliding speeds 0.314, 0.628 m/s and a hardness of 5100 MPa is assumed.

Figure 4.1.9 shows the calculated wear depth as a function of the sliding distance for the two mean pressures at 0.314 m/s and 0.628 m/s sliding speed. The maximum tolerable wear depths, which are determined from the three ISO IT classes, are indicated by the dotted lines. The maximum sliding distance considered here is $1.25\text{x}10^5$ m, corresponding to 10^6 revolutions, which can be taken as representative of the required operating life.

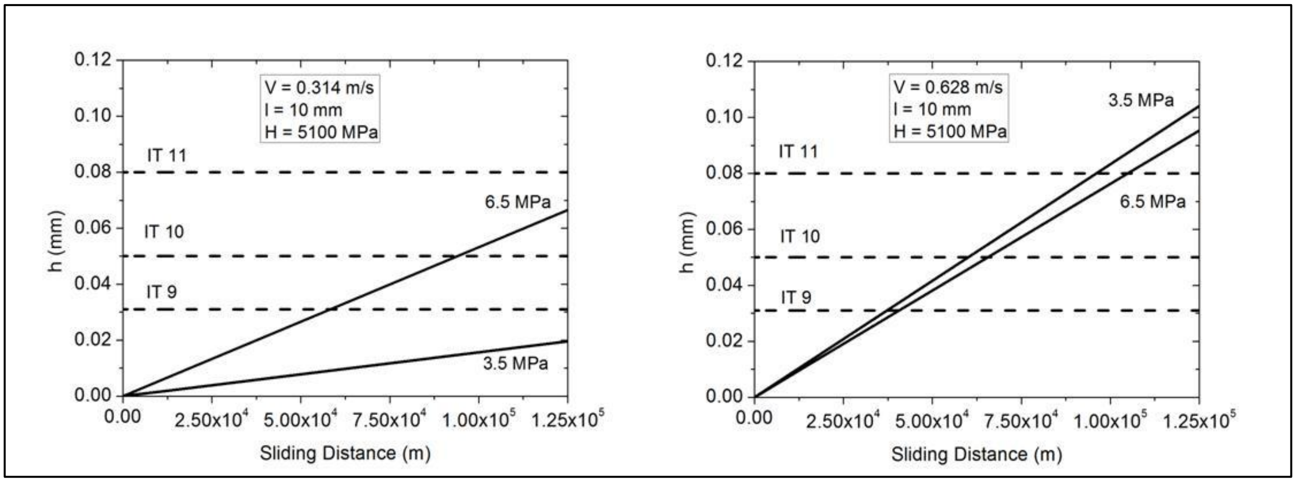

Figure 4.1.9. Wear depth vs. sliding distance at 0.314 m/s and 0.628 m/s.

When the speed is 0.314 m/s and the mean pressure is 3.5 MPa, wear depth remains below the failure criterion for any of the IT tolerance classes during the whole operating life. However, at the higher mean pressure of 6.5 MPa, the failure criteria for IT9 and IT10 are not matched at the end of the operating life. Only the IT11 criterion is met.

When the speed is increased up to 0.628 m/s, the wear depth at the end of the operating life for both mean pressures fails all three IT class criteria.

According to equation (13), wear depth, h, decreases on increasing the hardness H and the contact length l. Following the design approach proposed here, the effect of these two variables on the wear resistance of 73-DDH2-HD are discussed.

An increase in hardness, by increasing the carbon content, may be considered as the first option. For instance, an increase of around 600 MPa in hardness may be expected by increasing the carbon content up to 0.7-0.8%. Figure 4.1.10 shows the resulting wear depth after an increase in hardness at the two sliding speeds; the force and the contact area are the same as those considered in Figure 4.1.9.

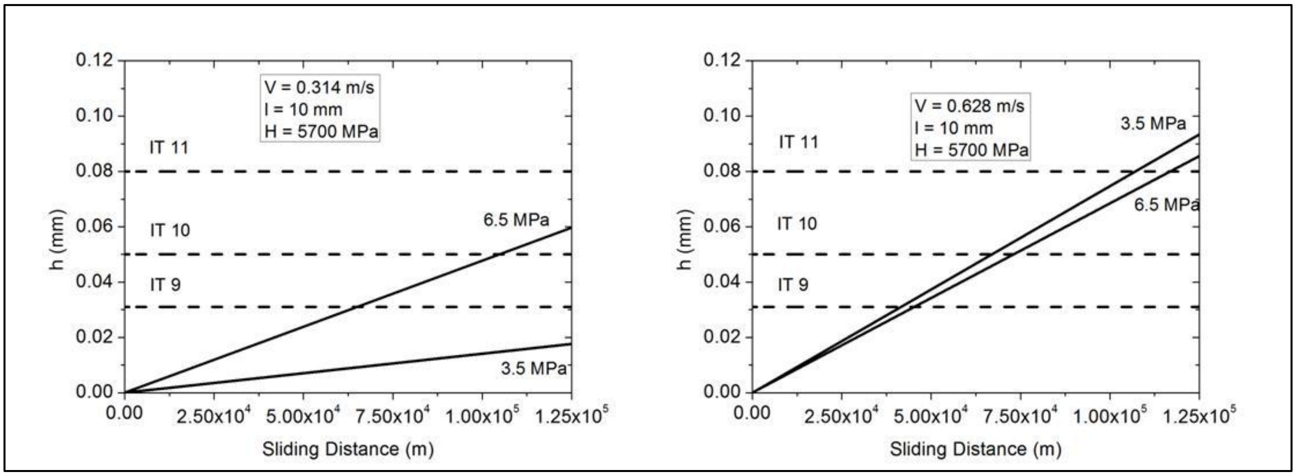

Figure 4.1.10. Wear depth vs. sliding distance with increased hardness

The trend shown in Figure 4.1.10 is the same as in Figure 4.1.9. Although the increase in hardness actually reduces the wear depth, it can be observed that the performance of the material did not improve significantly.

As a second option, a change in contact length is now considered. The length of the contact area is simply the height of the parts in the case at study, which can be increased easily, within certain limits. On the other hand, an increase in the contact length causes an increase in the contact area, which results in a decrease of the mean pressure. For instance, an increase in the contact length by 30% decreases the mean pressure from 3.5 MPa and 6.5 MPa to 2.7 MPa and 5 MPa, respectively, when the normal forces are kept as 70N and 130N, respectively. Considering the decrease of the mean pressure for the higher force, at the lower speed wear resistance decreases dramatically in correspondence with the range where the protective oxide layer is stable (see Figure 4.1.4). Figure 4.1.11 shows the plot of the wear depth in the case of increased length of the contact area. Force and hardness are the same as in Figure 4.1.9.

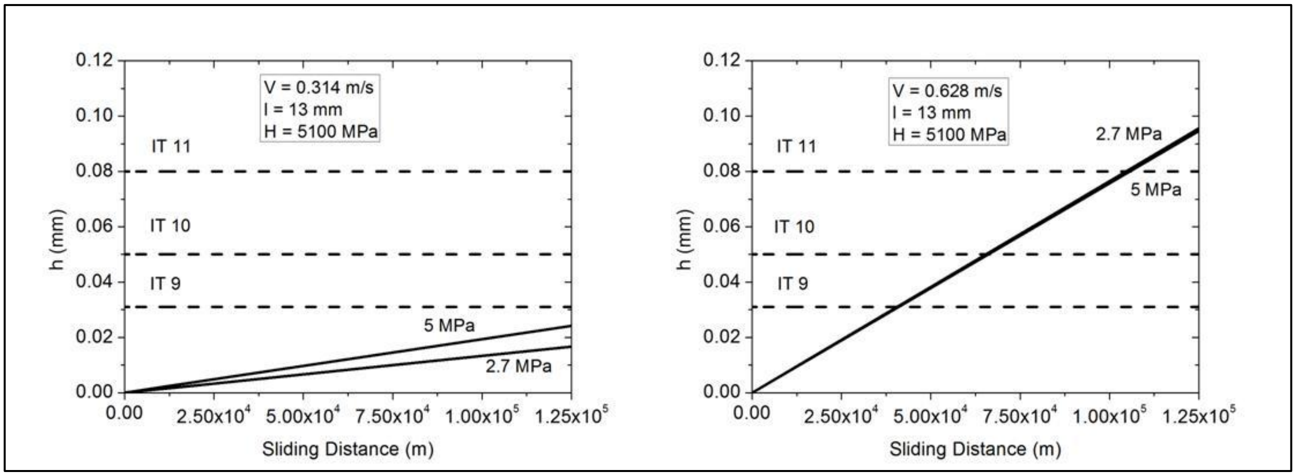

Figure 4.1.11. Wear depth vs. sliding distance with increased contact length

At the lower speed, the performance of the material at the higher force (130N, corresponding to 5 MPa mean pressure) is greatly increased and becomes similar to that corresponding to the lower force, as was expected, due to the transition into the low wear rate range. The wear resistance of the material is ensured during the whole operating life, whichever ISO IT tolerance class is taken as reference for the definition of the failure criterion. Nevertheless, at the higher speed the improvement is poor, and the performance of the material is still not satisfactory.

The results of this last simulation highlight the need for improvement in high speed wear situations and reveal the way to gain it by increasing hardness and/or increasing contact length when considering the wear behavior of the material.

4.1.2 Influence of Ni amount on dry sliding behavior of PM steels

From the results of the previous section, it may be concluded that Ni has a negative effect on the dry sliding wear of the sintered steels. However, Ni alloying has positive effects on other characteristics of the sintered steels such as impact toughness and sizeability. Different contents of Ni are present in conventional sintered steels, and the next step of the research was aimed at investigating the effect of the Ni amount on dry sliding behavior of PM steels. For these purpose two other materials were investigated, differing in the amount of Ni. These two materials were 73-DAE1-HD with 4% Ni and 73-DAB1-HD with 1.8% Ni, which are reported in Table 3.1.

The microstructure of these two materials after etching with 50% Nital - 50% Picral solution are shown in Figure 4.1.12. From their microstructures on subsurface layers martensite, bainite and the Ni-rich austenite (the white phase in the micrographs) can be observed. The content of austenite is higher in 73-DAE1-HD than in 73-DAB1-HD due to the higher amount of Ni.

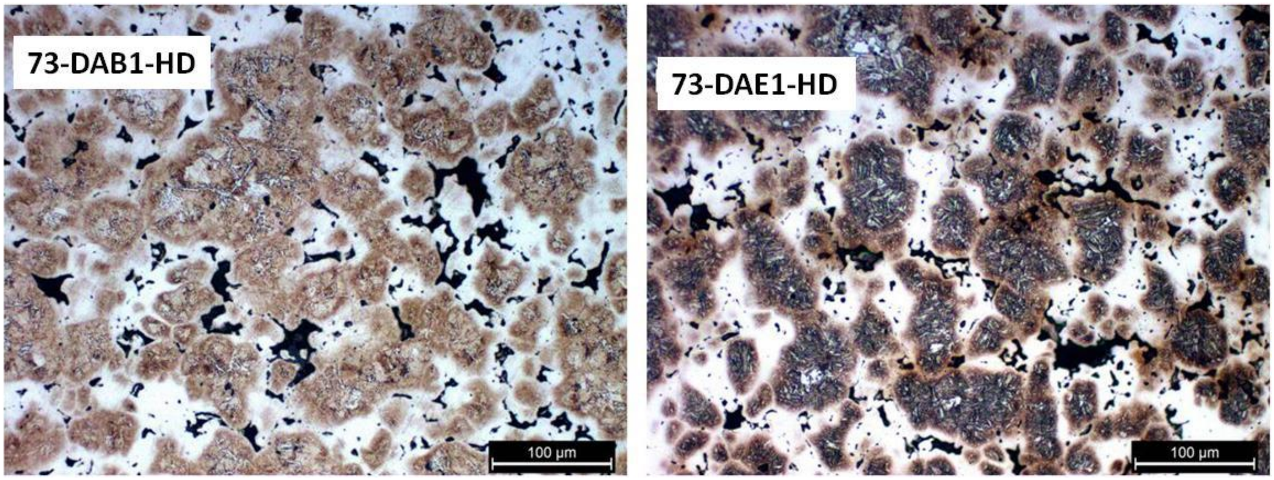

Figure 4.1.12. Microstructure of 73-DAB1-HD and 73-DAE1-HD

4.1.2.1 Wear tests

Wear tests were done under the same conditions as in previous case. Also in this case the mean pressure P_0 was high at the beginning, and decreased afterwards, due to the enlargement in the contact area by time, as it can be seen in Figure 4.1.13.

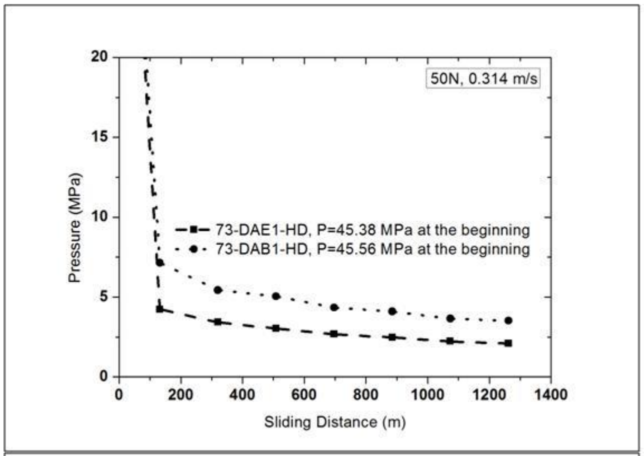
50N, 0.314 m/s
Pressure (MPa)
Sliding Distance (m)
0
5
10
15
20
0
200
400
600
800
1000
1200
1400
73-DAE1-HD, P=45.38 MPa at the beginning
73-DAB1-HD, P=45.56 MPa at the beginning

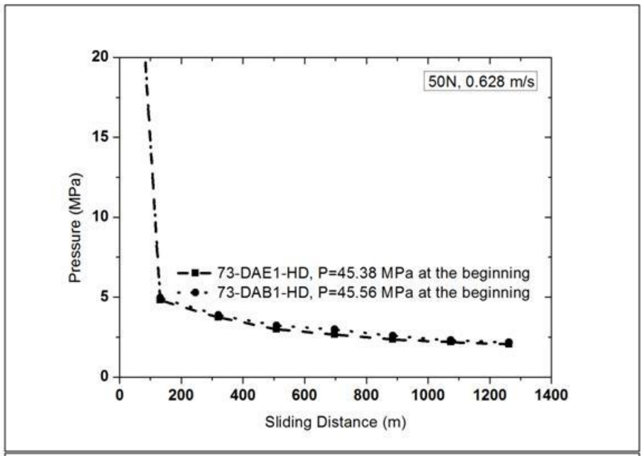
50N, 0.628 m/s
Pressure (MPa)
Sliding Distance (m)
0
5
10
15
20
0
200
400
600
800
1000
1200
1400
73-DAE1-HD, P=45.38 MPa at the beginning
73-DAB1-HD, P=45.56 MPa at the beginning

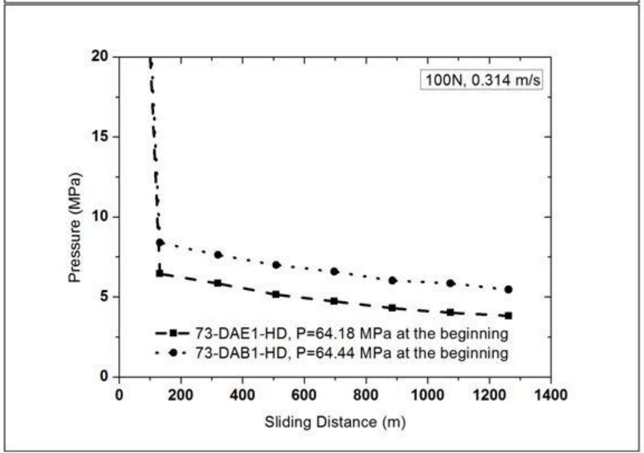
100N, 0.314 m/s
Pressure (MPa)
Sliding Distance (m)
0
5
10
15
20
0
200
400
600
800
1000
1200
1400
73-DAE1-HD, P=64.18 MPa at the beginning
73-DAB1-HD, P=64.44 MPa at the beginning

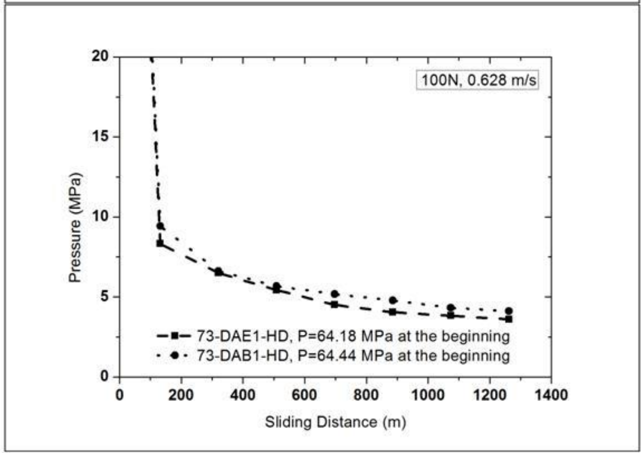
100N, 0.628 m/s
Pressure (MPa)
Sliding Distance (m)
0
5
10
15
20
0
200
400
600
800
1000
1200
1400
73-DAE1-HD, P=64.18 MPa at the beginning
73-DAB1-HD, P=64.44 MPa at the beginning

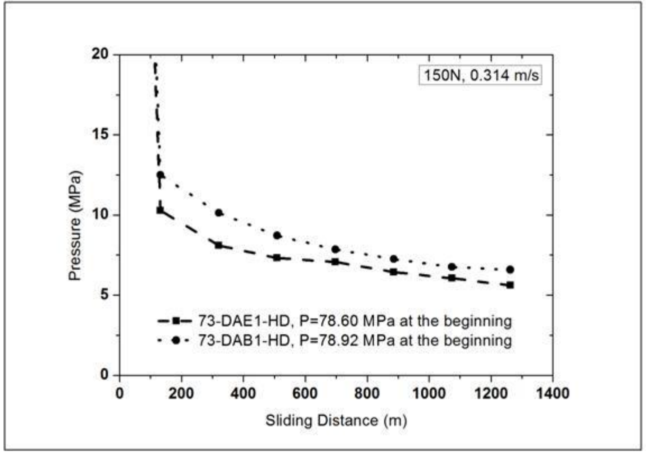
150N, 0.314 m/s
Pressure (MPa)
Sliding Distance (m)
0
5
10
15
20
0
200
400
600
800
1000
1200
1400
73-DAE1-HD, P=78.60 MPa at the beginning
73-DAB1-HD, P=78.92 MPa at the beginning

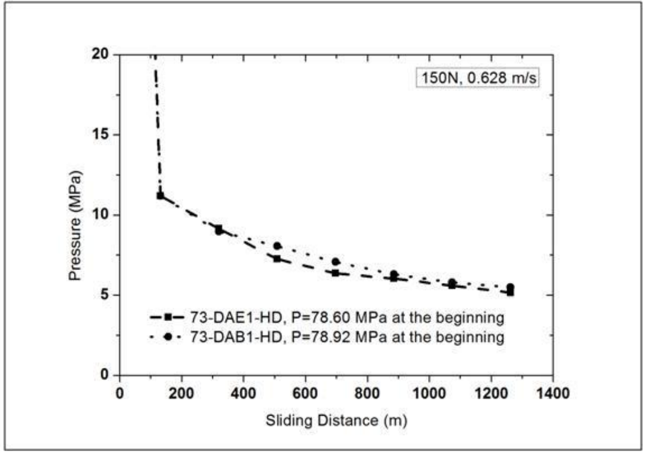
150N, 0.628 m/s
Pressure (MPa)
Sliding Distance (m)
0
5
10
15
20
0
200
400
600
800
1000
1200
1400
73-DAE1-HD, P=78.60 MPa at the beginning
73-DAB1-HD, P=78.92 MPa at the beginning

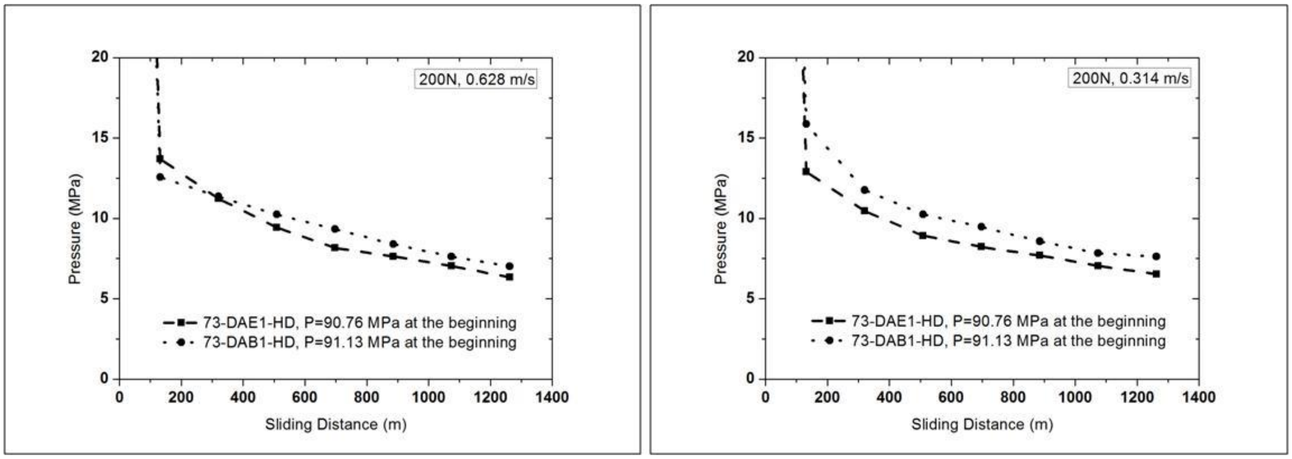

Figure 4.1.13. Mean pressure vs. sliding distance at the lowest load at all four loads and two speeds

In the following, a constant mean pressure will be used corresponding to the mean value of the seven experimental points, neglecting the initial value. The extension of the contact area and the resulting mean pressure were not the same, even the tests were done in the same conditions such as load, speed, sliding distance, due to the different wear resistance of the two materials, as it is shown in the following Table 4.1.4. In addition, the relationship between W and P_0 is plotted in Figure 4.1.14.

Load (N)	**Sliding speed (m/s)**	**P_0 (MPa)**	
		73-DAB1-HD	**73-DAE1-HD**
50	0.314	4.74	2.88
100	0.314	6.79	4.90
150	0.314	8.54	7.27
200	0.314	10.20	8.83
50	0.628	3.15	2.97
100	0.628	5.73	5.18
150	0.628	7.55	7.25
200	0.628	9.59	9.08

Table 4.1.4. Mean pressure, P_0, for all conditions

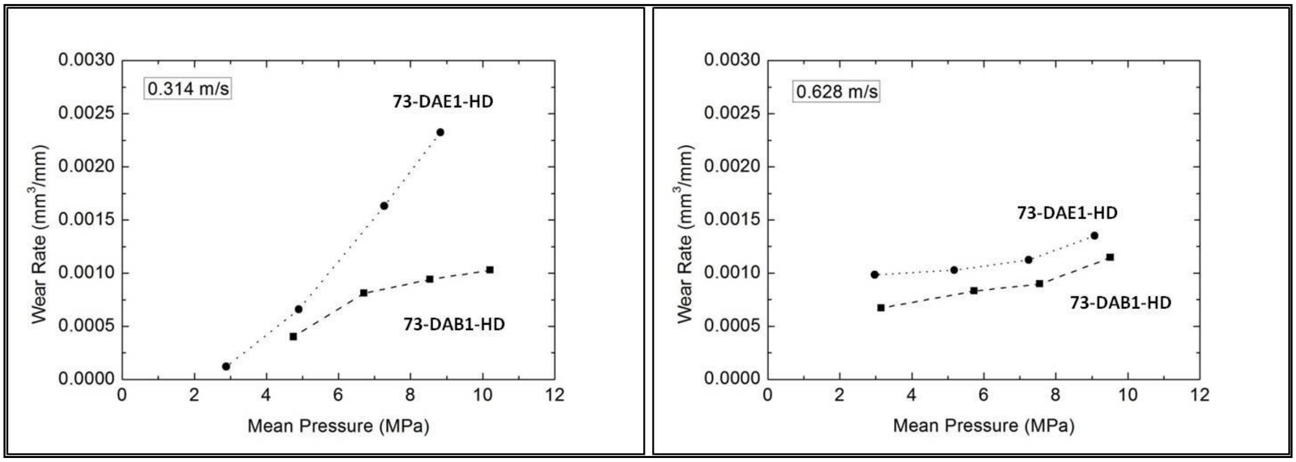

Figure 4.1.14. Wear rate, W, versus mean pressure, P_0, at 0.314 m/s (left) and 0.628 m/s (right).

73-DAB1-HD shows a higher wear resistance than 73-DAE1-HD in all the conditions investigated, and this confirms the effect of Ni-austenite on wear. Wear rate slightly increases with P_0 with the exception of 73-DAE1-HD at the lower speed, where the effect of mean pressure on increasing wear rate is much more evident. The influence of the sliding speed is not systematic; in principle wear rate slightly increases with sliding speed, apart from the case of 73-DAE1-HD at the higher mean pressures where wear rate is significantly higher at the lower sliding speed.

4.1.2.2 Characterization of the wear surfaces and profiles

Figure 4.1.15 shows the back scattered electron (BSE) images of the wear surface of 73-DAB1-HD after tests at 0.314 m/s for different pressures.

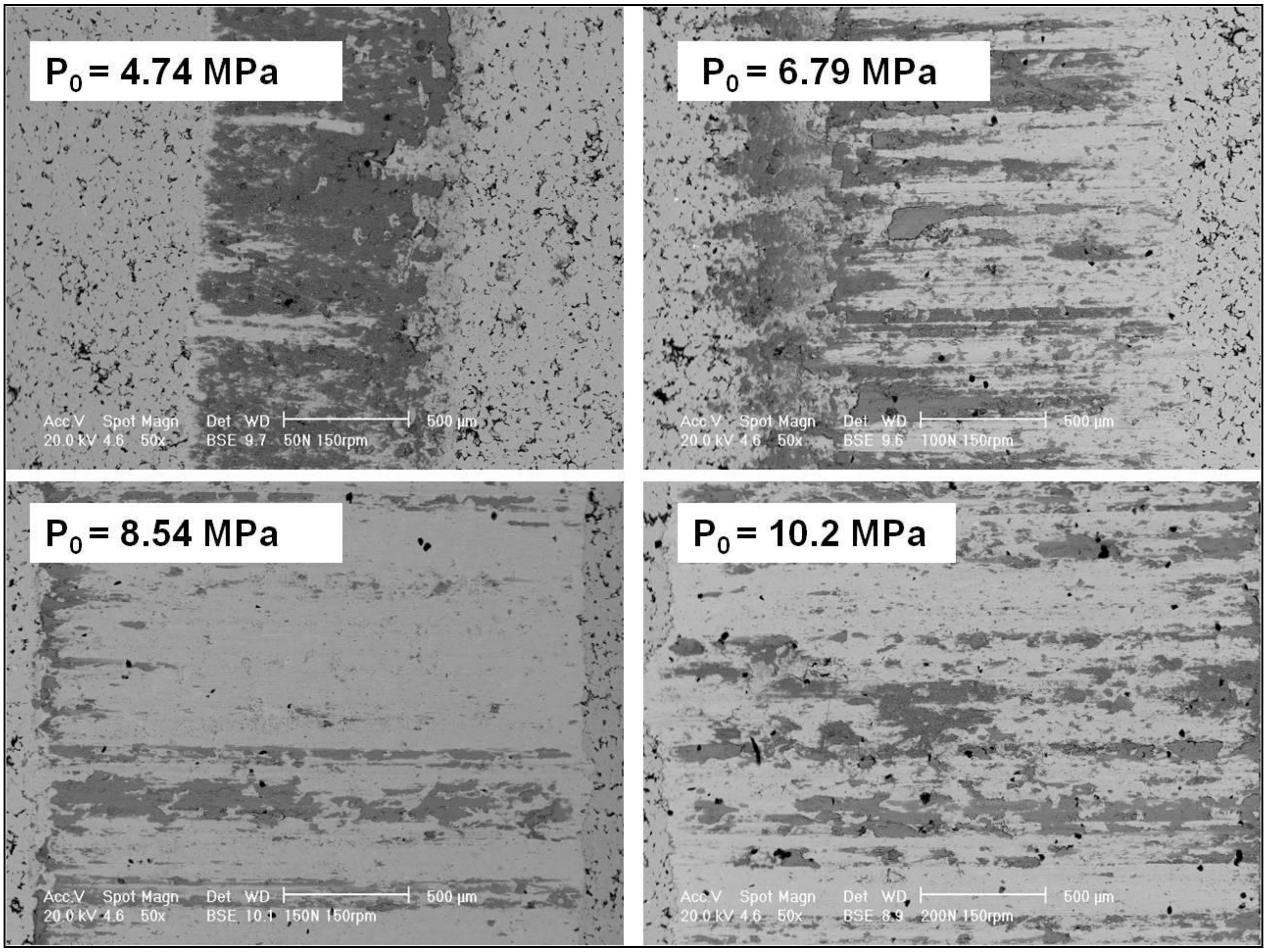

Figure 4.1.15. BSE images of 73-DAB1-HD after wear test at 0.314 m/s and different mean pressure.

The wear surface is either almost fully (lowest mean pressure) or partially (other pressures) covered by an oxide layer, whose coverage decreases on increasing the mean pressure. Figure 4.1.16 shows a detail of the oxide scale; the morphology unambiguously indicates that it has been formed through the compaction and sintering of oxidized wear fragments [89]. This mechanism is typical of the “low sliding velocity oxidative wear” proposed by Stott, as it was discussed previously.

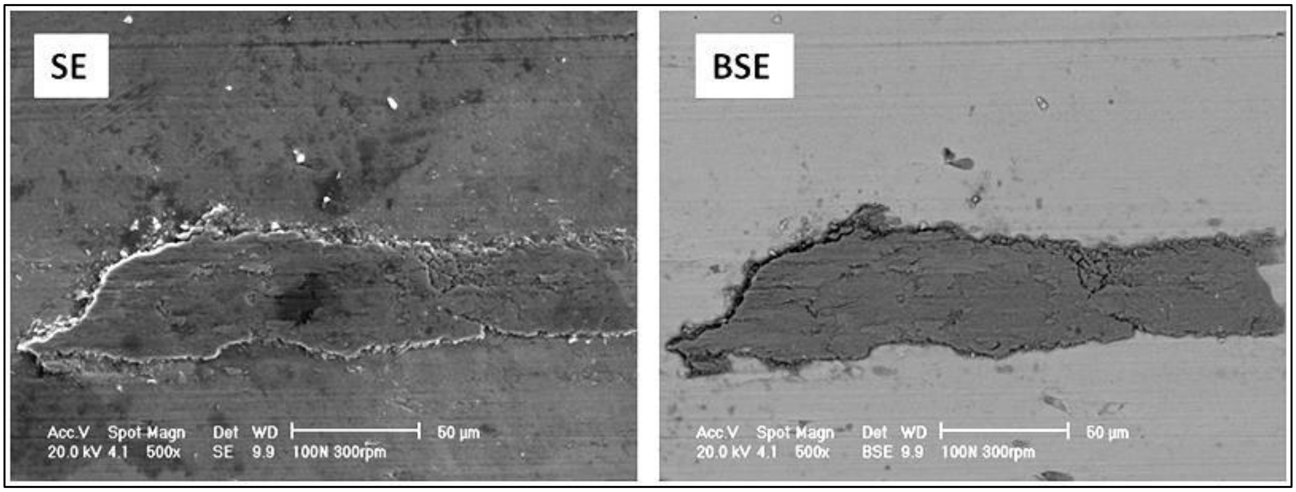

Figure 4.1.16. Secondary Electron and Back Scattered Electron SEM images on the oxide.

According to Stott [88], under certain conditions the oxide layer is protective and reduces wear rate. The progressive increase in wear rate with mean pressure, Figure 4.1.15, is in agreement with the ever less coverage shown in figure 4.1.16.

Figure 4.1.17 shows the wear surface of 73-DAE1-HD after tests at 0.314 m/s.

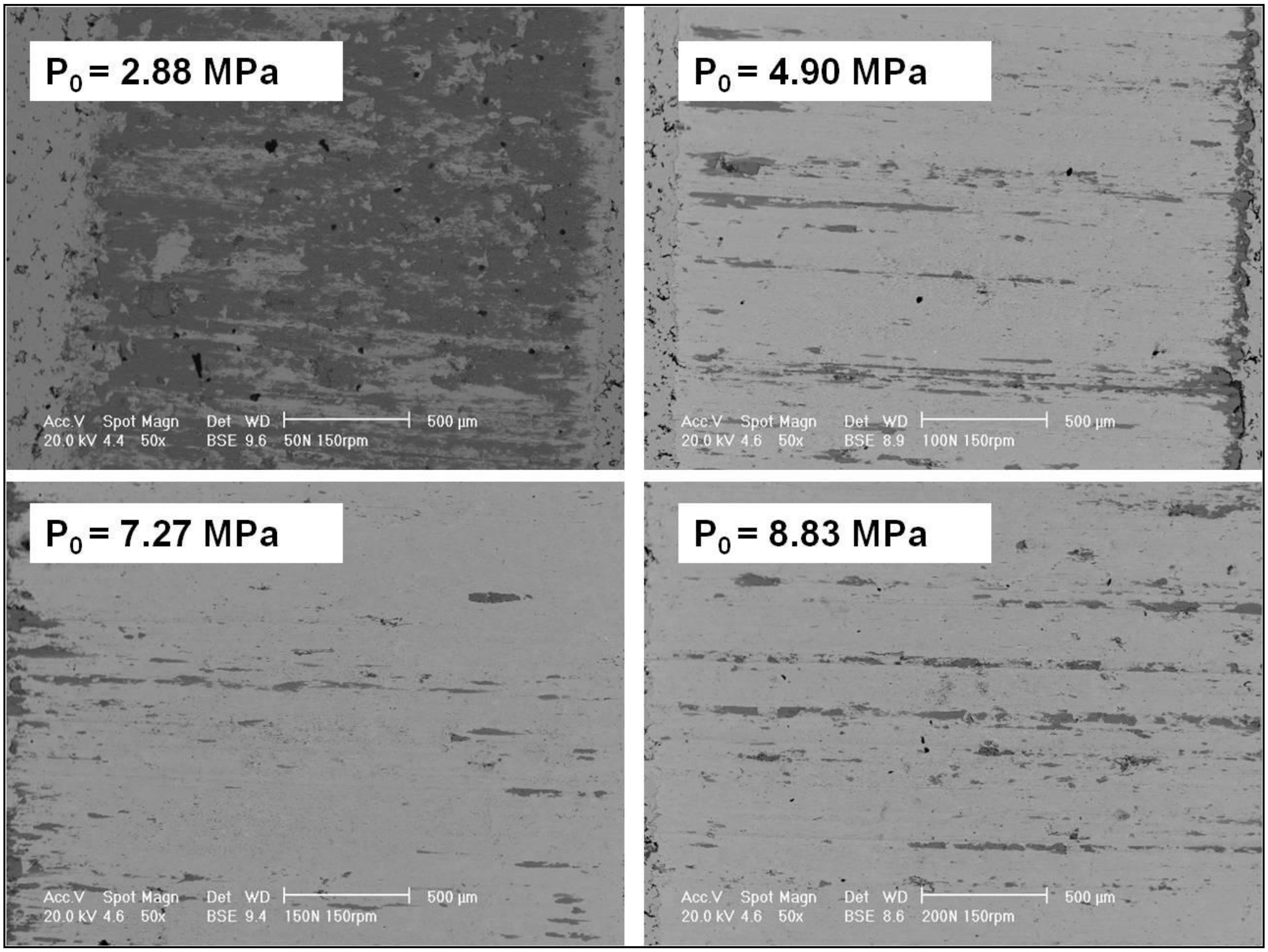

Figure 4.1.17. BSE images of 73-DAE1-HD after wear test at 0.314 m/s and different mean pressure.

Similarly to 73-DAB1-HD, the protective oxide layer is observed at the lowest mean pressure; in the other cases, coverage by the oxide layer is negligible. It’s interesting the comparison between the two materials at the same mean pressure: 4.74 MPa for 73-DAB1-HD, 4.90 MPa for to 73-DAE1-HD. The protective oxide is visible in to 73-DAB1-HD only, which results in a slight but significant lower wear rate.

At the higher speed the wear track does not show the protective oxide layer in both the materials, as shown by Figures 4.1.18 and 4.1.19. Under these conditions, adhesive wear is observed.

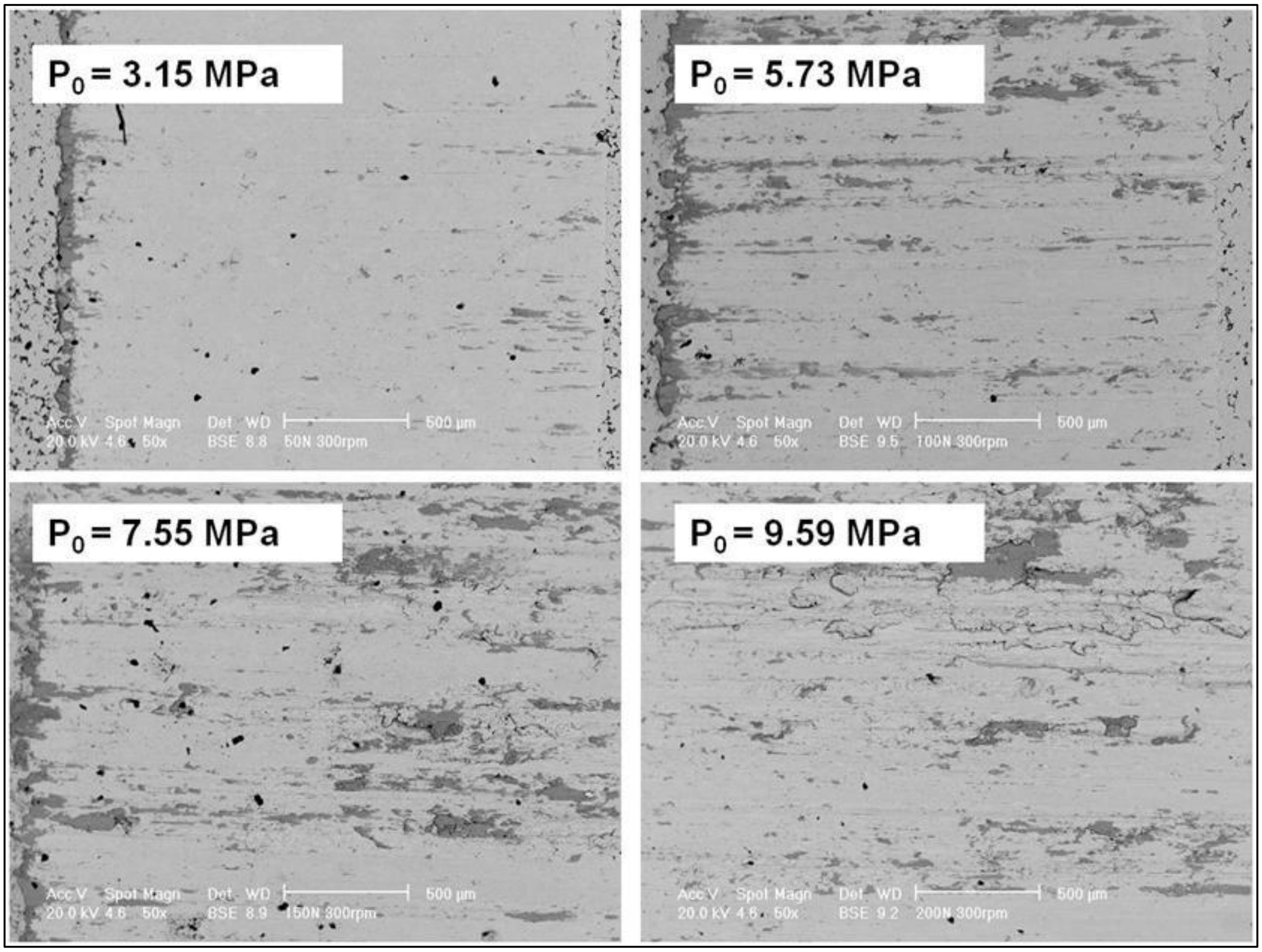

Figure 4.1.18. BSE images of 73-DAB1-HD after wear test at 0.628 m/s and different mean pressure.

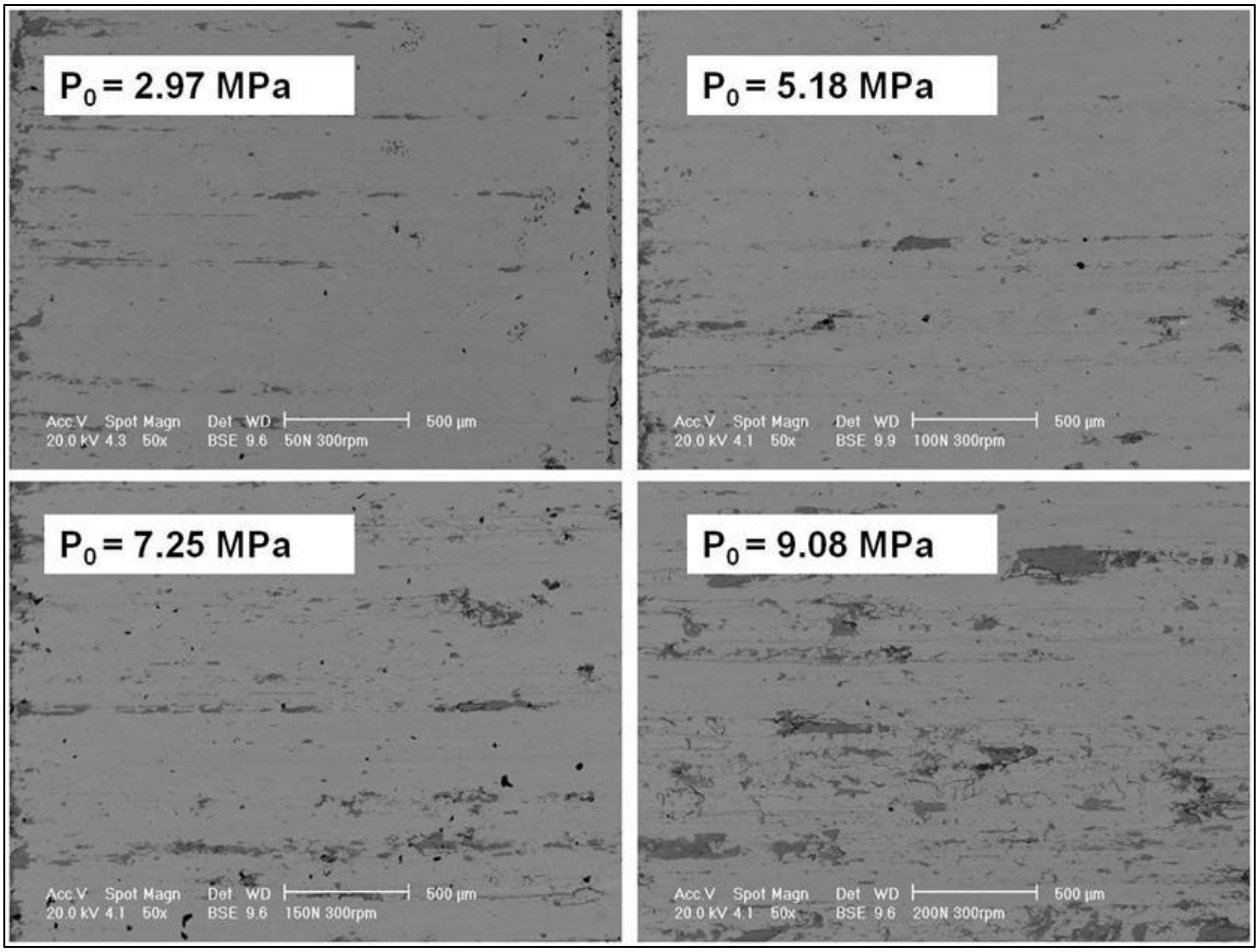

Figure 4.1.19. BSE images of 73-DAE1-HD after wear test at 0.628 m/s and different mean pressure.

It can be concluded that at the lower speed a transition from oxidative to adhesive wear occurs on increasing the mean pressure; such a transition is gradual in 73-DAB1-HD and sharp in 73-DAE1-HD between 2.88 MPa and 4.90 MPa. At the higher speed wear is adhesive in the whole pressure range investigated, since the higher speed does not allow the formation of the protective oxide scale.

The different wear resistance of the two materials can be attributed to the different amount of Ni-rich austenite. It is softer than martensite and bainite and promotes localized deformation, thus reducing the mechanical stability of the surface oxide and enhancing adhesive wear.

However, since there is no sharp difference between the wear rates of 73-DAE1-HD and 73-DAB1-HD, as in the case of 73-DDH2-HD and 73-DHP2-HD, for the following section both materials are considered.

4.1.2.3 Failure criterion and design guideline

K values were calculated using equation (12) for the two materials under the different test conditions and are reported in Table 4.1.5.

Load (N)	Sliding speed (m/s)	73-DAB1-HD		73-DAE1-HD	
		P_0 (MPa)	K x 10^{-5}	P_0 (MPa)	K x 10^{-5}
50	0.314	4.74	3.67	2.88	1.02
100	0.314	6.79	3.72	4.90	2.84
150	0.314	8.54	2.87	7.27	4.68
200	0.314	10.20	2.35	8.83	5.00
50	0.628	3.15	6.14	2.97	8.46
100	0.628	5.73	3.82	5.18	4.42
150	0.628	7.55	2.74	7.25	3.22
200	0.628	9.59	2.63	9.08	2.91

Table 4.1.5. Wear coefficients of 73-DAB1-HD and 73-DAE1-HD

As in the previous section, two parts in a dry sliding contact, determining a rectangular contact area with the following dimensions: l = 10 mm, b = 2 mm were considered. Two different speeds, 0.314 m/s, 0.628 m/s, and mean pressures, 4 MPa and 8 MPa, were studied. Maximum sliding distance of 1.25x105 m, corresponding to 10^6 revolutions was taken as representative of the required operating life.

Figure 4.1.20 and 4.1.21 plot the wear depth vs. the sliding distance for 73-DAB1-HD and 73-DAE1-HD respectively. In each figure the dashed lines represent the maximum wear thickness corresponding to the three ISO IT classes mentioned previously.

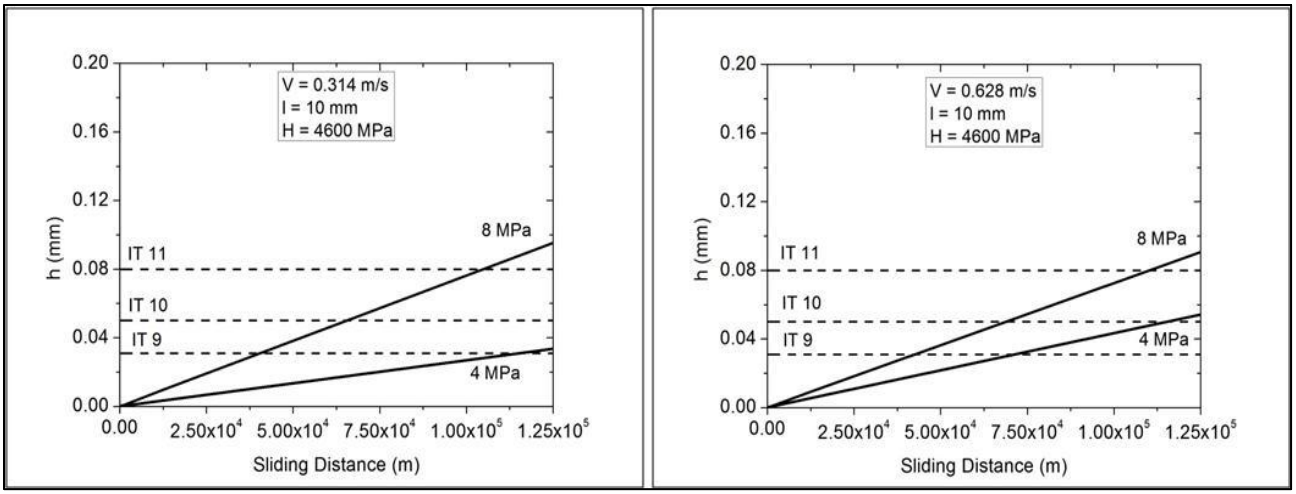

Figure 4.1.20. Wear depth vs. sliding distance of 73-DAB1-HD at 0.314 m/s and 0.628 m/s.

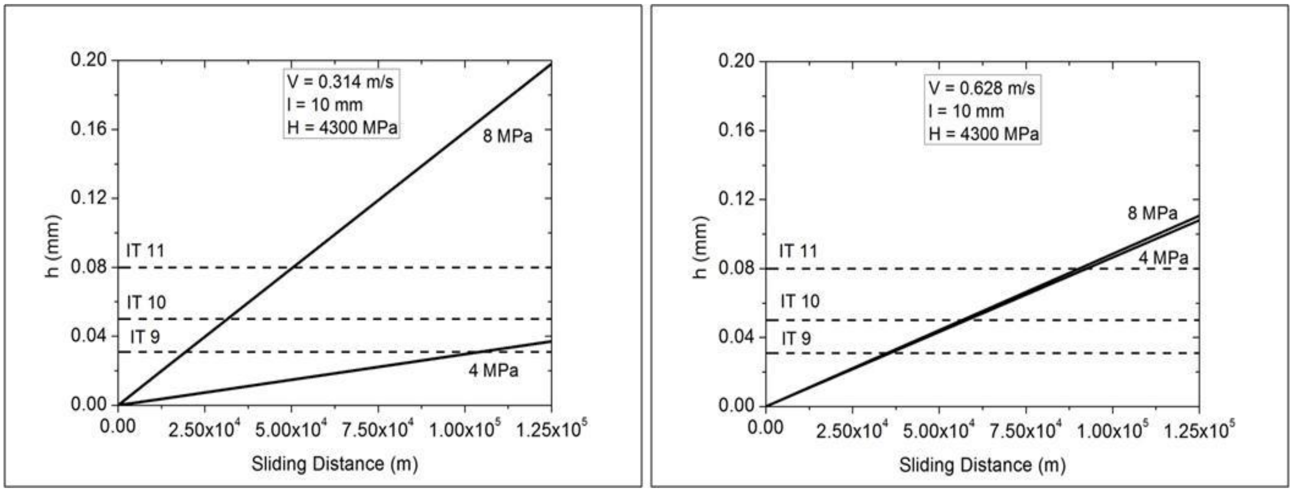

Figure 4.1.21. Wear depth vs. sliding distance of 73-DAE1-HD at 0.314 m/s and 0.628 m/s.

At the lower speed, both the materials meet the failure criterion when the required tolerance class is IT10 and IT11 at 4 MPa, whilst at the higher pressure both the materials fail in any case.

At the higher speed 73-DAE1-HD fails in all the cases considered, whilst 73-DAB1-HD matches the failure criterion when the required tolerance class is IT11.

As in the previous section, the effect of hardness and of the contact length on the wear resistance of both materials is discussed.

An increase in hardness, by increasing the carbon content, can be considered as a first option. For this purpose, as it was done in the previous section, hardness increased by 600 MPa for both materials.

Figure 4.1.22 and 4.1.23 show the resulting wear depth after an increase in hardness at the two sliding speeds; the force and the contact area are the same as those considered in Figure 10 and 11.

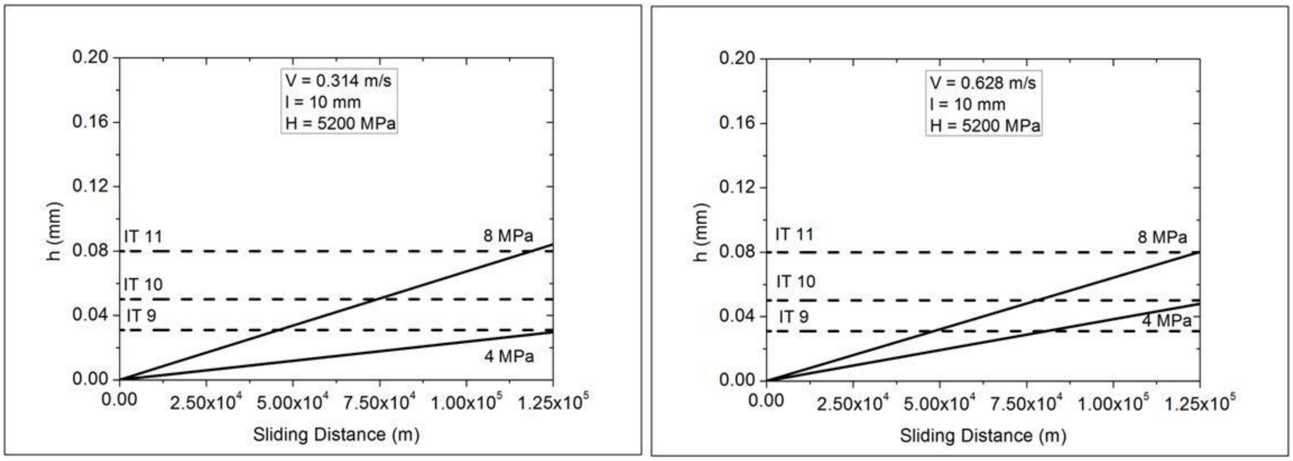

Figure 4.1.22. Wear depth vs. sliding distance of 73-DAB1-HD at 0.314 m/s and 0.628 m/s with an increased hardness

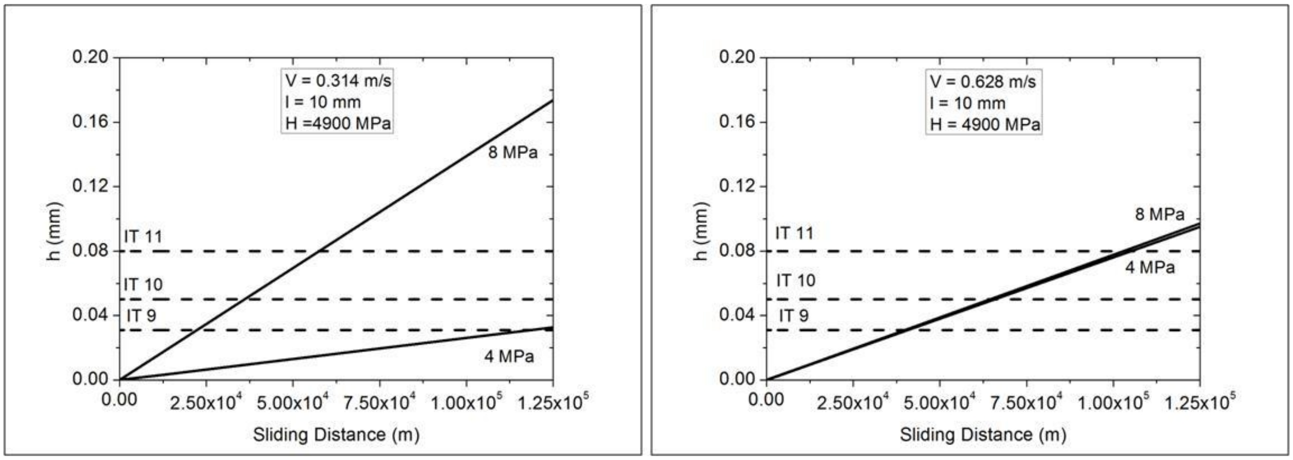

Figure 4.1.23. Wear depth vs. sliding distance of 73-DAE1-HD at 0.314 m/s and 0.628 m/s with an increased hardness

After increasing hardness it can be observed there is a minor change in reducing the wear depth. However, this minor change is not enough to improve wear resistance of the materials notably.

When changing the geometry is considered, the contact length is increased by 30%. This increase results in a decrease in the contact area which means a decrease in the mean pressure. 4 MPa and 8 MPa mean pressures drop down to 3.08 MPa and 6.15 MPa, respectively, when the normal forces are kept as 65 N, 130 N for 73-DAB1-HD and 73 N, 171 N for 73-DAE1-HD. Figure 4.1.24 and 4.1.25

show the plot of the wear depth in the case of increased length of the contact area by 30% for both materials. Force and hardness are the same as in Figure 4.1.20 and 4.1.21.

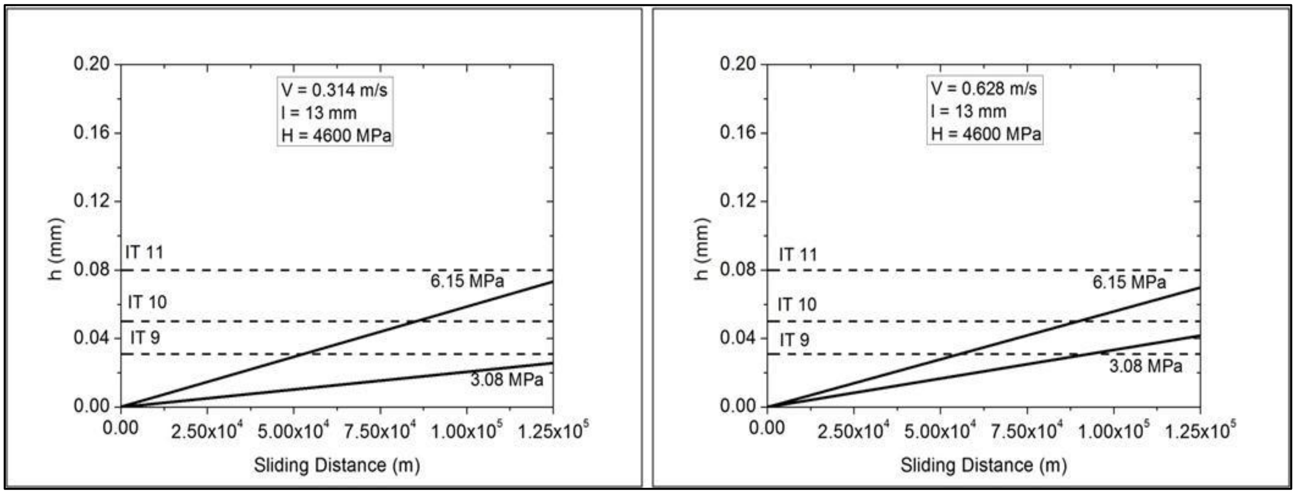

Figure 4.1.24. Wear depth vs. sliding distance of 73-DAB1-HD at 0.314 m/s and 0.628 m/s with an increased contact length

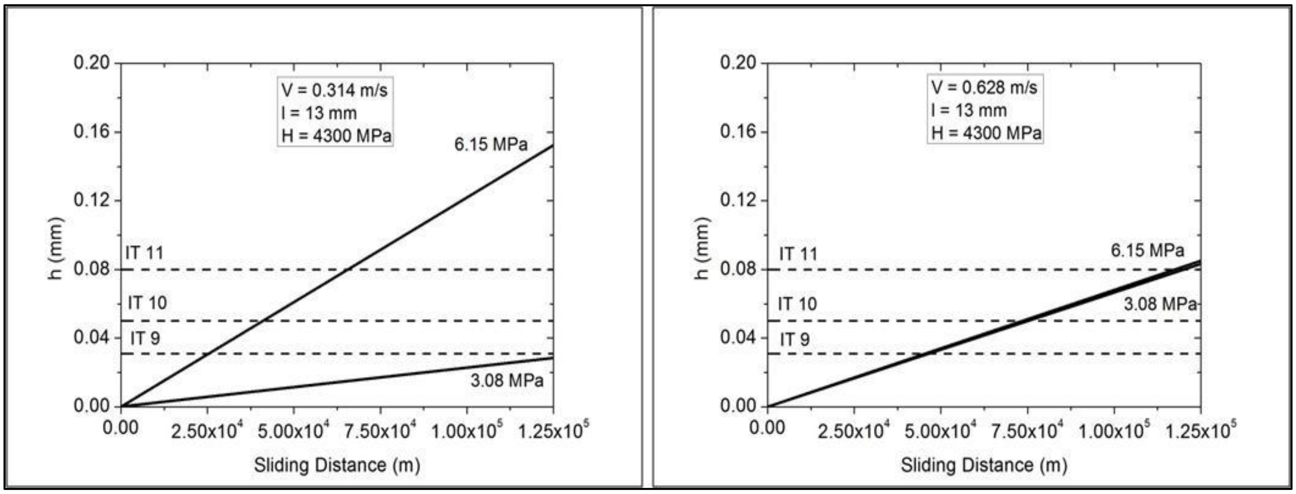

Figure 4.1.25. Wear depth vs. sliding distance of 73-DAE1-HD at 0.314 m/s and 0.628 m/s with an increased contact length

At lower speed, 73-DAB1-HD is able to meet the failure criterion for all the required tolerance classes at the lower pressure, and the one defined by ISO IT11 class at the higher pressure. At the higher speed, it meets the failure criterion when the required tolerance class is ISO IT 11 and ISO IT 10 at the lower pressure and ISO IT 11 at the higher pressure. 73-DAE1-HD meets the failure criterion for all the required tolerance classes only at the lower speed and the lower pressure, whilst in all the other conditions it fails.

The higher wear resistance of 73-DAB1-HD resulting from the lower amount of Ni-rich austenite has a practical significance in the cases here proposed. The design approach here proposed allows an evaluation of the different performances of the two materials to be evaluated in any other conditions.

4.1.3 Summary

In the first part of the work, dry sliding wear behavior of two high density sinterhardened PM steels, one with and one without Ni, was investigated. In the microstructure of the steels studied, the prevailing constituent was martensite, with minor amounts of bainite and, in the Ni alloyed steel, of Ni-rich austenite. Wear tests were carried out in different load and sliding speed conditions. The wear resistance depended on the formation and stability of a protective oxide layer on the contact surface according to the well known mechanism of the “low sliding velocity oxidative wear” proposed by Stott. The presence of the soft Ni-rich austenite in the Ni-alloyed steel prevented its formation due to localized plastic deformation (mechanical instability), and therefore the Ni-free steel showed a better wear resistance.

The results of the wear tests were used as a knowledge base for the definition of a design procedure for parts subject to dry sliding wear in application. As a failure criterion, the maximum allowable wear depth was chosen based on the permissible wear perpendicular to the contact surface as required by the ISO IT9, IT10, IT11 tolerance classes. The influence of load, in terms of mean pressure, and of sliding speed on wear depth was calculated and the possibility to improve the performance of parts subject to dry sliding wear by adapting the microhardness (material) and the contact length (geometry) was discussed.

A reliable database is a precondition for any design methodology. The correlation between the wear coefficient K and load is ambiguous at the lower speed, whilst it is reliable at the higher speed. The practical application of the proposed design criterion requires extensive experimental work to obtain a reliable K vs. F correlation.

After noticing the negative effect of Ni on dry sliding behavior of PM steels, in the second part two Ni alloyed sintered and carburized steels was studied in different conditions of force and sliding speed, in order to investigate the influence of the Ni amount on dry sliding behavior of PM steels.

Wear resistance of the material containing the smaller amount of Ni is higher in all the conditions investigated. The wear mechanisms depend on force and sliding speed. At the lower force and sliding speed, an oxidative wear is observed, while in the other conditions wear is adhesive. The amount of the soft Ni-rich austenite influences the stability of the oxide layer in oxidative wear, and the load bearing capacity of the materials in adhesive wear, and this result in a better wear resistance in the material with the smaller Ni content.

Also in the second part of the work a design procedure was proposed, based on the results of the wear tests, in order evaluate the practical significance of the differences between the two materials. A failure criterion was defined, in terms of maximum allowable wear thickness, with reference to the dimensional tolerances of the parts considered. The wear thickness calculated from the wear coefficient was compared to the maximum allowable thickness, and an effective significant difference between the two materials was concluded.

The results of the present investigation clearly indicates that in dry sliding wear the Ni content of the sintered steels have a significantly negative effect.

4.2 Contact Fatigue

4.2.1 The Model

Fatigue crack nucleation is anticipated by local plastic deformation, which occurs when the maximum local stress σ exceeds the yield strength of the matrix σ_{yo}.
The maximum local stress σ is calculated by equation (14) [90],

$$\sigma = \tau_{max}\beta_k/\phi \qquad (14)$$

where $\tau_{\max}$ is the maximum shear stress [MPa], β_k is the notch effect coefficient, which depends on the shape coefficient of pores K_t, and ϕ is the fraction of load bearing section, which depends on the amount and shape of the pores, and will be defined in the following.

The calculation of the maximum shear stress $\tau_{\max}$ is made by considering two solid cylinders held in contact by a force F uniformly distributed along the cylinder length l, according to the theory of the elastic contact (Hertzian theory).

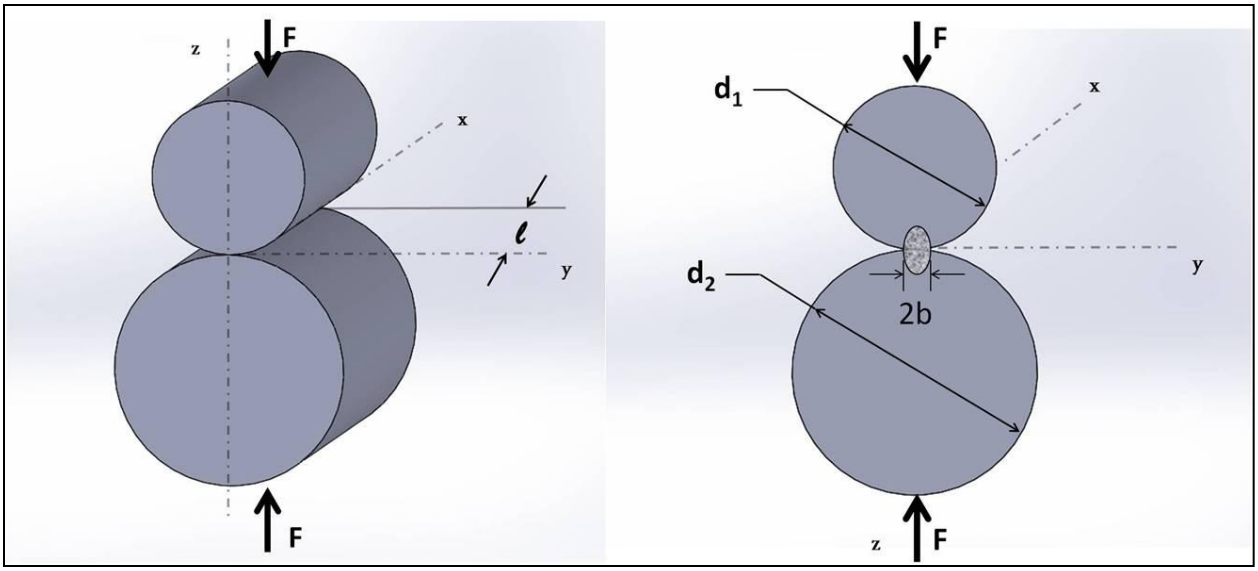

Figure 4.2.1. Two cylinders in contact [91]

The maximum shear stress is calculated by equation (15)

$$\tau_{\max} = \begin{cases} \tau_{xz} = \frac{\sigma_z - \sigma_x}{2} \text{ for } 0 \leq \zeta_b \leq 0.436 \\ \tau_{yz} = \frac{\sigma_z - \sigma_y}{2} \text{ for } 0.436 \leq \zeta_b \end{cases} \qquad (15)$$

where σ_x and σ_y are the stresses along x and y axis, respectively, and σ_z is the dominant stress along the z axis (parallel to the applied force), given by equations (16) to (18):

$$\sigma_x = -2v\, P_{\max} \left[\sqrt{1 + \zeta_b^2} - |\zeta_b| \right] \qquad (16)$$

$$\sigma_y = -P_{\max} \left[\left(\frac{1 + 2\zeta_b^2}{\sqrt{1 + \zeta_b^2}} \right) - 2|\zeta_b| \right] \qquad (17)$$

$$\sigma_z = -P_{\max} \frac{1}{\sqrt{1 + \zeta_b^2}} \qquad (18)$$

Parameter ζ_b in equations (15) to (18) is defined by equation (19)

$$\zeta_b = \frac{z}{b} \qquad (19)$$

where z is the depth from the surface [m] and b is the half of the contact width [m].

The maximum contact pressure P_{max} between the cylinders acts along a longitudinal line at the center of the rectangular contact area having width b, and is defined as:

$$P_{max} = \frac{2\,F}{\pi\,b\,l} \qquad (20)$$

The width of the contact area is given by

$$b = K_b\sqrt{F} \qquad (21)$$

$$K_b = \left[\frac{2}{\pi l}\frac{\frac{1-v_1{}^2}{E_1}+\frac{1-v_2{}^2}{E_2}}{\frac{1}{d_1}+\frac{1}{d_2}}\right]^{1/2} \qquad (22)$$

where F is the applied Force [N], v_1, v_2 are the Poisson's ratios and, E_1, E_2 are the elastic moduli of the two materials [Pa], d_1, d_2 are the diameters and l is the length (height) of the cylinders 1 and 2 ($l_1 = l_2$ assumed) [m]. Based on the Poisson's ratio of 0.3 for counterface disc and 0.27 for sintered discs, τ_{max} is maximum for $\zeta_b = \frac{z}{b} = 0.786$ and $0.3P_{max}$. [33].

Figure 4.2.2 shows the ratio to maximum pressure of the stresses along different axis and of the maximum shear stress versus z/b.

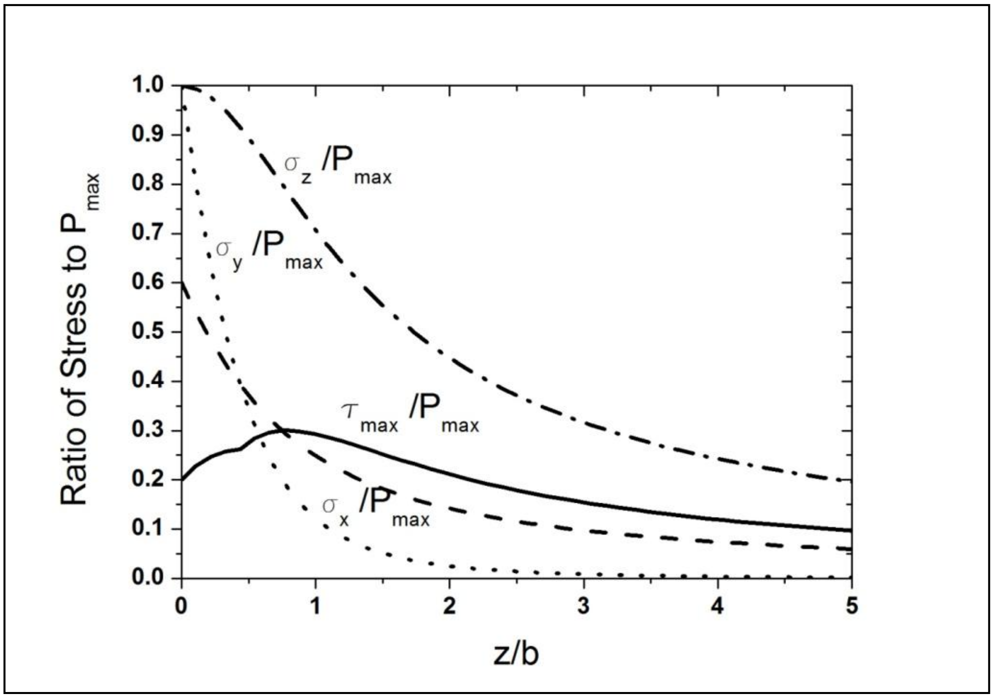

Figure 4.2.2. Stresses and maximum shear stress normalized by the maximum pressure [91]

The notch effect coefficient β_k is calculated by equation (23) [90]:

$$\beta_k = (K_t - 1)\eta + 1 \qquad (23)$$

where K_t is the shape coefficient of pores, which is about 3 [90] and η is the coefficient for matrix structure: it is 0.3 for ferritic, 0.5 for pearlitic and 0.7 for heat treated steels [90]. Thus the value 0.7 was assumed, resulting in β_k equal to 2.4 for the tested materials.

Another parameter which influences the maximum local stress is the fraction of load bearing section, ϕ. Several methods were proposed to determine ϕ: from porosity [92-94], from the elastic modulus [95], from the extension of the fractured areas on the fatigue or low temperature impact fracture surfaces [96]. In this work, the method proposed by Molinari et al [97] was used. The fraction of load bearing section is calculated by equation (24);

$$\phi = [1 - (5.58 - 5.7f_{circle})\varepsilon]^2 \qquad (24)$$

where ε is the fractional porosity of the material and f_{circle} is the shape factor of pores, calculated by equation (25);

$$f_{circle} = (4\pi A)/p^2 \qquad (25)$$

where A is the area [m^2] and p is the perimeter [m] of the pore, measured by image analysis of the metallographic sections.

The matrix yield strength of the material is calculated by equation (26);

$$\sigma_{Yo} = \mu HV/B \qquad (26)$$

where μHV is the microhardness of the material and B is a constant; Bell and Sun [98] proposed B=4.2 for heat treated steels.

4.2.2 Rolling-sliding tests

Rolling sliding tests were done on 73-DDH2-HD, 73-DAE2-HD and 73-AS4300C75 to investigate their rolling contact fatigue behavior. These are the typical materials that are used for the parts which are subjected to contact fatigue (CF). Figure 4.2.3 shows the microstructures of the investigated materials.

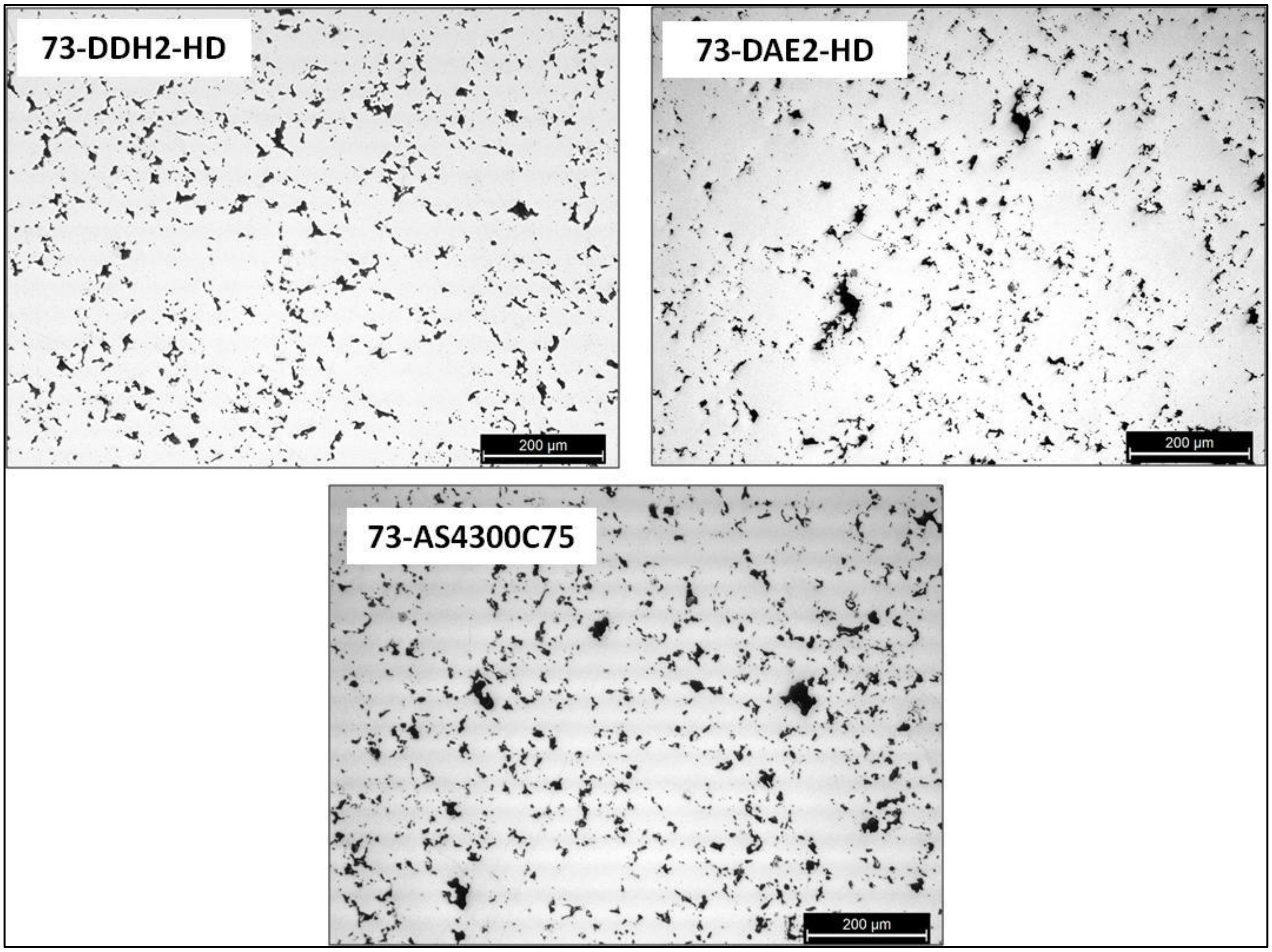

Figure 4.2.3. Microstructure of 73-DDH2-HD, 73-DAE2-HD and 73-AS4300C75

For the theoretical calculation of the stress the fraction of load bearing section ϕ had to be calculated. Calculations were done on the basis of equations (24) and (25).

f_{circle} is calculated from the image analysis of the microstructure of the materials reported in Figure 4.2.3. The relation between the equivalent diameter D_{eq} and f_{circle} are shown in Figure 4.2.4 for all three materials.

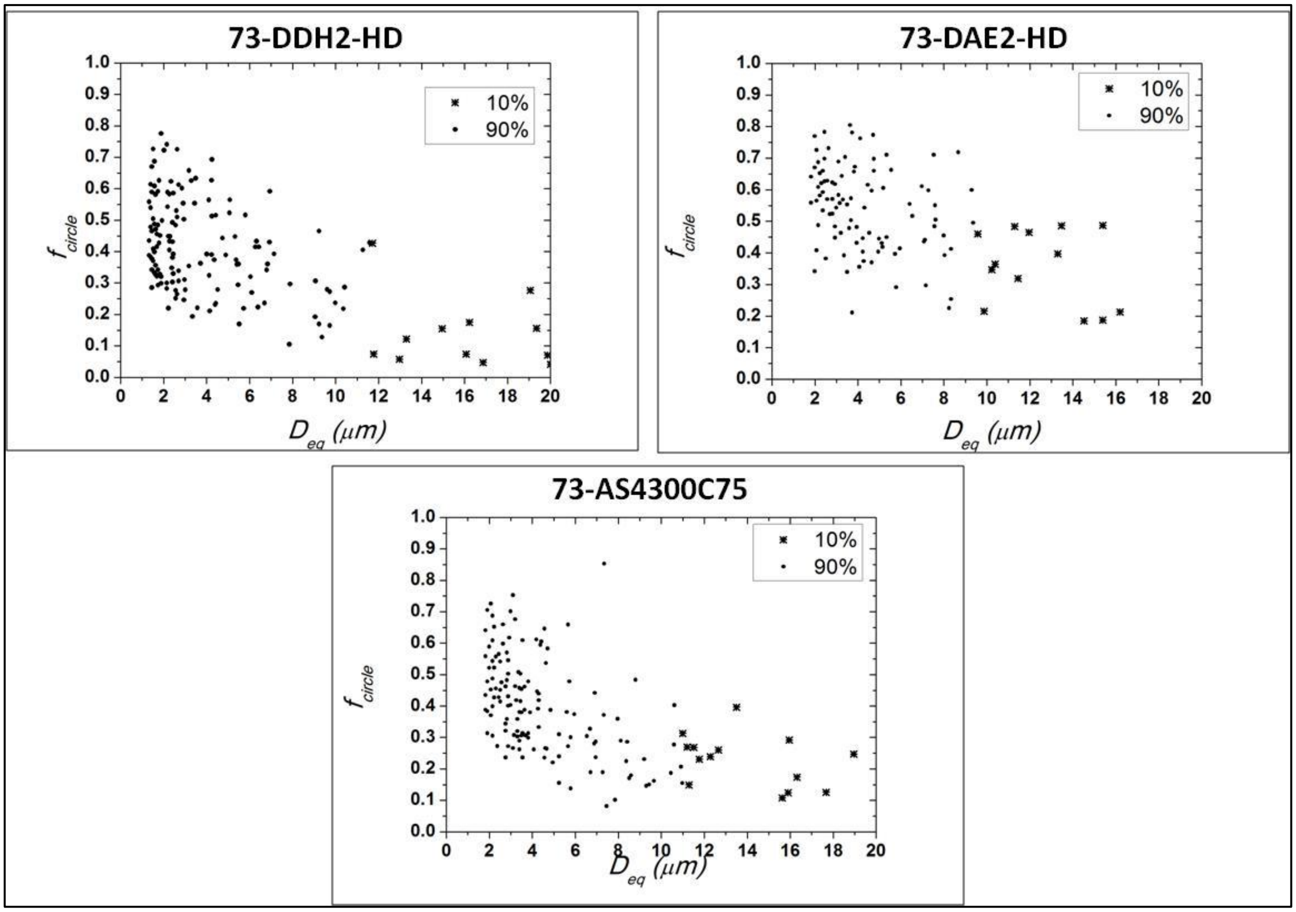

Figure 4.2.4. Equivalent diameter vs. f_{circle} distribution in 73-DDH2-HD, 73-DAE2-HD and 73-AS4300C75

Figure 4.2.4 shows that the large pores are the more irregular. Therefore the fraction of the load bearing section was calculated using the mean f_{circle} derived considering both the whole of the pore population and the largest pores corresponding to 10% of the pore population (highlighted in Figure 4.2.4). The results are reported in Table 4.2.1 and show that ϕ is significantly smaller in the latter case.

Material	**ϕ (100%)**	**ϕ (10%)**
73-DDH2-HD	0.64	0.52
73-DAE2-HD	0.72	0.62
73-AS4300C75	0.64	0.53

Table 4.2.1. Fraction of load bearing section of 73-DDH2-HD, 73-DAE2-HD and 73-AS4300C75

The microstructures of the materials are shown in Figure 4.2.5.

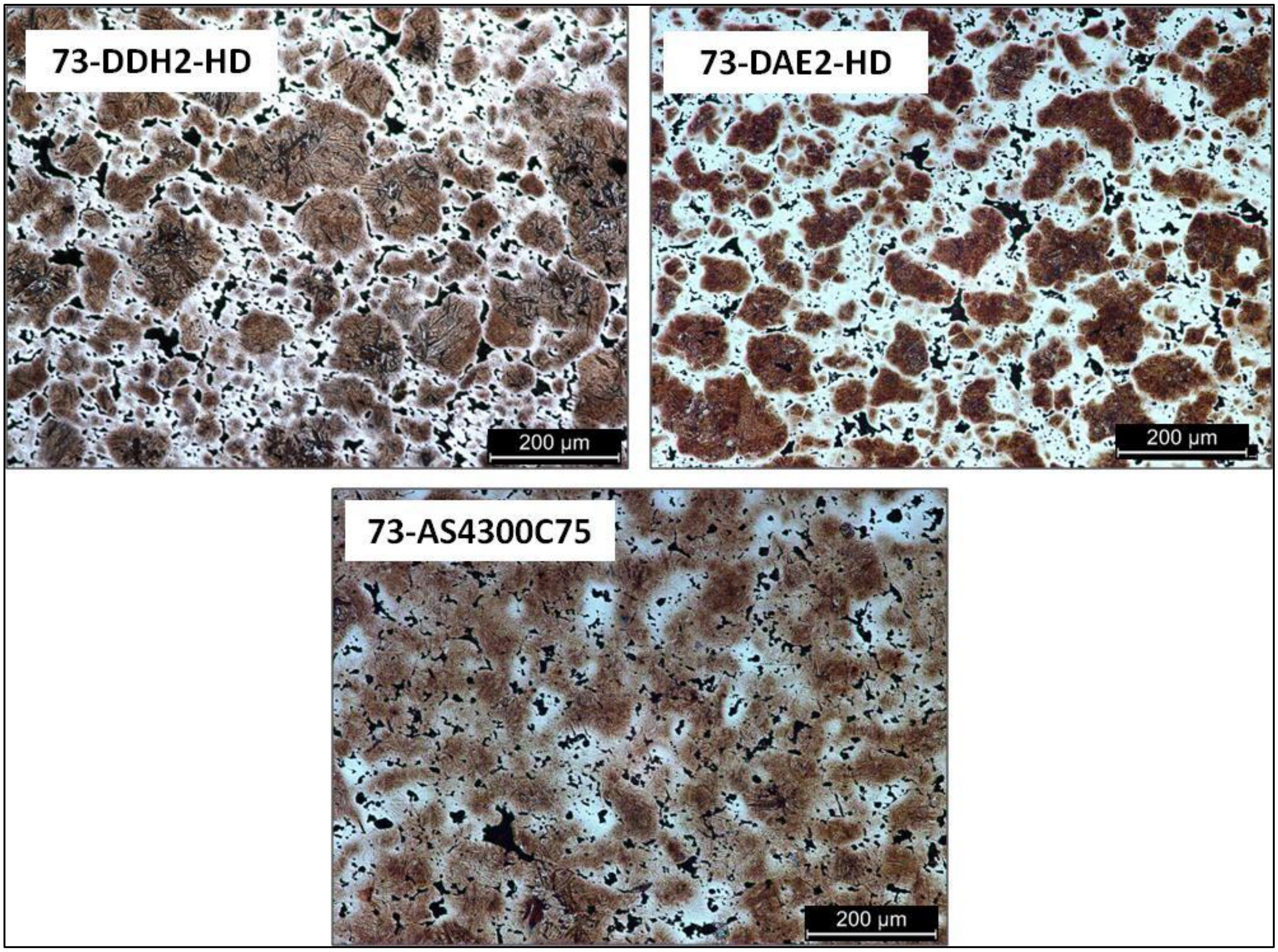

Figure 4.2.5. Microstructures of 73-DDH2-HD, 73-DAE2-HD and 73-AS4300C75 after proper etching

The microstructure of 73-DDH-HD consists of lower bainite (dark) and martensite (bright), 73-DAE2-HD has martensite and Ni-rich austenite (white) and 73-AS4300C75 is mostly martensitic with some Ni-rich austenite (white). For the calculation of the matrix yield strength, microhardness of the materials were measured within a 1 mm thick surface layer and the microhardness profiles are shown in Figure 4.2.6. Measurements were done after etching on different constituents such as martensite, lower bainite and Ni-rich austenite. Mean microhardness was then calculated from those results by considering weighted mean in the basis of the microstructures of the materials.

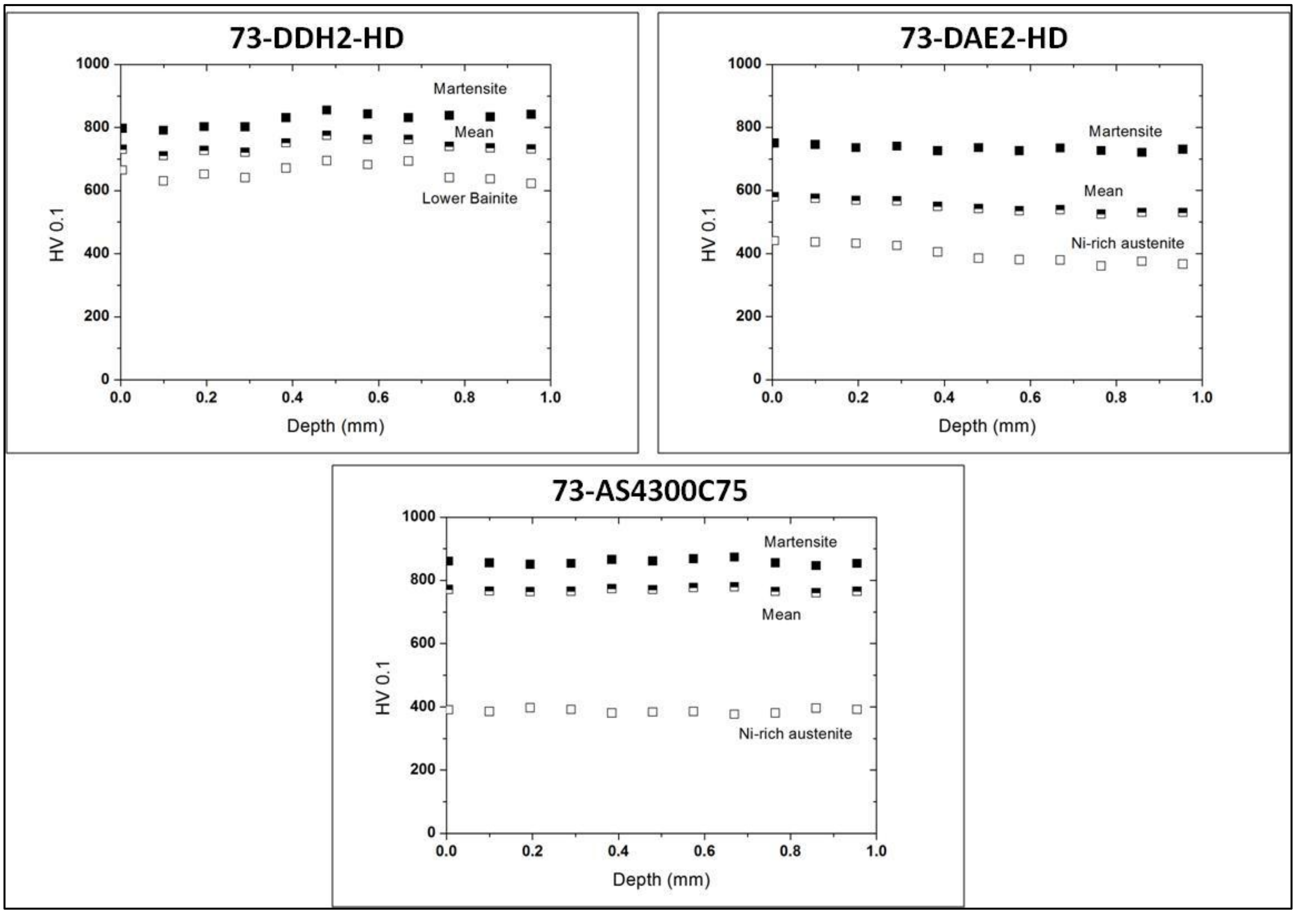

Figure 4.2.6. Microhardness profiles of 73-DDH2-HD, 73-DAE2-HD and 73-AS4300C75

Theoretical prediction of the nucleation of the contact fatigue crack was made with two different approaches for what concerns microhardness (to calculate the matrix yield strength) and the pores to calculate the fraction of the load bearing section:

a) the mean microhardness and the whole of the pore population (mean approach);

b) the mean microhardness and large pores corresponding to 10% of the pore population.

The maximum local stress and the matrix yield strength in a 1 mm thick layer are plotted in Figure 4.2.7 for 73-DDH2-HD in case of a mean pressure of 600 MPa, as by these two approaches.

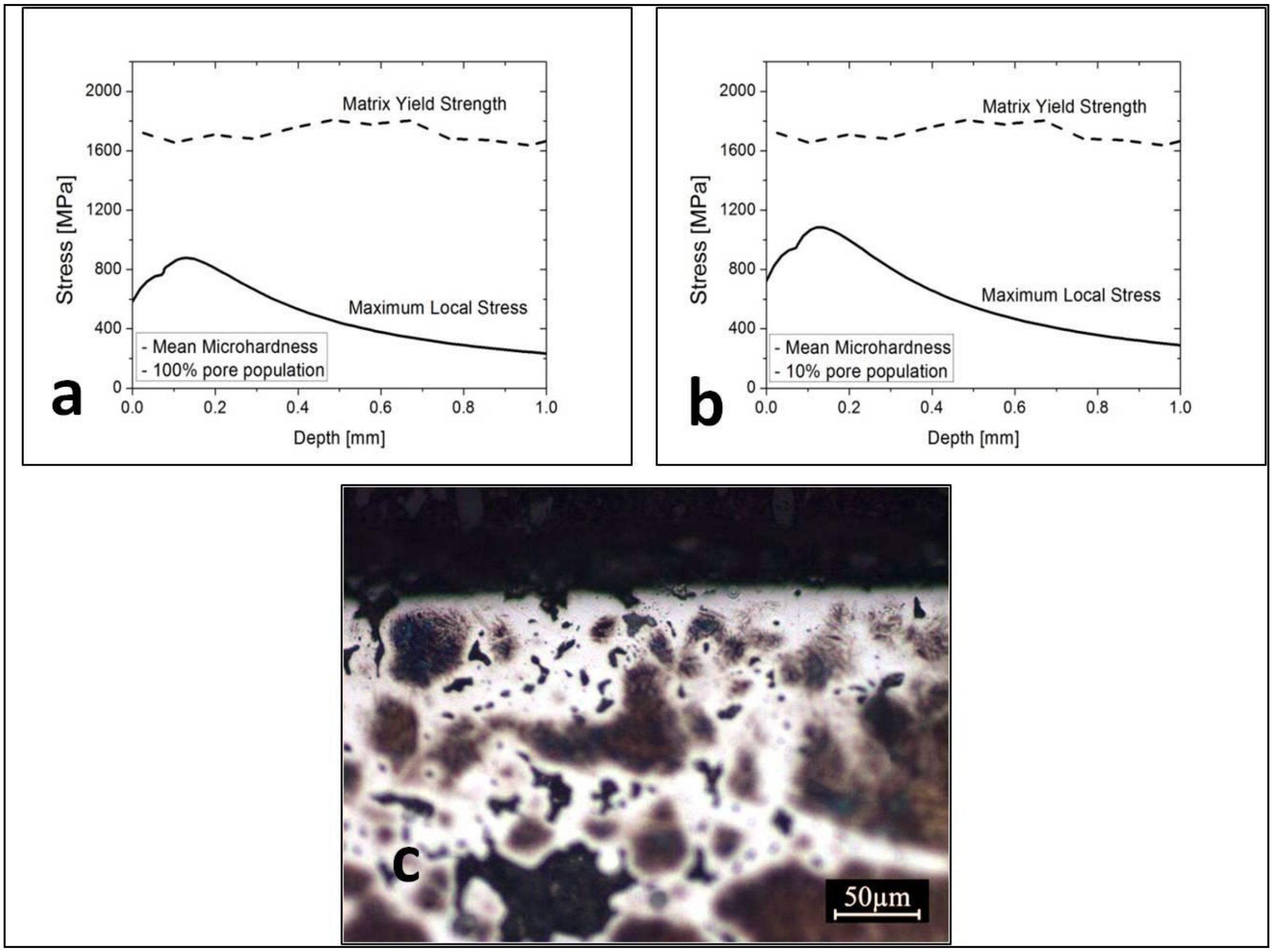

Figure 4.2.7. Theoretical predictions for 73-DDH2-HD at 600 MPa mean pressure and microstructure after the wear test

At 600 MPa mean pressure leads to the results shown in Figure 4.2.7. The comparison between the matrix yield strength calculated using the mean microhardness and the maximum local stress calculated using both the whole population and the large pores corresponding to 10% of the pore population does not predict local plastic deformation and, in turn, the nucleation of the fatigue crack. After the wear test performed with 600 MPa mean pressure the specimen does not show any crack, confirming the theoretical predictions.

The same calculations were done for 73-AS4300C75 at 600 MPa mean pressure and again after the tests specimens do not show any crack again confirming the theoretical predictions.

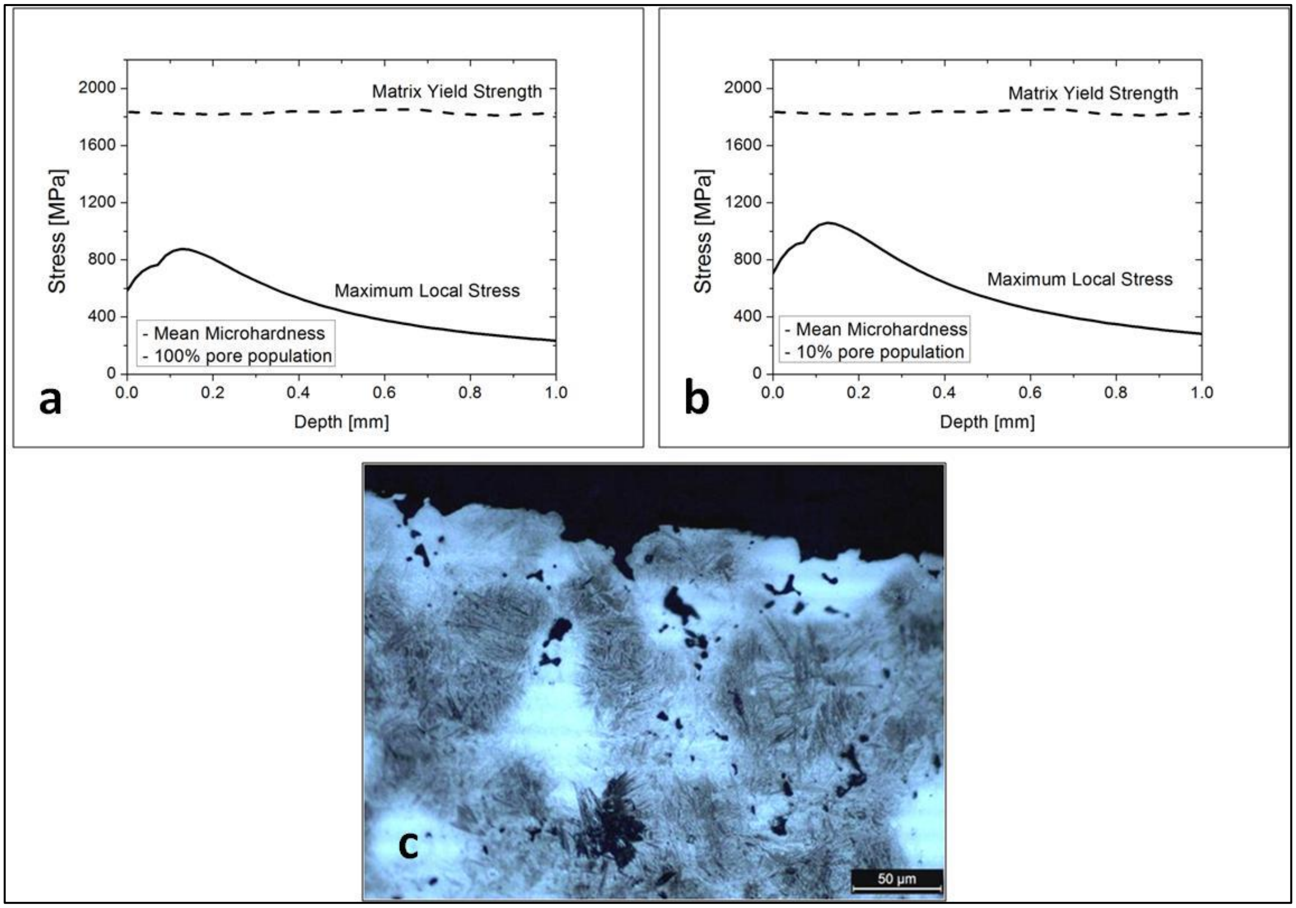

Figure 4.2.8. Theoretical predictions for 73-AS4300C75 at 600 MPa mean pressure and microstructure after the wear test

For 73-DAE2-HD, the same approach was done at the beginning by considering the mean microhardness and the whole population and the mean microhardness and large pores corresponding to 10% of the pore population. However, after the tests, cracks were observed. Therefore approach was improved by considering by following two predictions in addition to the a) and b) which were previously mentioned:

c) the microhardness of the microstructural constituent where the large pores are localized (Ni austenite) and the whole of the pore population.

d) the microhardness of the microstructural constituent where the large pores are localized (Ni austenite) and large pores corresponding to 10% of the pore population (local approach).

The maximum local stress and the matrix yield strength in a 1 mm thick layer are plotted in Figure 4.2.9 for 73-DAE2-HD in case of a mean pressure of 600 MPa, as by the four approaches.

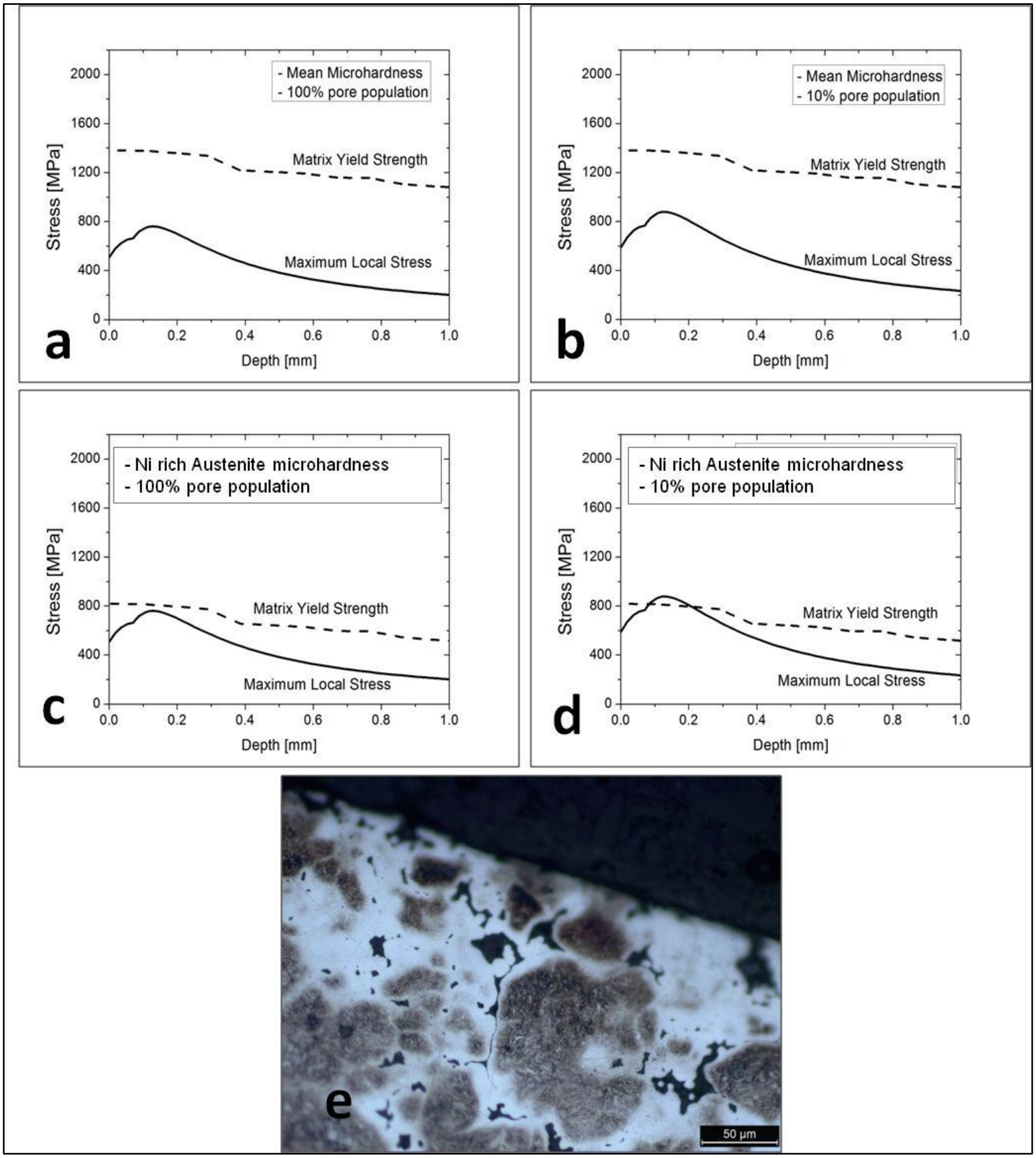

Figure 4.2.9. Theoretical predictions for 73-DAE2-HD at 600 MPa mean pressure and microstructure after the rolling sliding tests

In the first three cases, the model does not predict any fatigue crack, whilst in the fourth one (local approach) plastic deformation is predicted at a distance between 0.1 and 0.2 mm from the surface, since the yield strength of the Ni-rich constituent is lower than the mean one. A fatigue crack is therefore expected to nucleate. Figure 4.2.9e shows the microstructure of the subsurface layers after a rolling-sliding test with a mean pressure of 600 MPa; it reveals the presence of some cracks connecting the large pores in the Ni-rich constituent, at a distance from the surface corresponding to the Hertzian depth, confirming the prediction obtained with the local approach. The calculation based on the mean characteristics of the material, both in terms of pores and of microhardness, fails in predicting the CF behavior.

As it can be seen from calculations, differently from 73-DAE2-HD, 73-DDH2-HD and 73-AS4300C75 were expected to resist higher mean pressures. Therefore new calculations were made for increasing the mean pressure up to 1GPa.

The results for 73-DDH2-HD are shown in Figure 4.2.10a, where large pores corresponding to 10% of the pore population are used to calculate the fraction of load bearing section. Plastic deformation is expected but, as shown in figure 4.2.10b, no cracks were observed after the wear test at the same mean pressure. Discrepancy may be attributed to the use of the mean microhardness to calculate the matrix yield strength; indeed the large pores are localized in the martensite (as previously mentioned), which is the harder constituent. If the matrix yield strength is calculated on the basis of the martensite microhardness, no plastic deformation is predicted (figure 4.2.10c) and the agreement between theoretical calculation and experimental evidence is attained.

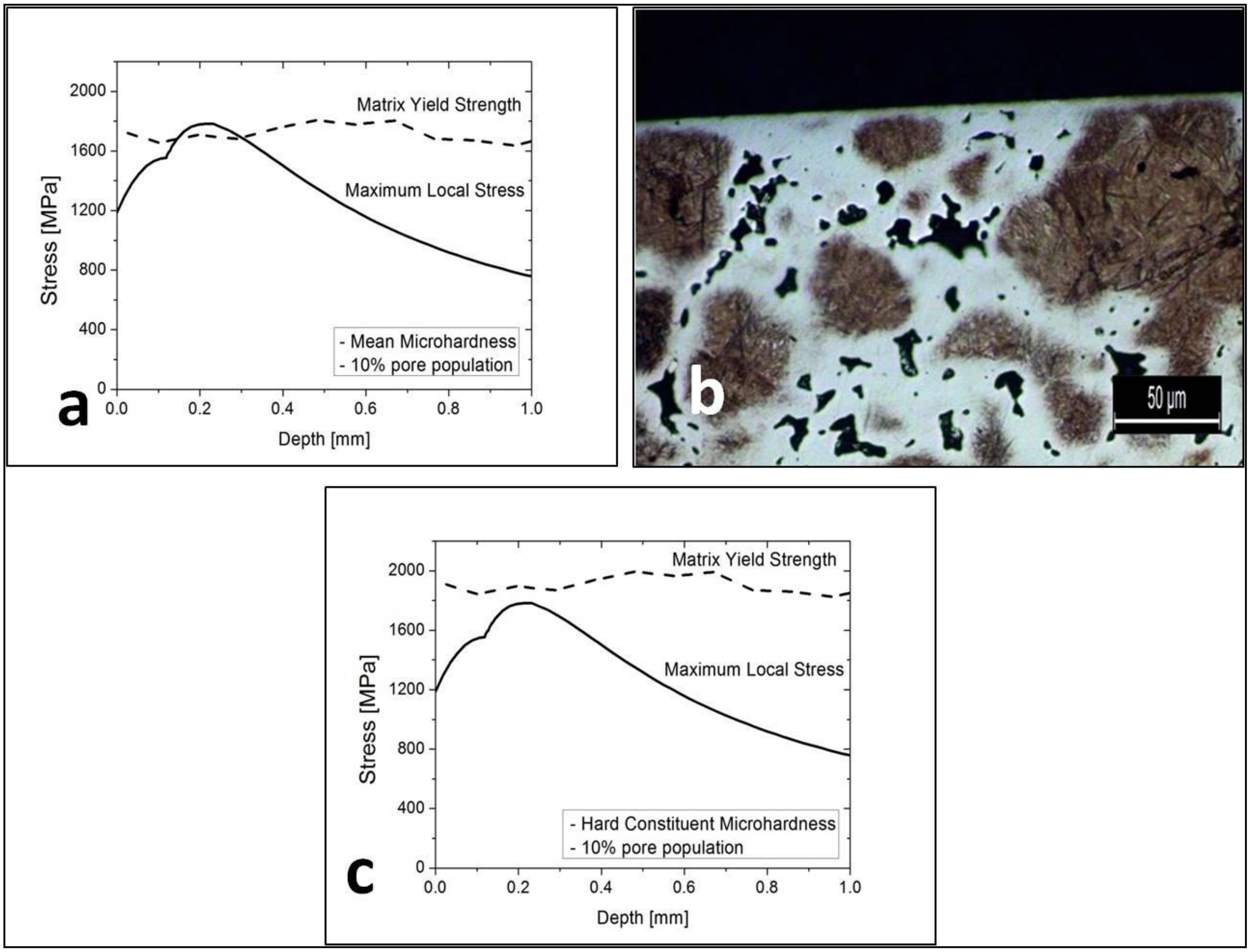

Figure 4.2.10. Theoretical predictions for 73-DDH2-HD at 1 GPa mean pressure and microstructure after the wear test

In addition, the results for 73-AS4300C75 are shown in Figure 4.2.11a, where large pores corresponding to 10% of the pore population are used to calculate the fraction of load bearing section. Plastic deformation was expected and as shown in figure 4.2.11b, cracks were observed after the wear test at the same mean pressure. In case of 73-AS4300C75, the large pores are not localized in any specific constituent so use of mean microhardness for the calculation of the matrix yield strength is in agreement between theoretical calculation and experimental evidence is attained.

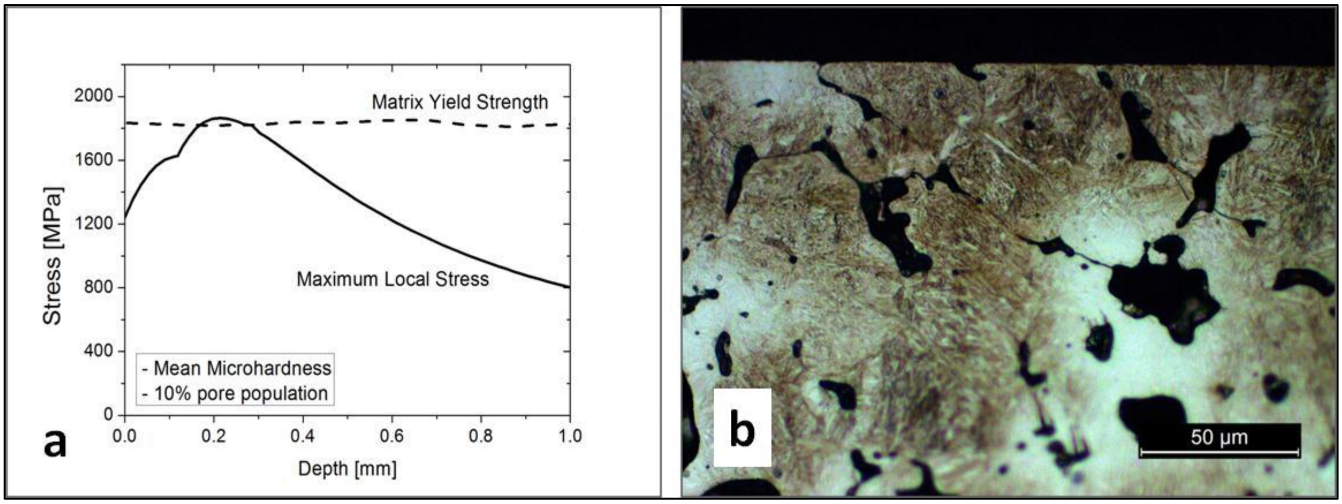

Figure 4.2.11. Theoretical predictions for 73-AS4300C75 at 1 GPa mean pressure and microstructure after the wear test.

After tests at 1 GPa mean pressure on materials 73-DDH2-HD and 73-AS4300C75, it has been observed that the former can perform better. Therefore, the theoretical calculations were made for a higher pressure, at 1.1 GPa and reported in Figure 4.2.12.

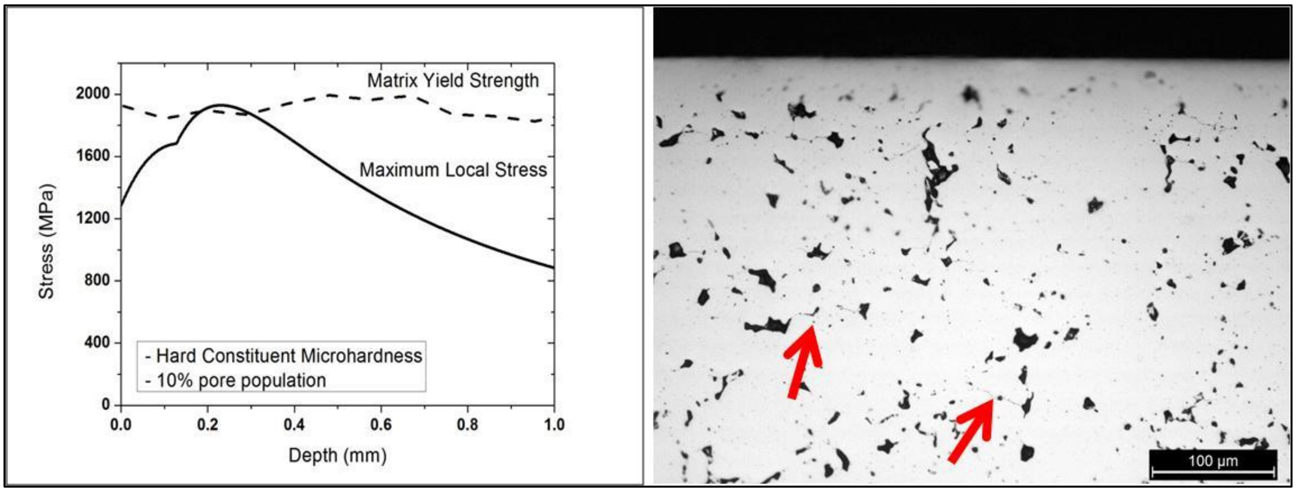

Figure 4.2.12. Theoretical predictions for 73-DDH2-HD at 1.1 GPa mean pressure and microstructure after the wear test

As it can be seen from Figure 4.2.12, theoretical calculations predicted a crack nucleation in 73-DDH2-HD at 1.1 GPa mean pressure and the experiments validated the prediction, cracks were observed.

Further analysis were also done on 73-AS4300C75 by decreasing the mean pressure to 0.8 GPa since there was a failure at 1 GPa mean pressure. Theoretical calculations were done and experiments validated the theoretical approach which is shown in Figure 4.2.13.

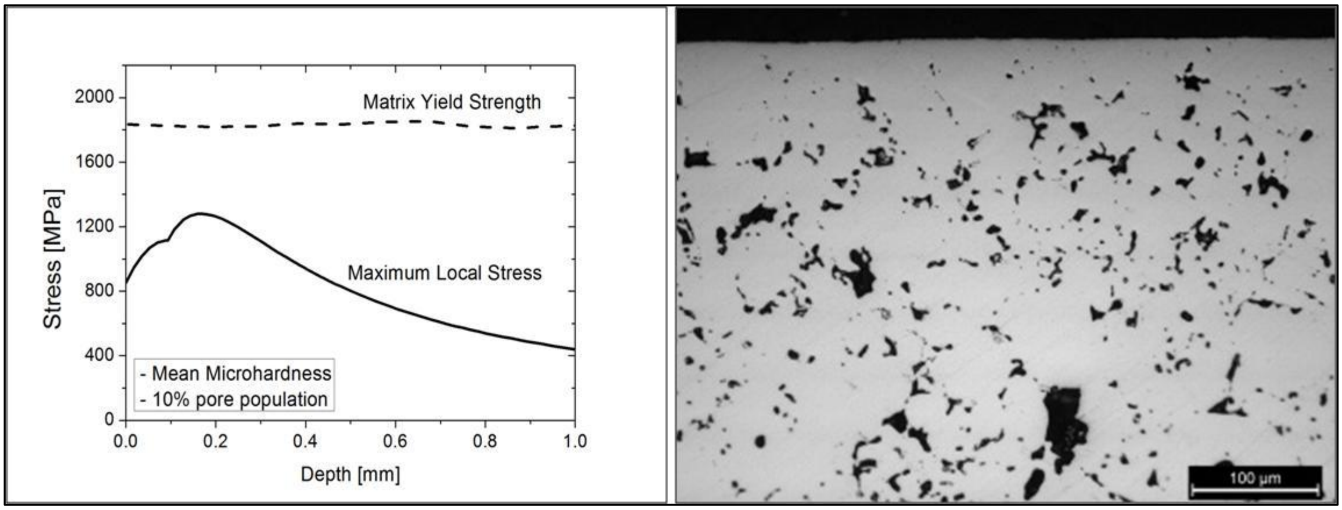

Figure 4.2.13. Theoretical predictions for 73-AS4300C75 at 0.8 GPa mean pressure and microstructure after the wear test

Table 4.2.2. summarizes the theoretical predictions (local approach) and experiments validations after all tests. "No" represents no crack expectations in theoretical prediction and no crack observed in experimental results. On the other hand, "Yes" represents the possible crack prediction by theory and observed crack in experimental results.

Material Name	**Mean Pressure (GPa)**							
	0.6		**0.8**		**1.0**		**1.1**	
	Theoretical Prediction	**Experimental Result**	**Theoretical Prediction**	**Experimental Result**	**Theoretical Prediction**	**Experimental Result**	**Theoretical Prediction**	**Experimental Result**
73-DDH2-HD	No Cracks	No Cracks	--	--	No Cracks	No Cracks	Cracks	Cracks
73-DAE2-HD	Cracks	Cracks	--	--	--	--	--	--
73-AS4300C75	No Cracks	No Cracks	No Cracks	No Cracks	Cracks	Cracks	--	--

Table 4.2.2. Summary of theoretical predictions and experimental validations after rolling sliding tests

After all predictions were validated, theoretical approach was used to calculate the maximum limit of mean pressure that can be applied for each material; results are listed in Table 4.

Material	**Mean Pressure Limit (GPa)**
73-DDH2-HD	1.07
73-DAE2-HD	0.53
73-AS4300C75	0.97

Table 4.2.3. The maximum limit of mean pressure for 73-DDH2-HD, 73-DAE2-HD and 73-AS4300C75

4.2.3 Shot Peening

4.2.3.1 Ceramic vs. steel/ceramic Shot peening

To select the proper shot peening method between the ceramic and steel+ceramic, the material 73-DDH2-HD was chosen since it was the best performing material in CF tests.

The residual stresses were measured till 250 µm below the surface and values for both ceramic and steel+ceramic shot peened samples are reported in Table 4.2.4.

Depth from the surface **(µm)**	**Residual Stress (MPa)**	
	Ceramic	**Steel + Ceramic**
0	-1184	-1219
50	-898	-773
100	-339	-482
150	-280	-362
200	-245	-315
250	-180	-256

Table 4.2.4. Compressive residual stresses after ceramic and steel+ceramic shot peening on 73-DDH2-HD

The effective depth of residual stresses was extrapolated from the values in Table 4.2.4 and Figure 4.2.14 shows the residual stress profile of 73-DDH2-HD.

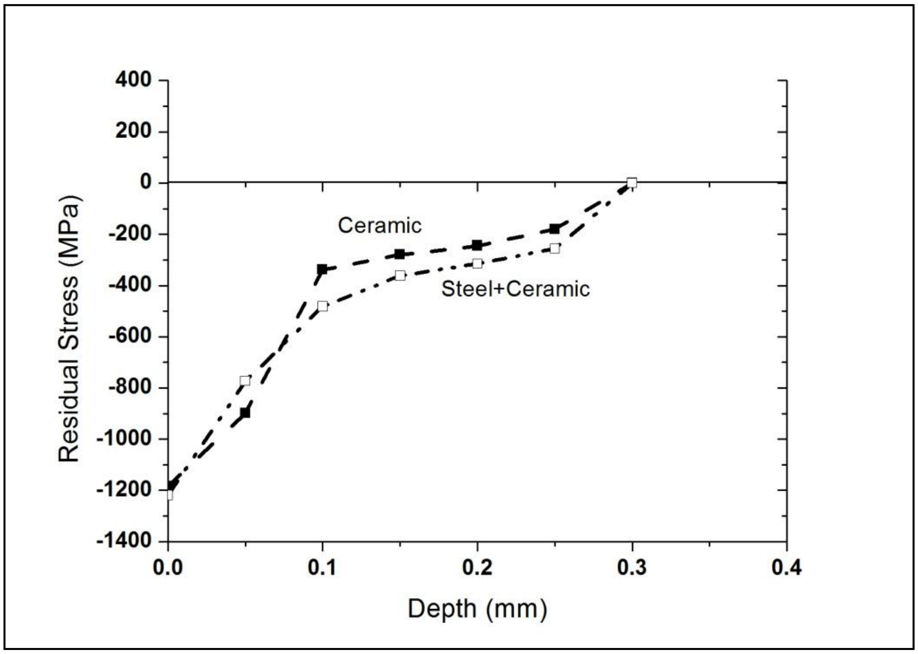

Figure 4.2.14. Residual stress profile of 73-DDH2-HD

The surface of the material was examined by both Optical and Scanning Electron Microscope and the effect on the surface morphology and the sub surfaces microstructure was compared.

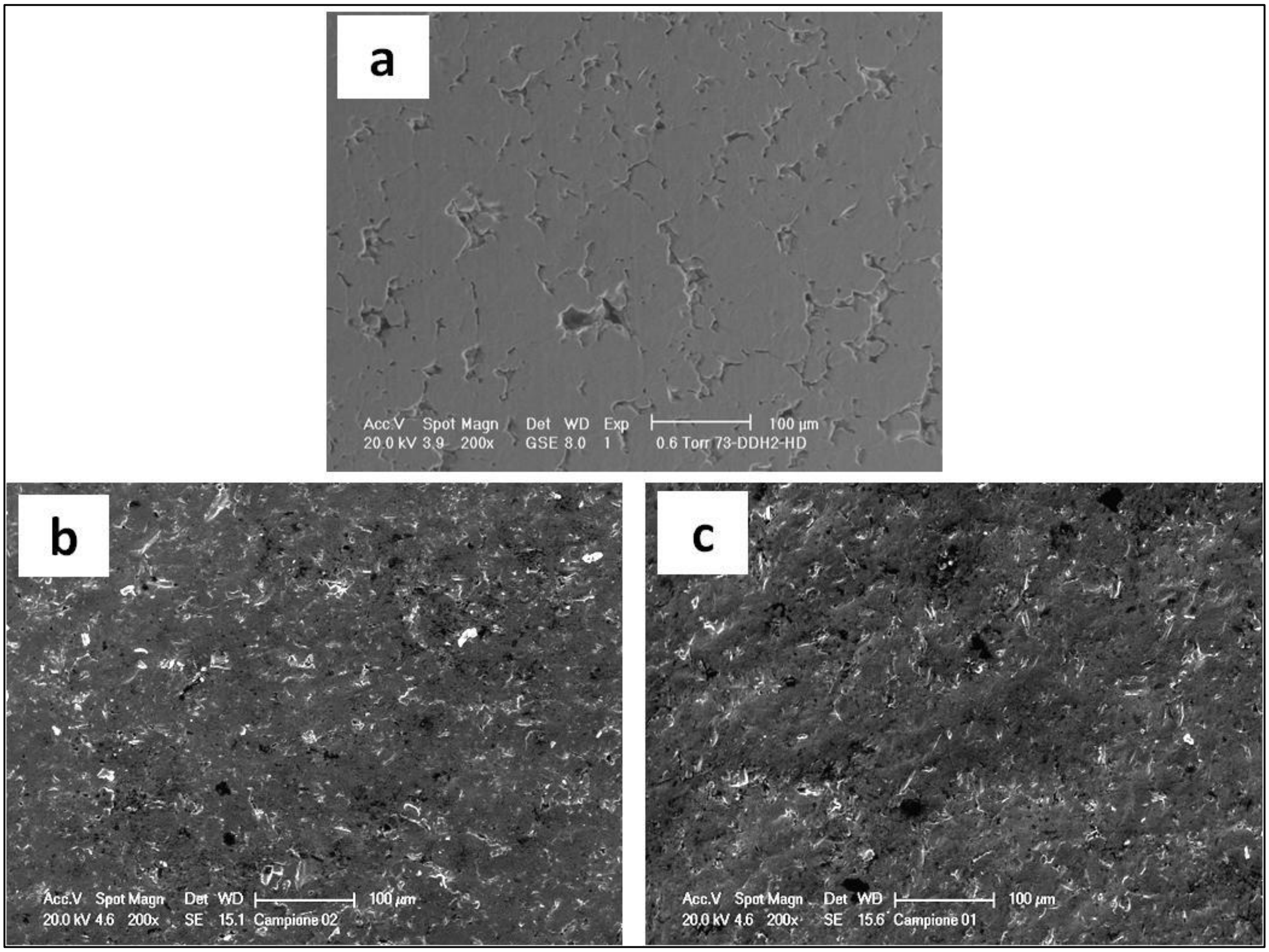

Figure 4.2.15. SEM analysis on the surface of 73-DDH2-HD a) as sintered surface b) after ceramic shot peening c) after steel+ceramic shot peening.

In Figure 4.2.15a, the pores on the surface of the material can be observed. After both shot peening methods, the pores were eliminated from the surface due to plastic deformation (Figure 4.2.15b and 4.2.15c). On the other hand, it may also be observed that the surface of the material was deformed after shot peening. This deformation caused a rough surface in comparison to the as sintered material.

This deformation on the surface was quantified by roughness measurement. Roughness, R_a, and the reduced peak height, R_{pk}, were measured in axial and tangential directions; results are shown in Table 4.2.5 and Figure 4.2.16 compares the values obtained.

	As sintered		Ceramic		Steel + Ceramic	
	Axial	**Tangential**	**Axial**	**Tangential**	**Axial**	**Tangential**
R_a [μm]	0.6	0.95	1.08	1.19	1.19	1.32
R_{pk} [μm]	0.24	0.35	0.68	1.08	1.15	1.28

Table 4.2.5. Roughness measurement results

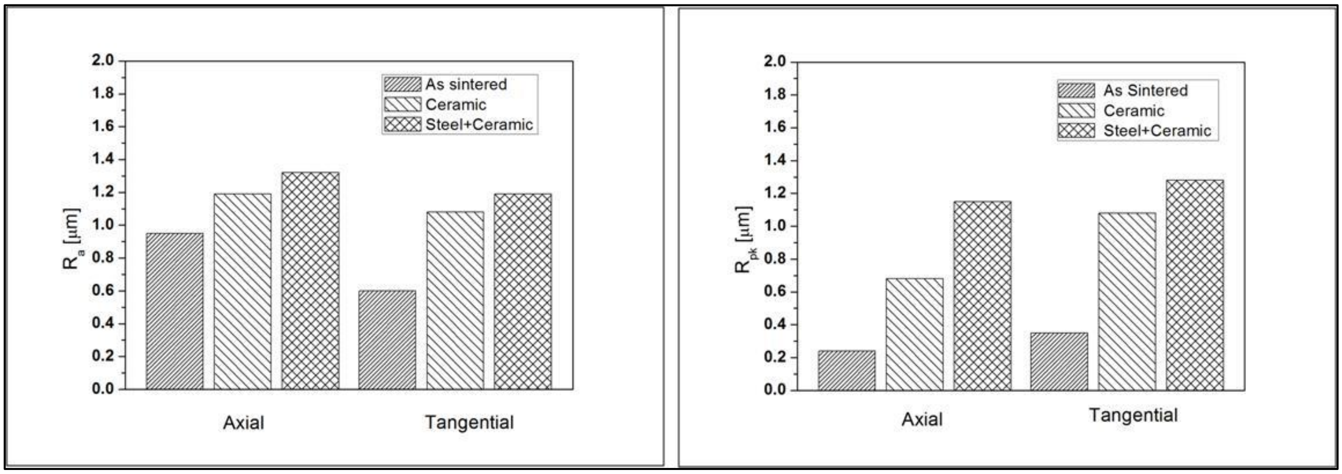

Figure 4.2.16. The comparison of R_a and R_{pk} for as sintered, after ceramic shot peening and after steel+ceramic shot peening.

It has to be considered that R_a for the porous surface is a poorly significant parameter, since it is affected by the surface pores that are considered as valleys in the calculation. Neglecting R_a of sintered disks, it may be concluded that double shot peening results in a slightly worse surface profile, since both R_a and R_{pk} are higher than in case of ceramic shot peening. This is attributed to the extensive deformation introduced by steels shots, whose effects on the surface profiles cannot be “repaired” by the subsequent ceramic shot peening.

The microstructure of the surface layers is shown in Figure 4.2.17 and 4.2.18, before and after etching.

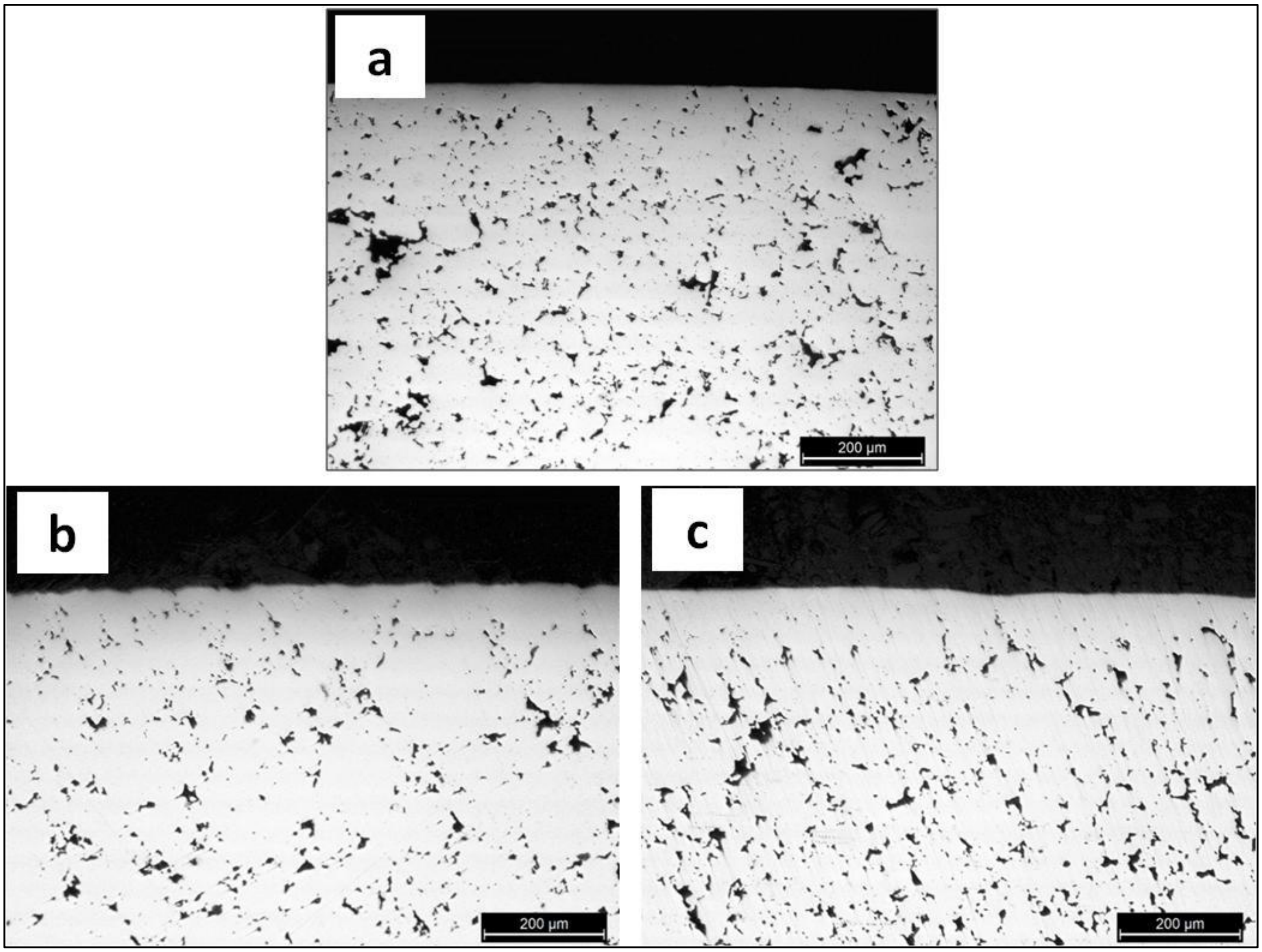

Figure 4.2.17. Microstructure of 73-DDH2-HD a) as sintered b) after ceramic shot peening c) after steel+ceramic shot peening.

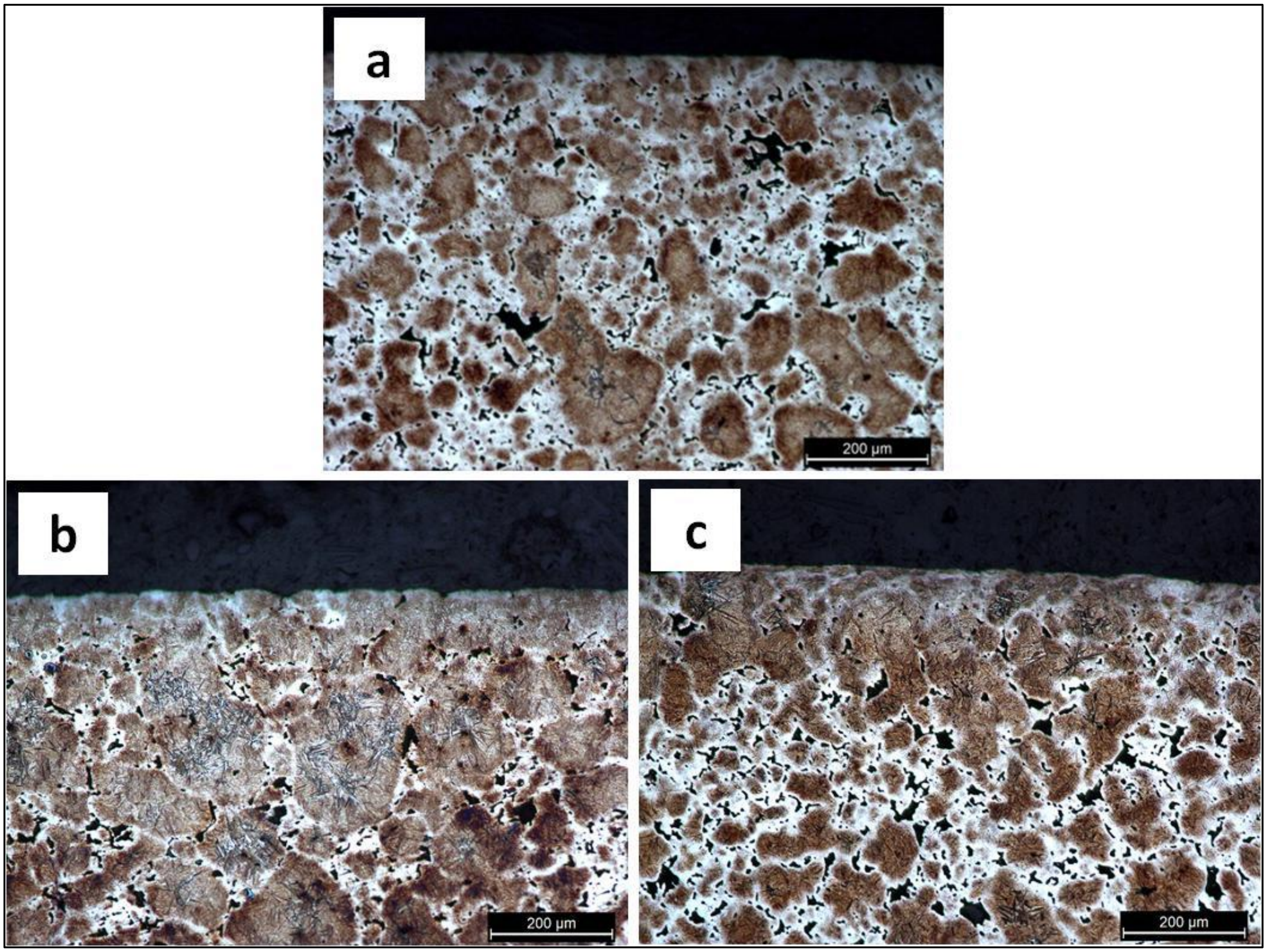

Figure 4.2.18. Microstructure of 73-DDH2-HD after etching a) as sintered b) after ceramic shot peening c) after steel+ceramic shot peening.

The effect of porosity can be seen in both figures. Both shot peened materials have relatively smaller pores close to the surface due to densification caused by plastic deformation. It results in lower porosity or smaller pores in size. Since pores got smaller or disappear after shot peening, densification takes place in the affected zone.

Porosity was measured by Image Analysis at each 50 µm intervals; Table 4.2.6 shows measured porosities in three conditions.

Depth [µm]	Porosity [%]		
	As Sintered	Ceramic Shot Peened	Steel+Ceramic Shot Peened
0	4.96	0.89	0.52
50	4.93	2.15	2.96
100	4.94	2.24	4.45
150	5.09	2.85	4.92
200	5.44	3.8	5.63
250	5.87	5.68	5.78

Table 4.2.6. Measured porosities by image analysis

The decrease of porosity in shot peened materials is clearly evident. From surface to the 50 µm depth porosity was affected dramatically by shot peening. Beyond this depth porosity started to increase and at around 250 µm it was similar to the one of as sintered discs.

The values from Table 4.2.6 were fitted by curves and the porosity profiles are shown in Figure 4.2.19.

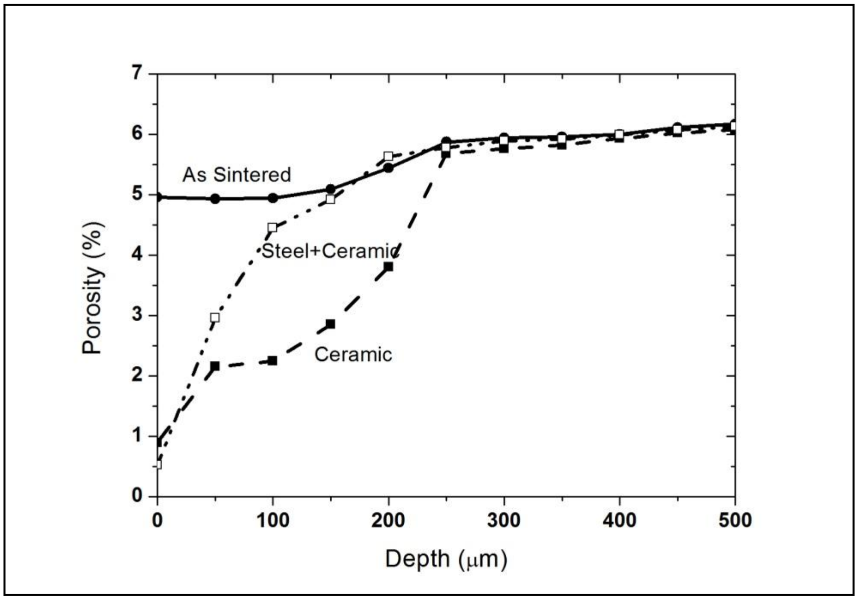

Figure 4.2.19. Porosity profiles of as sintered, ceramic shot peened and steel+ceramic shot peened material

From measured porosities profiles local densities were calculated from the theoretical density of the material; results are reported in Table 4.2.7.

Depth [µm]	**Calculated Density g/cm^3**	
	Ceramic shot peened	**Steel+Ceramic shot peened**
0-50	7.72	7.75
50-100	7.62	7.56
100-150	7.62	7.44
150-200	7.57	7.41
200-250	7.49	7.35
250-300	7.35	7.34

Table 4.2.7. Calculated densities corresponding to the measured porosities

Surface densification increases the elastic modulus of the surface layers. Therefore, elastic moduli for both ceramic shot peened and steel+ceramic shot peened materials were calculated, based on Höganäs Iron and Steel Powders for Sintered Components [14], and listed in Table 4.2.8.

Depth [µm]	**Elastic Modulus [GPa]**	
	Ceramic shot peened	**Steel + Ceramic shot peened**
0-50	171	173
50-100	166	163
100-150	166	157
150-200	163	155
200-250	160	153
250-300	152	152

Table 4.2.8. Elastic modulus of ceramic shot peened and steel + ceramic shot peened material

Elastic modulus profiles after shot peening reported in Figure 4.2.20.

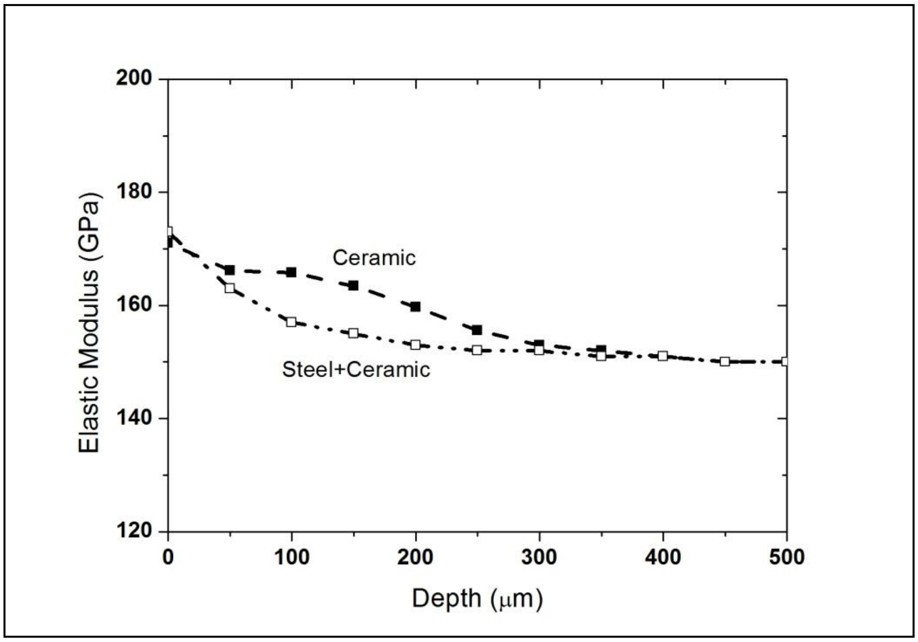

Figure 4.2.20. Elastic modulus profiles of ceramic and steel+ceramic shot peened materials

As it can be seen from Figure 4.2.20, elastic modulus is higher close to surface and decreases by going deeper from the surface after both shot peening processes. At around 300 µm elastic modulus tends to decrease to the one of the as sintered material.

Densification affects the fraction of load bearing section, ϕ. The calculation of ϕ for the surface densified layers was done by equation (24) and, as previously explained, 10% of the largest pores were considered. Table 4.2.9 show the values calculated.

Depth [µm]	**ϕ**	
	Ceramic shot peened	**Steel + Ceramic shot peened**
0	0.937	0.952
50	0.847	0.795
100	0.846	0.729
150	0.806	0.717
200	0.716	0.623
250	0.624	0.571

Table 4.2.9. Fraction of load bearing section for ceramic, steel+ceramic shot peened materials

From the values listed in Table 4.2.9, load bearing section values are interpolated and the profile was drawn and shown in Figure 4.2.21.

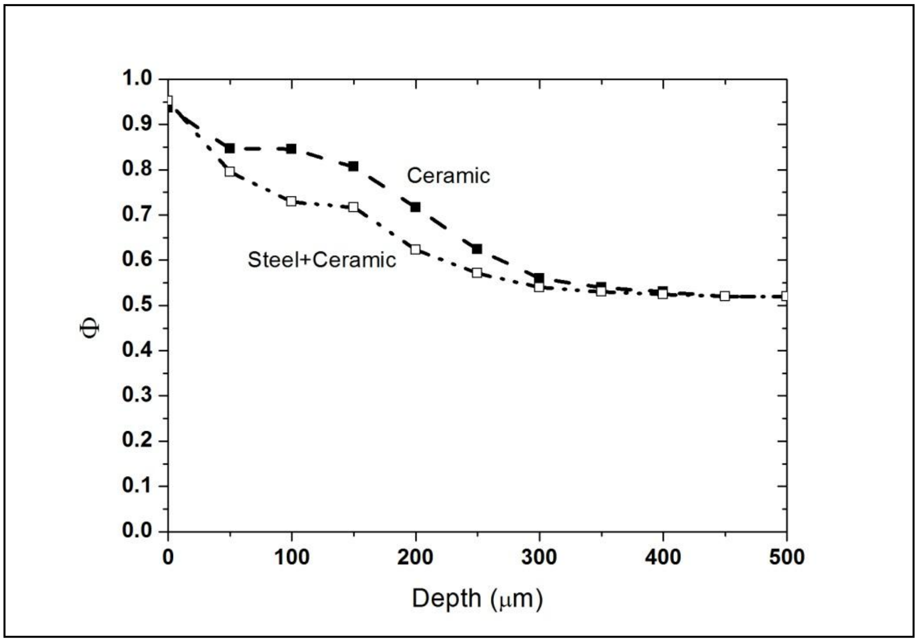

Figure 4.2.21. Fraction of load bearing section profile

In Figure 4.2.22 the maximum stress profile at 1 GPa mean pressure is drawn for both ceramic and steel+ceramic shot peened 73-DDH2-HD, by considering the profiles of the elastic modulus and of the fraction of load bearing section resulting from the surface densification.

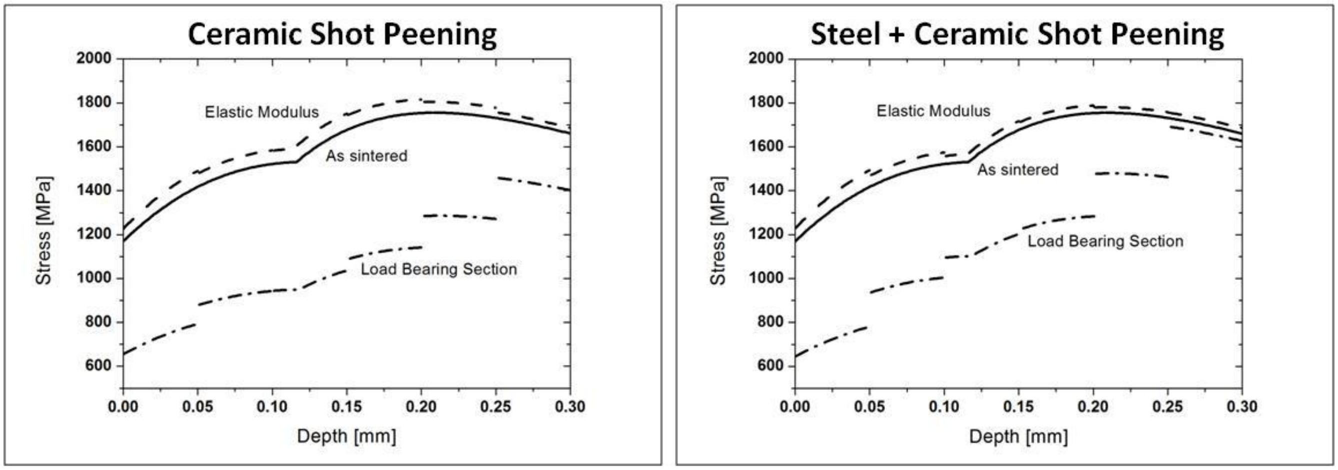

Figure 4.2.22. Stress at 1 GPa mean pressure for 73-DDH2-HD after ceramic and steel+ceramic shot peening

Starting from the curve of the sintered material (continuous line), the higher elastic modulus increases the stress slightly (dashed line), while the increase in load bearing section decreases it dramatically (dashed-dotted line).

From these values, a fitting was done to obtain a curve considering the changes both in elastic modulus and in load bearing section. These curves are shown in Figure 4.2.23, along with the residual stresses.

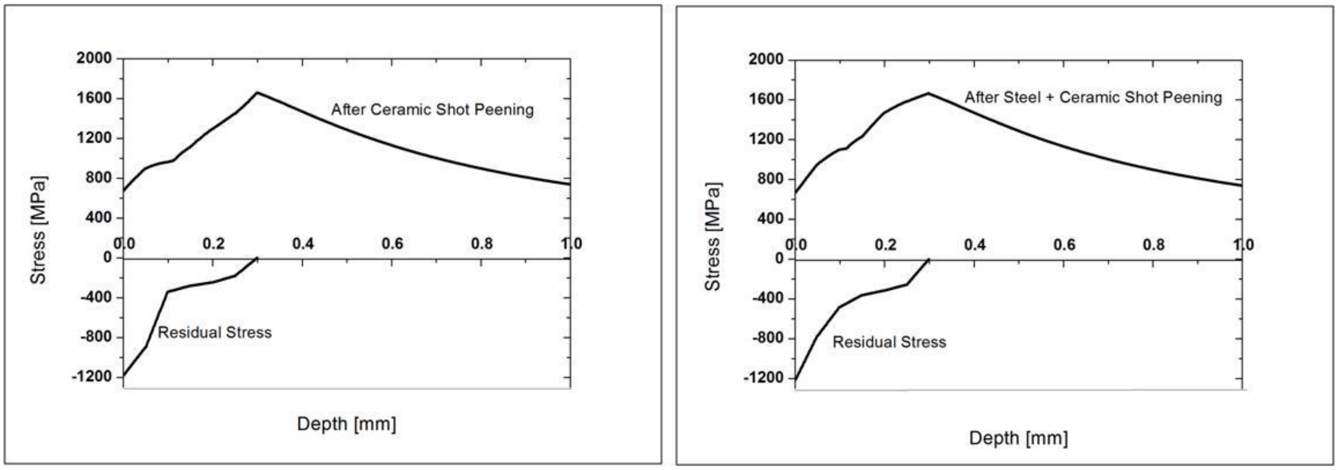

Figure 4.2.23. Stress at 1 GPa mean pressure and residual stresses after ceramic and steel+ceramic shot peening

The combination of the maximum stress profile modified by the increased elastic modulus and the fraction of load bearing section with the residual stress profiles result in a “real stress” profile reported in Figure 4.2.24 for a mean pressure of 1 GPa..

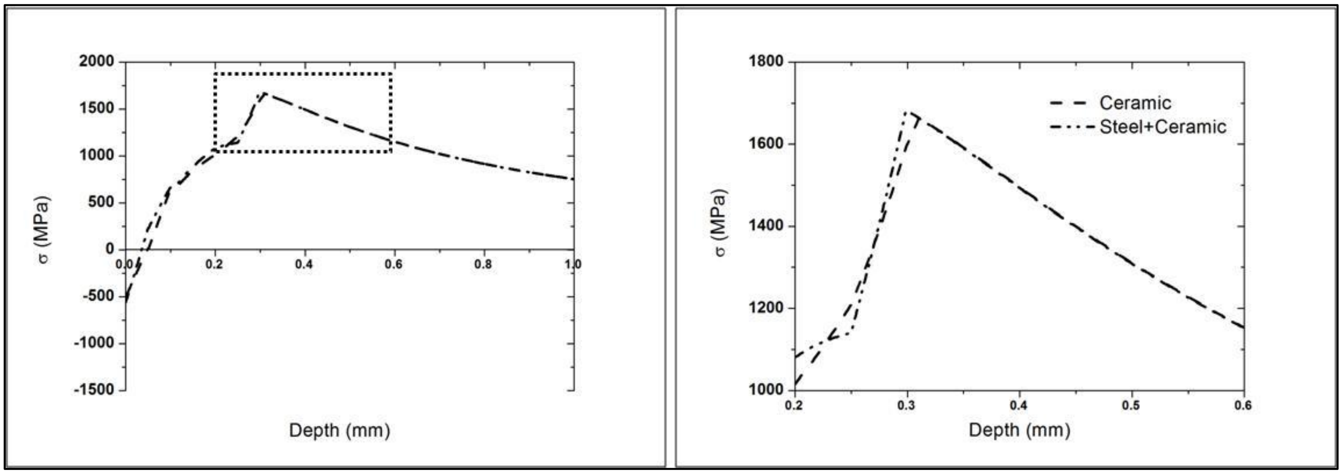

Figure 4.2.24. Stress of ceramic shot peened and steel+ceramic shot peened 73-DDH2-HD at 1 GPa mean pressure.

It can be seen from Figure 4.2.24 that the maximum stress is lowered in both shot peened discs. The difference between ceramic and the steel+ceramic shot peening is almost negligible. From these results, it has been decided to go on with ceramic shot peening, due to the lower deformation of the surface profile previously described. In the following section the effect of ceramic shot peening and its improvements on 73-DDH2-HD, 73-DAE2-HD and 73-AS4300C75 will be discussed.

4.2.3.2 Effect of shot peening on properties of materials

Figure 4.2.25 shows the microstructures of the materials before and after shot peening.

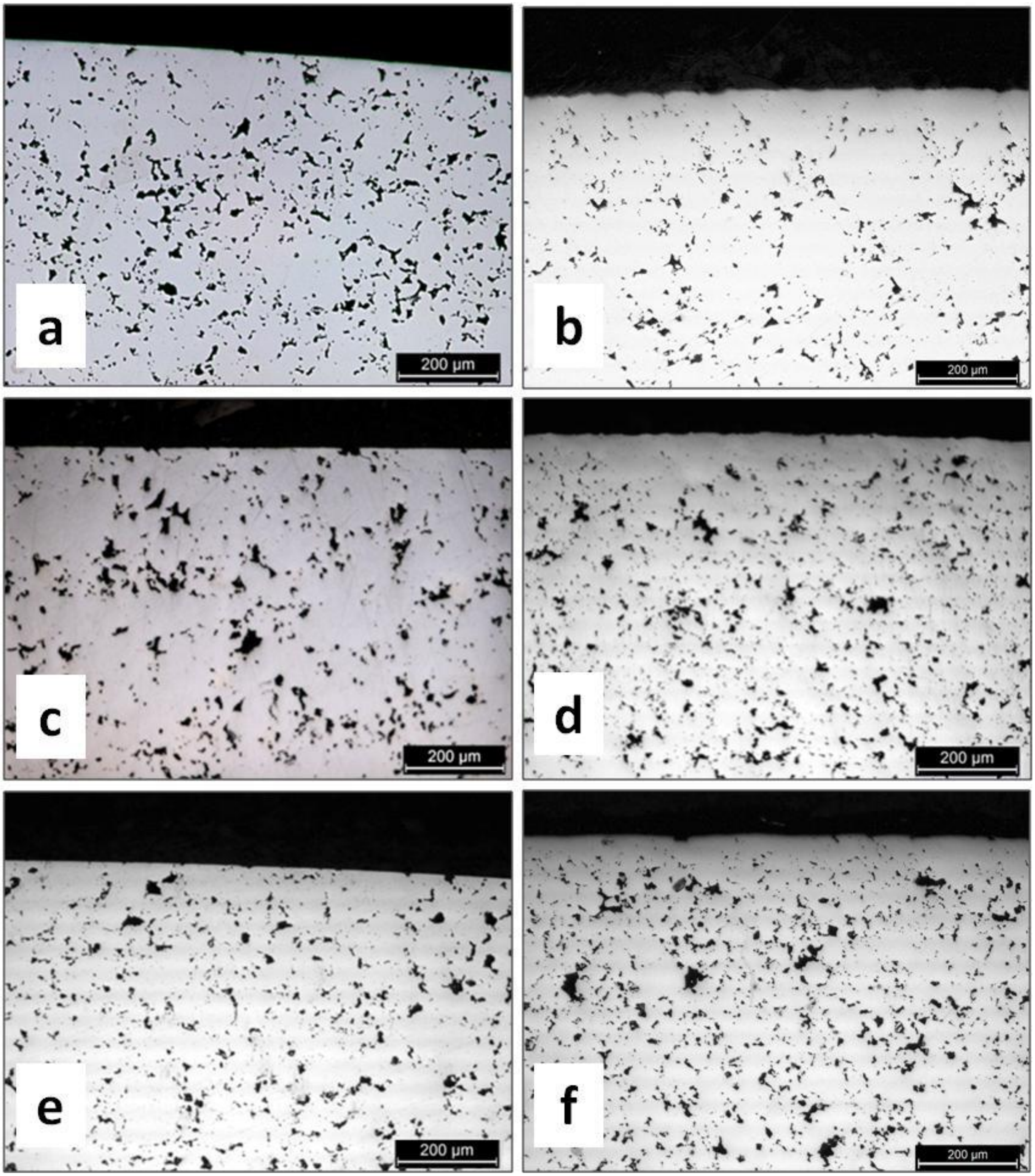

Figure 4.2.25. Microstructures of a) 73-DDH2-HD as sintered, b) 73-DDH2-HD after shot peening, c) 73-DAE2-HD as sintered, d) 73-DAE2-HD after shot peening e) 73-AS4300C75 as sintered f) 73-AS4300C75 after shot peening

Figure 4.2.26 shows the porosity profiles, measured by image analysis. .

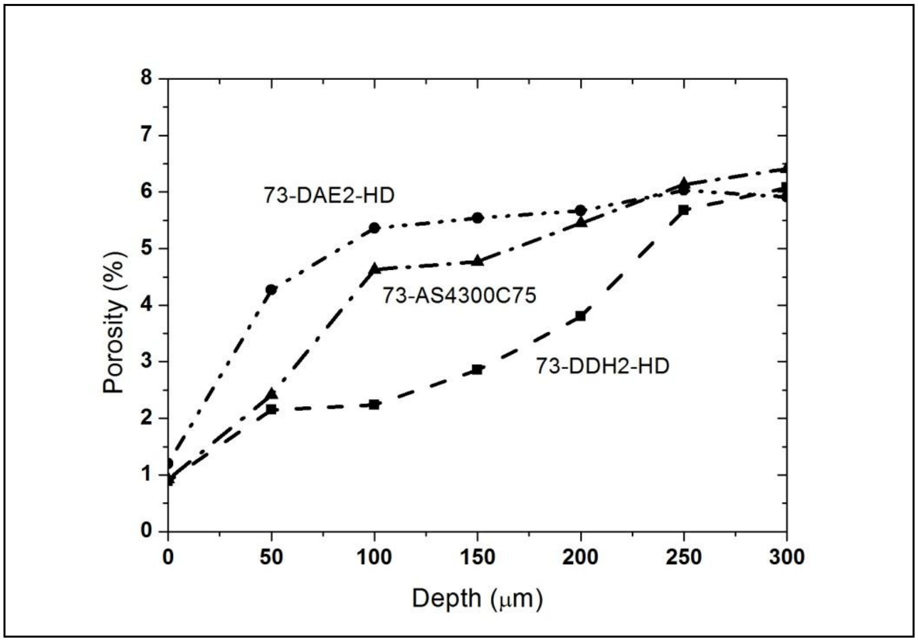

Figure 4.2.26. Porosity profile of 73-DDH2-HD, 73-DAE2-HD and 73-AS4300C75 after ceramic shot peening

The zones affected by shot peening have lower porosity than the core porosity, especially in the first 50 µm. Beyond that depth, only 73-DDH2-HD keeps lower porosity, while 73-DAE2-HD and 73-AS4300C75 tend to get closer to the porosity of the core.

Densities of the zones from 0 to 300 µm were calculated and reported on the Table 4.2.10.

Depth [µm]	**73-DDH2-HD**		**73-DAE2-HD**		**73-AS4300C75**	
	Porosity [%]	**Calculated density [g/cm3]**	**Porosity [%]**	**Calculated density [g/cm3]**	**Porosity [%]**	**Calculated density [g/cm3]**
0-50 µm	0.89	7.72	1.2	7.74	0.92	7.53
50-100 µm	2.15	7.62	4.27	7.50	2.41	7.42
100-150 µm	2.24	7.62	5.36	7.41	4.63	7.25
150-200 µm	2.85	7.57	5.54	7.40	4.77	7.24
200-250 µm	3.80	7.49	5.67	7.39	5.45	7.19
250-300 µm	5.68	7.35	6.03	7.36	5.63	7.17

Table 4.2.10. Calculated densities of 73-DDH2-HD, 73-DAE2-HD and 73-AS4300C75

In addition to optical microscopic images, scanning electron microscope analysis was also performed to check the surface of the materials before and after ceramic shot peening and the results are represented in figure 4.2.27. It can be seen from this analysis that shot peening affects the porosity on the surface of the materials by closing the pores.

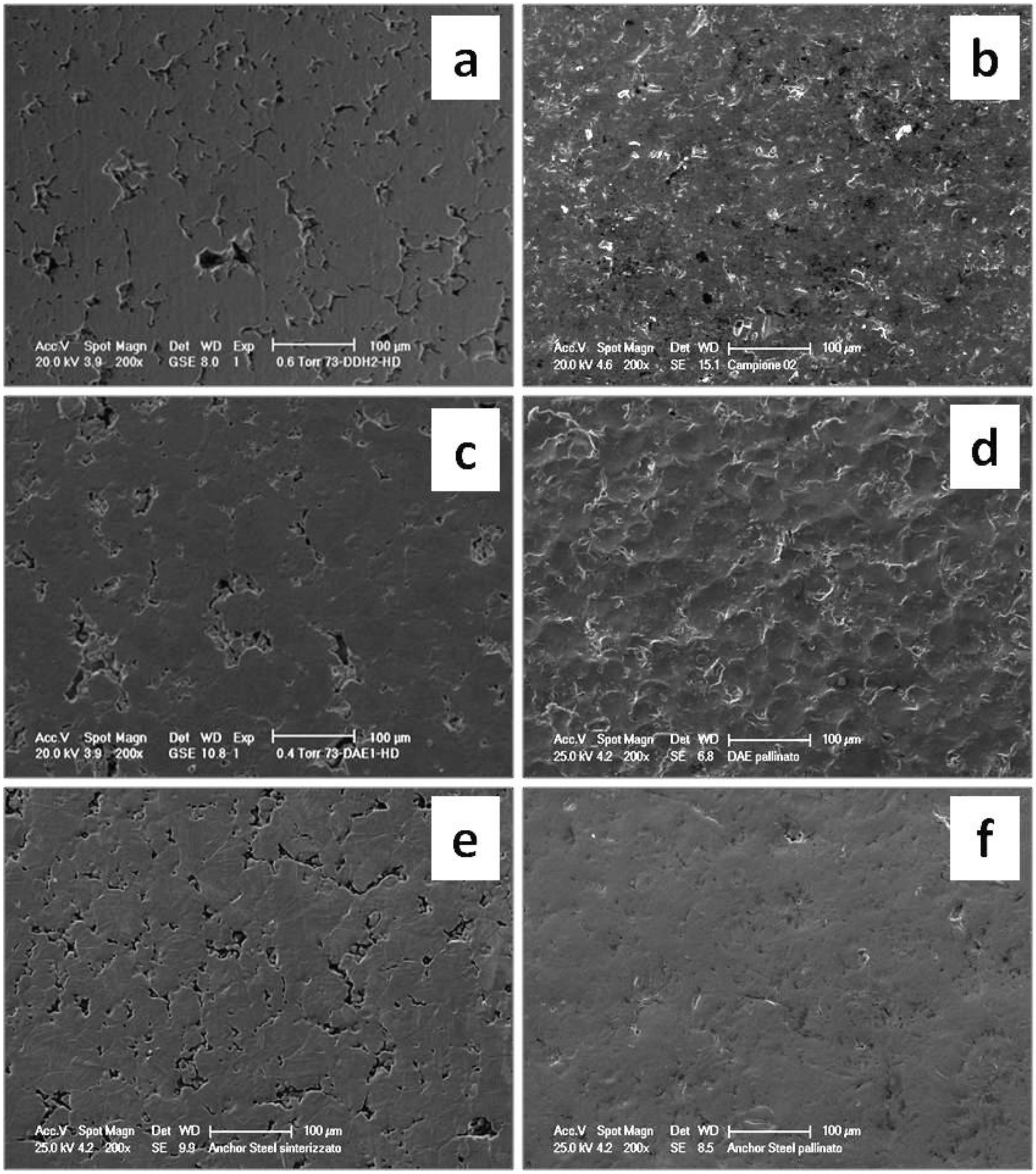

Figure 4.2.27. Surface of a) 73-DDH2-HD as sintered, b) 73-DDH2-HD after shot peening, c) 73-DAE2-HD as sintered, d) 73-DAE2-HD after shot peening e) 73-AS4300C75 as sintered f) 73-AS4300C75 after shot peening

To obtain maximum local stress on the materials, the load bearing section had to be calculated first, according to the equation (24). Since the load bearing section depends on the porosity and the f_{circle} according to equation (25), the change in these two parameters due to the shot peening has been considered in calculation.

For the calculation of f_{circle}, the results from image analysis were utilized. In Figure 4.2.28 left, equivalent diameter versus f_{circle} for all three materials were shown; large pores are also highlighted. In Figure 4.2.28 right mean D_{eq} and mean f_{circle} calculated for the different layer are shown.

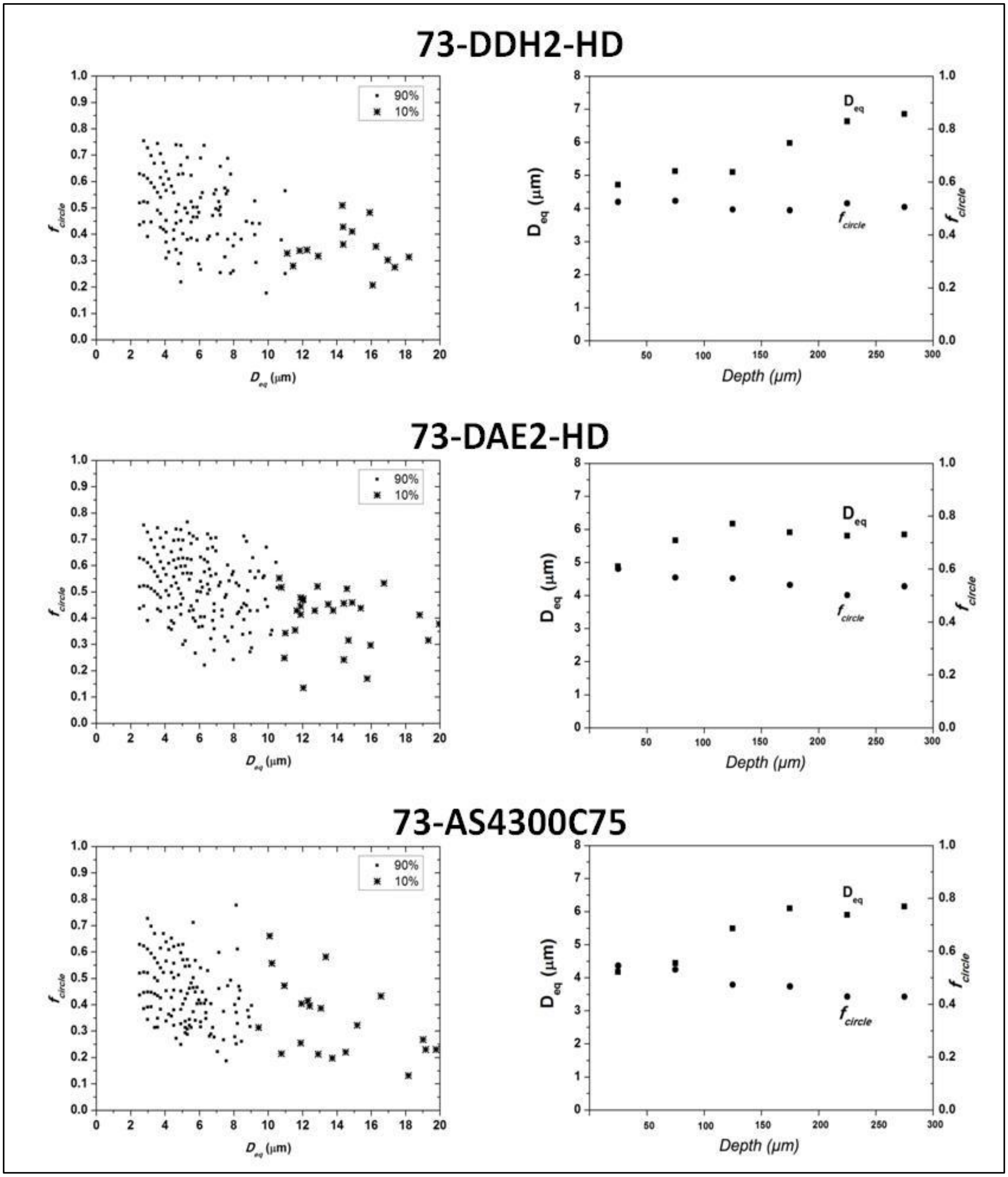

Figure 4.2.28. D_{eq} vs f_{circle} 73-DDH2-HD, 73-DAE2-HD and 73-AS4300C75 and mean D_{eq} and mean f_{circle} values are shown.

The larger and more irregular pores have lower f_{circle} which are the preferred crack sites. It can also be noticed that this change in pore morphology is also depending on the depth from the surface since mean D_{eq} values are increasing.

The fraction of load bearing section was calculated and reported in Table 4.2.11 and the profile was drawn in Figure 4.2.29.

Depth [µm]	**Fraction of load bearing section**		
	73-DDH2-HD	**73-DAE2-HD**	**73-AS4300C75**
0	0.937	0.917	0.952
50	0.847	0.74	0.853
100	0.846	0.701	0.703
150	0.806	0.629	0.684
200	0.716	0.624	0.628
250	0.624	0.617	0.63
300	0.52	0.62	0.53

Table 4.2.11. The fraction of load bearing section of 73-DDH2-HD, 73-DAE2-HD and 73-AS4300C75

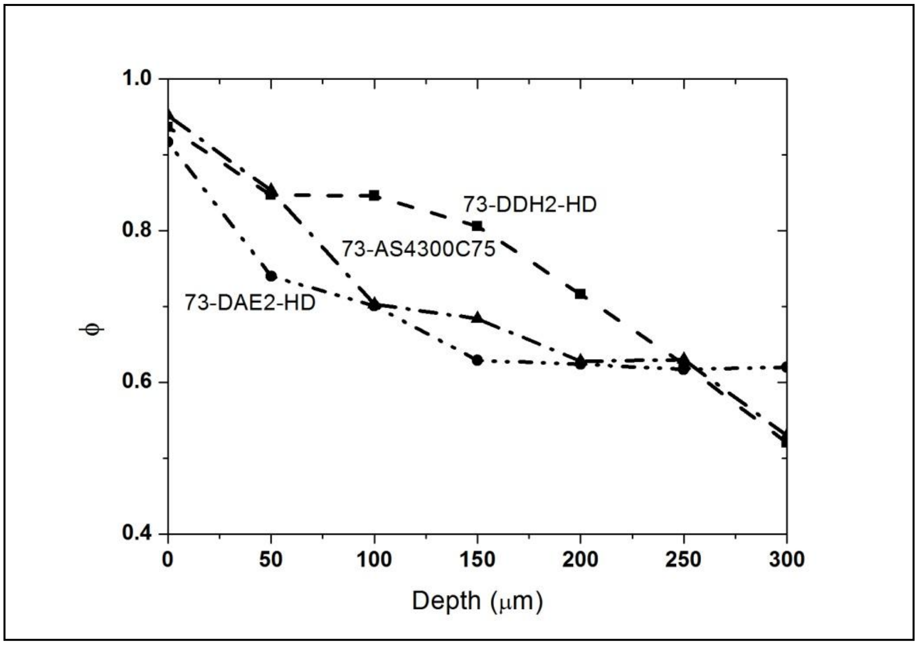

Figure 4.2.29. The fraction of load bearing section profile of 73-DDH2-HD, 73-DAE2-HD and 73-AS4300C75

It can be seen that, close to the surface of the material, the fraction of load bearing section is higher due to the densified region, where the porosity is lower, the pores are smaller and more regularly shaped.

In Figure 4.2.30 on the left, the change in elastic modulus by density is shown based on properties of materials [14]. From this relation, the elastic modulus of the material is extrapolated and the values correspond to the different zones are shown in Figure 4.3.17 on the right for 73-DDH2-HD, 73-DAE2-HD and 73-AS4300C75 .

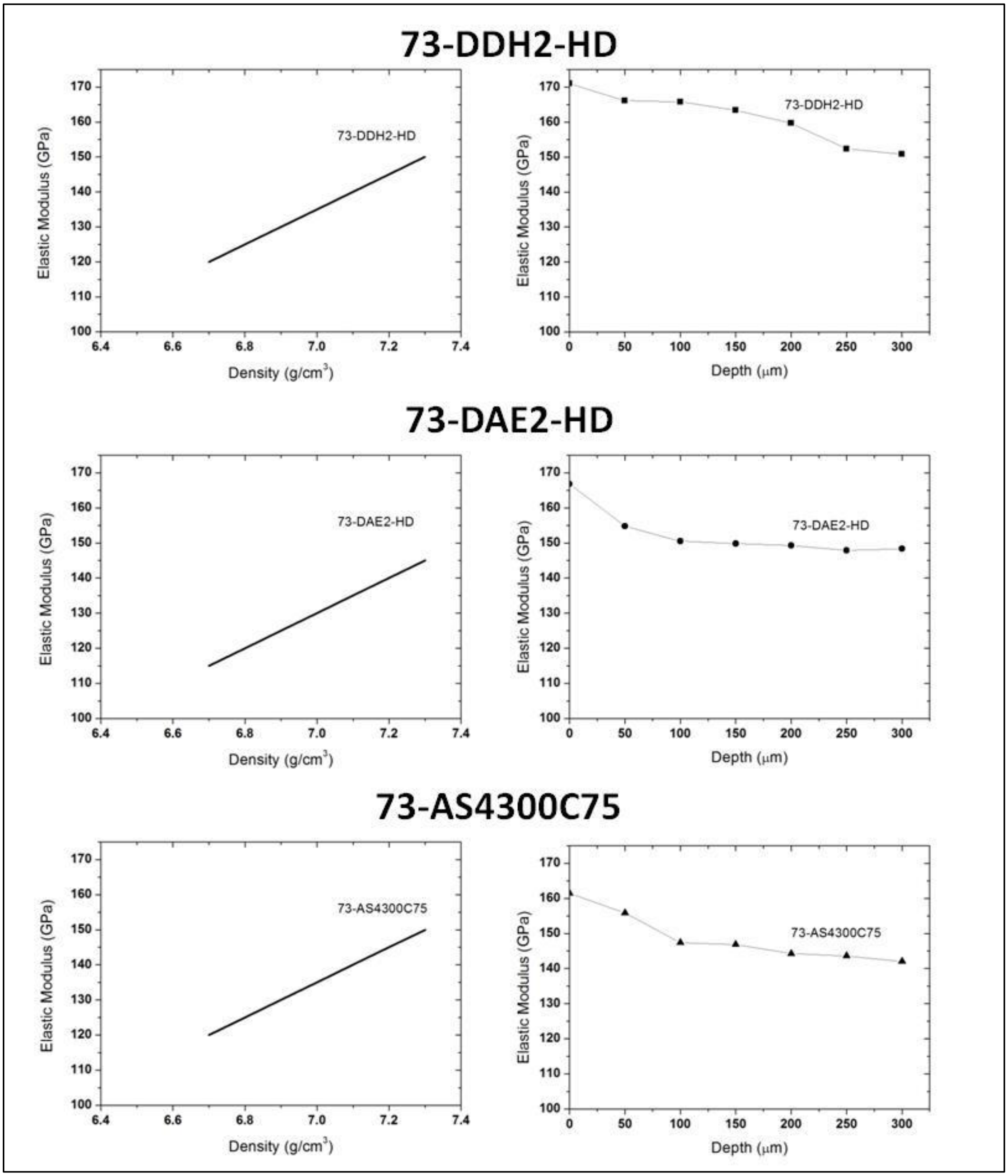

Figure 4.2.30. Elastic modulus of 73-DDH2-HD, 73-DAE2-HD and 73-AS4300C75

The microstructure of the materials after ceramic shot peening is shown in Figure 16.

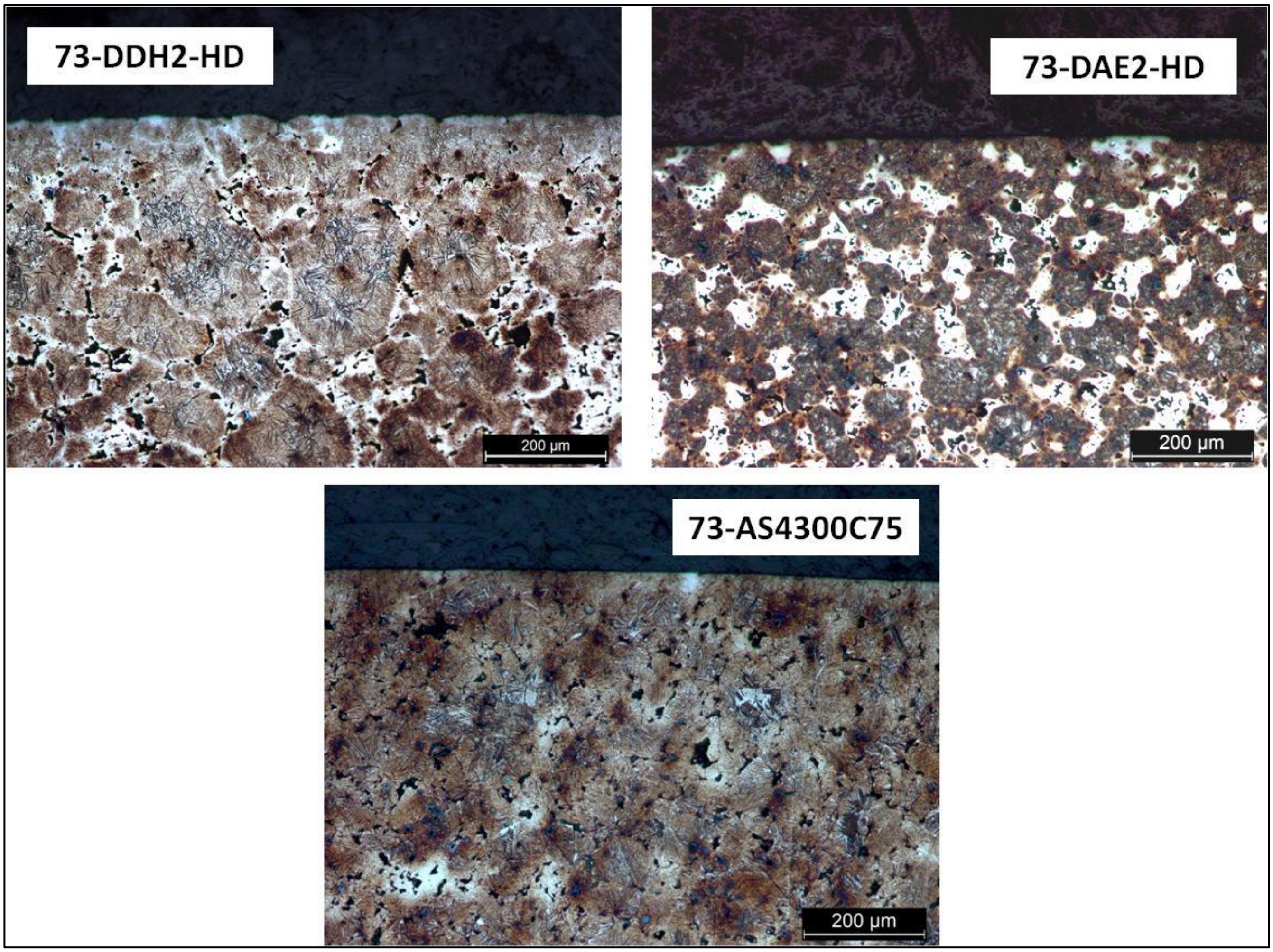

Figure 4.2.31. Microstructure of 73-DDH2-HD, 73-DAE2-HD and 73-AS4300C75 after etching.

After shot peening microhardness was measured again to see possible changes. Figure 4.2.32 shows the slight increase in the microhardness of the materials before and after shot peening.

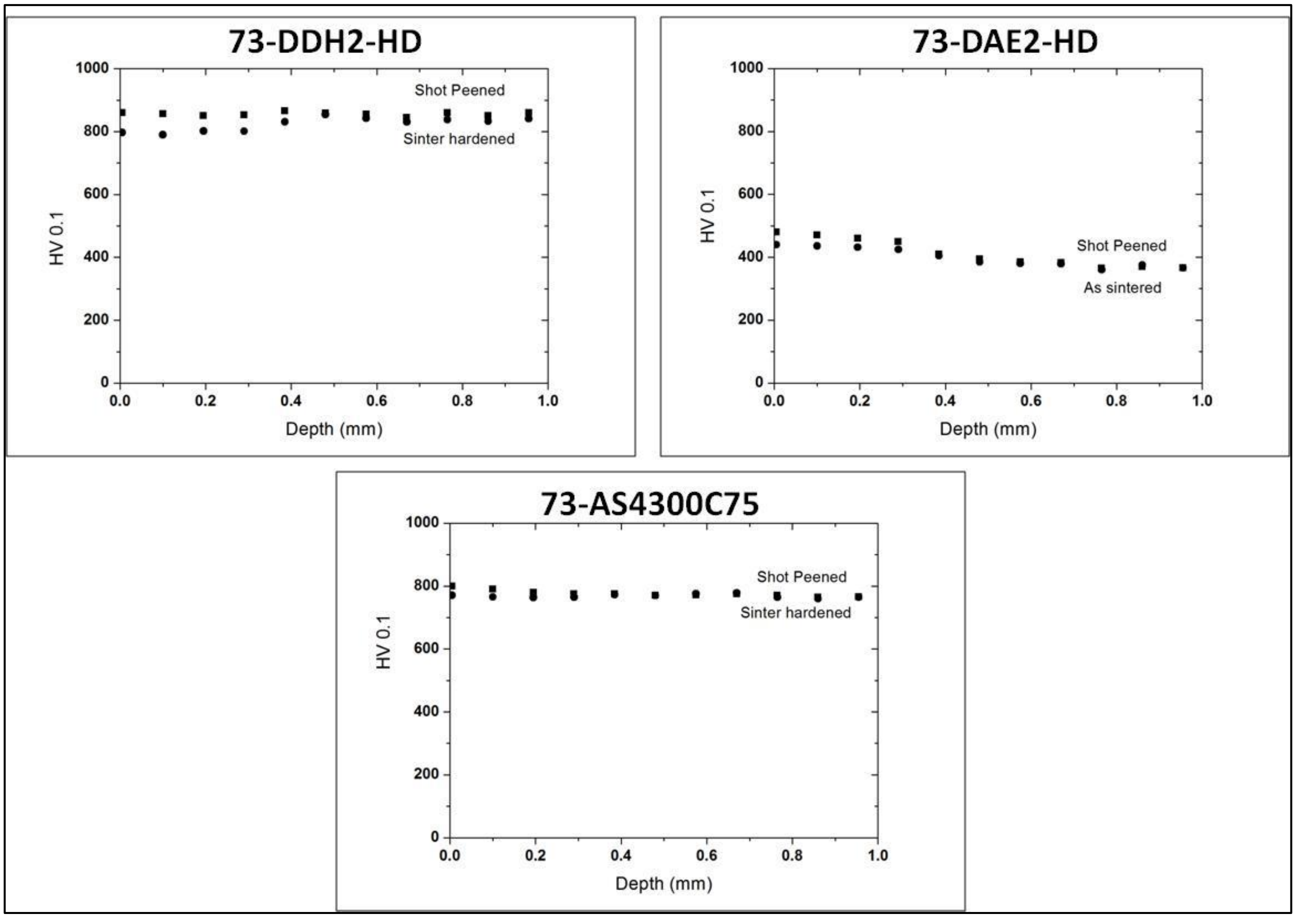

Figure 4.2.32. Microhardness comparison of the materials before and after shot peening.

It should be noted that the comparison of the microhardness before and after shot peening was based on the constituents. For 73-DDH2-HD it refers to the martensite, for 73-DAE2-HD to the Ni-rich austenite and for 73-AS4300C75 to the mean microhardness, as it was decided in CF behavior section.

4.2.3.3 Effect of shot peening on CF behavior

New rolling sliding tests were done on shot peened discs of 73-DDH2-HD, 73-DAE2-HD and 73-AS4300C75. The mean pressures were applied to the materials by considering the results on the as sintered materials.

Firstly, CF test at 1.1 GPa mean pressure was done on shot peened 73-DDH2-HD. At this pressure the as sintered material fast failed. Figure 4.2.33 shows the theoretical calculations and the microstructure of the material after the validation test.

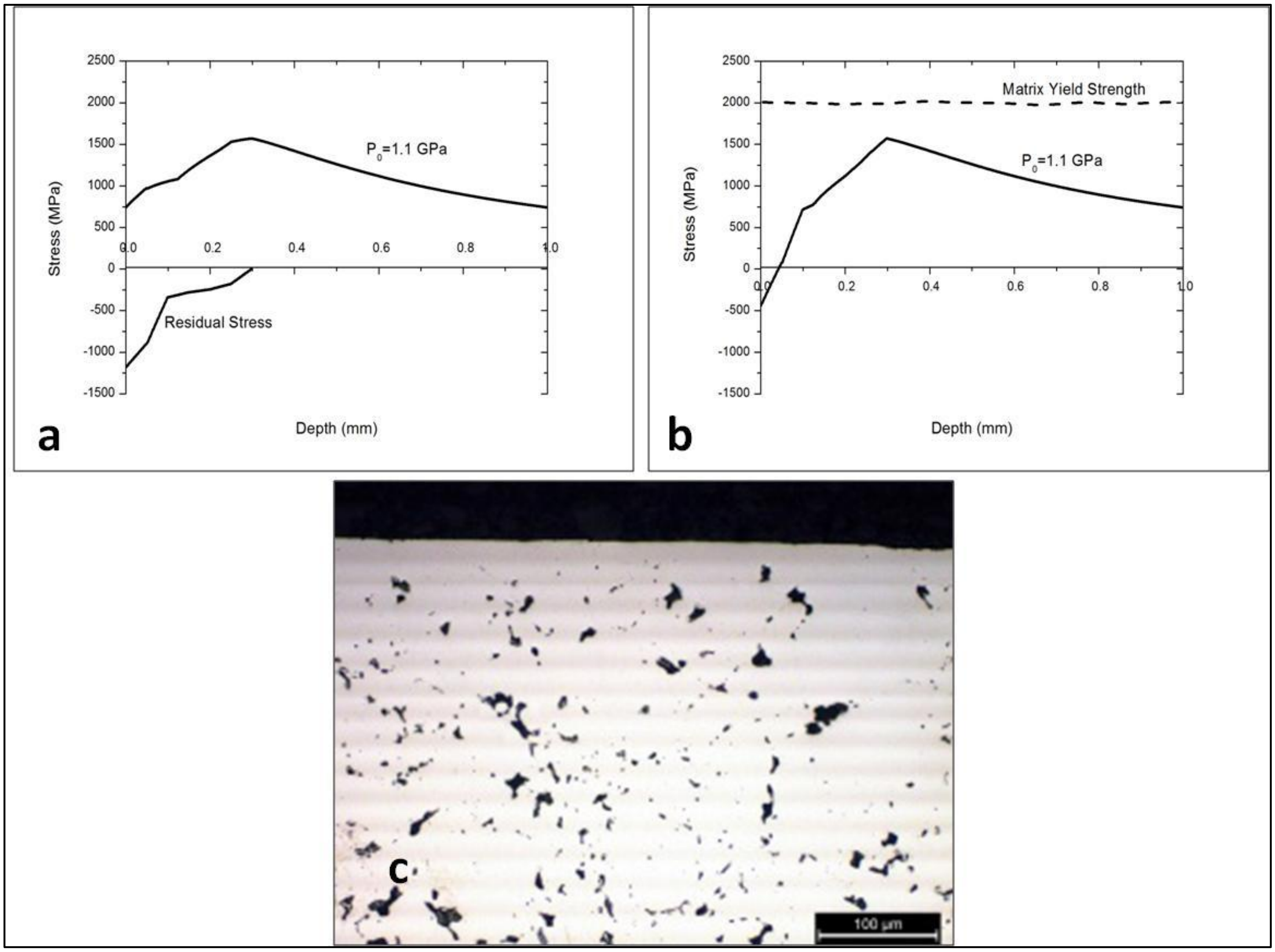

Figure 4.2.33. 73-DDH2-HD a) Stress at 1.1 GPa mean pressure and residual stresses after shot peening, b) Stress at 1.1 GPa mean pressure by introducing residual stresses c) microstructure after the test

Shot peening increases the performance of 73-DDH2-HD: neither theoretical prediction of contact fatigue crack, nor crack observation after the validation test. Mean pressure was increased step by step to 1.15, 1.25 and 1.4 GPa and calculations are shown in Figure 4.2.34, along with the microstructure of the material after the corresponding tests.

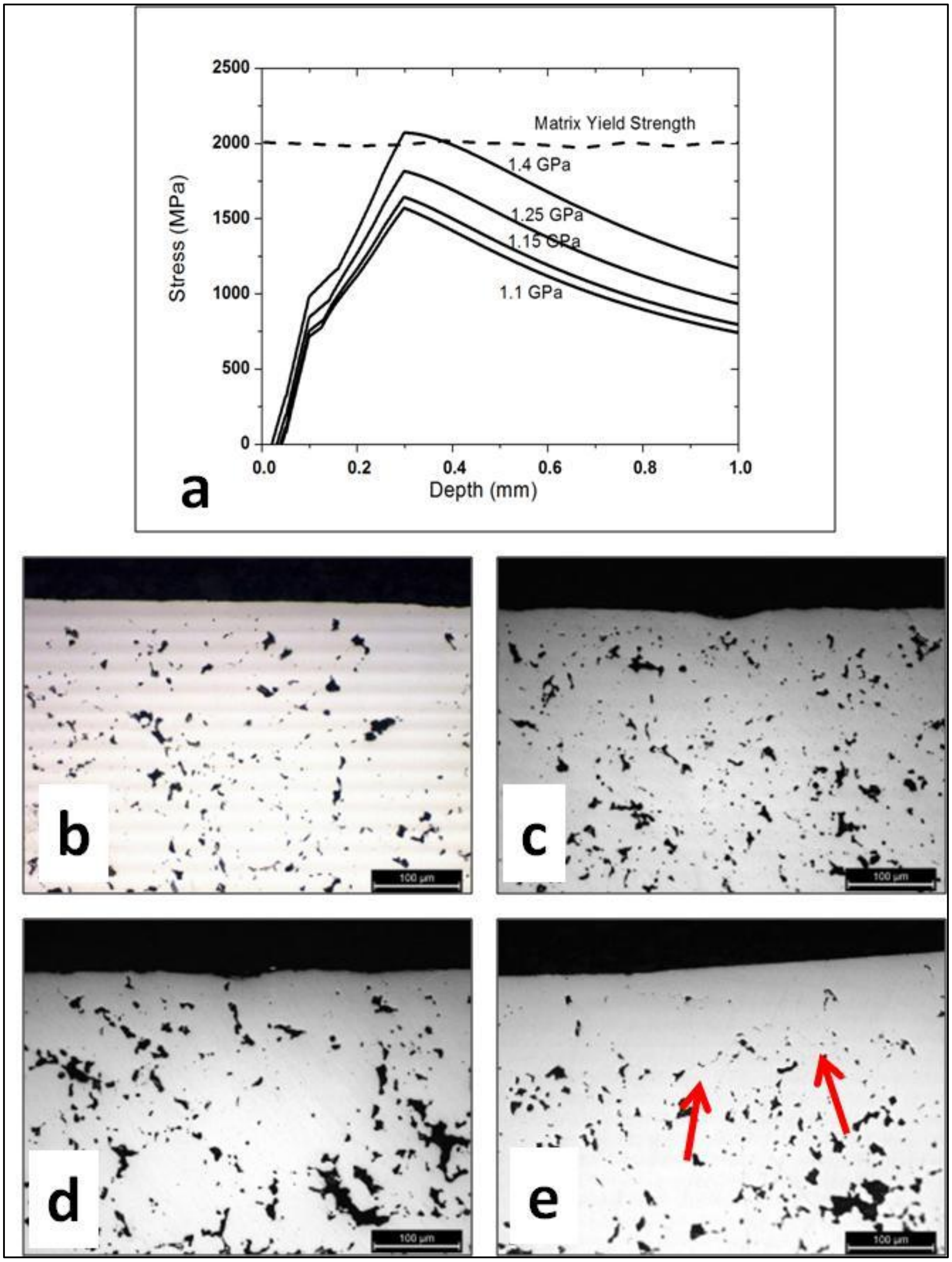

Figure 4.2.34 a) Theoretical calculations for different mean pressures for 73-DDH2-HD, Microstructures after the tests at b) 1.1 GPa, c) 1.15 GPa, d) 1.25 GPa, e) 1.4 GPa

As it can be seen in Figure 4.2.34 a, the CF limit of 73-DDH2-HD was increased significantly after shot peening, since crack nucleation occurs when 1.4 GPa mean pressure was applied. The resistance of the material was then calculated at 1.34 GPa.

For 73-DAE2-HD, cracks were observed at 0.6 GPa mean pressure on as sintered discs. Figure 4.2.35 shows the theoretical calculations at 0.6 GPa along with the experimental result for 73-DAE2-HD after the tests.

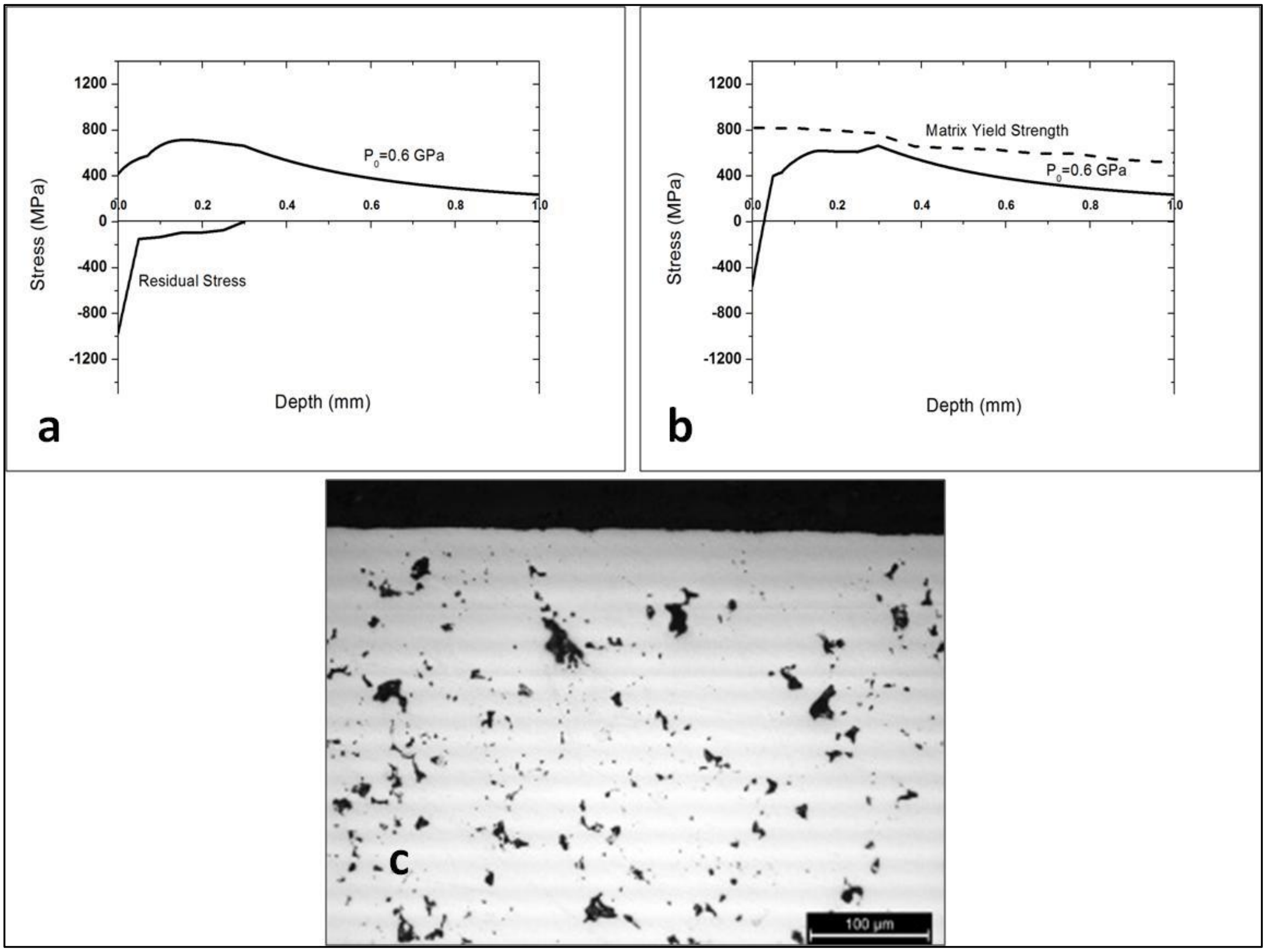

Figure 4.2.35. 73-DAE2-HD a) Stress at 0.6 GPa mean pressure and residual stresses after shot peening, b) Stress at 0.6 GPa mean pressure by introducing residual stresses c) microstructure after the test

Shot peening increases the performance of 73-DAE2-HD: theoretical predictions were not expecting crack nucleation and validation tests confirmed this result. Mean pressure was increased up to 0.8 GPa and calculations were shown in Figure 4.2.36.

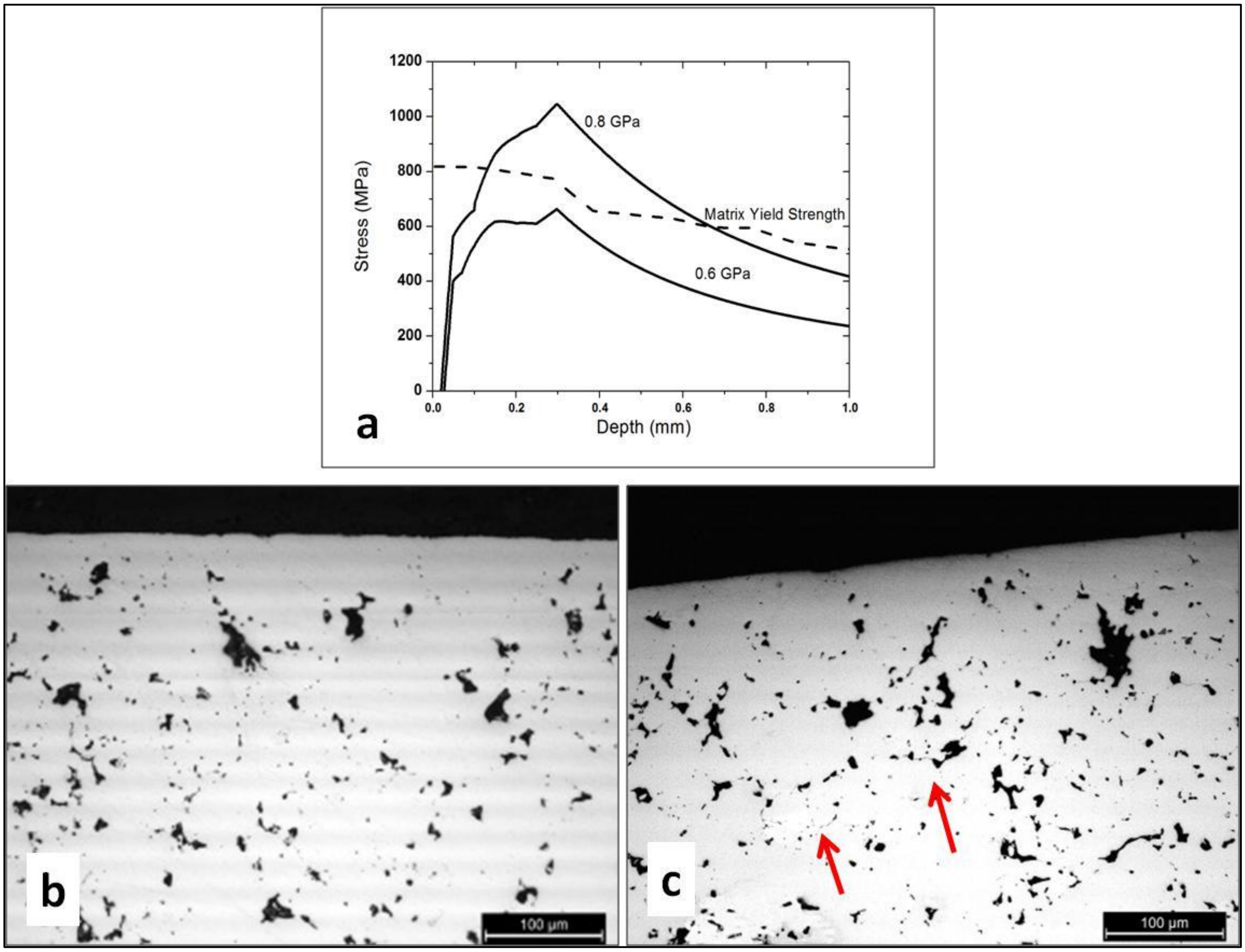

Figure 4.2.36. a) Theoretical calculations for different mean pressures for 73-DAE2-HD, Microstructures after the tests at b) 0.6 GPa, c) 0.8 GPa

The CF resistance of 73-DAE2-HD was increased after shot peening. However this increase is not as high as in 73-DDH2-HD. According to the tests, crack nucleation starts when 0.8 GPa mean pressure was applied. A theoretical resistance of 0.63 GPa was calculated.

For 73-AS4300C75, cracks were observed at 1 GPa mean pressure on as sintered discs. Figure 4.2.37 shows the theoretical calculations at 1 GPa along with the experimental result for 73-AS4300C75 after the tests.

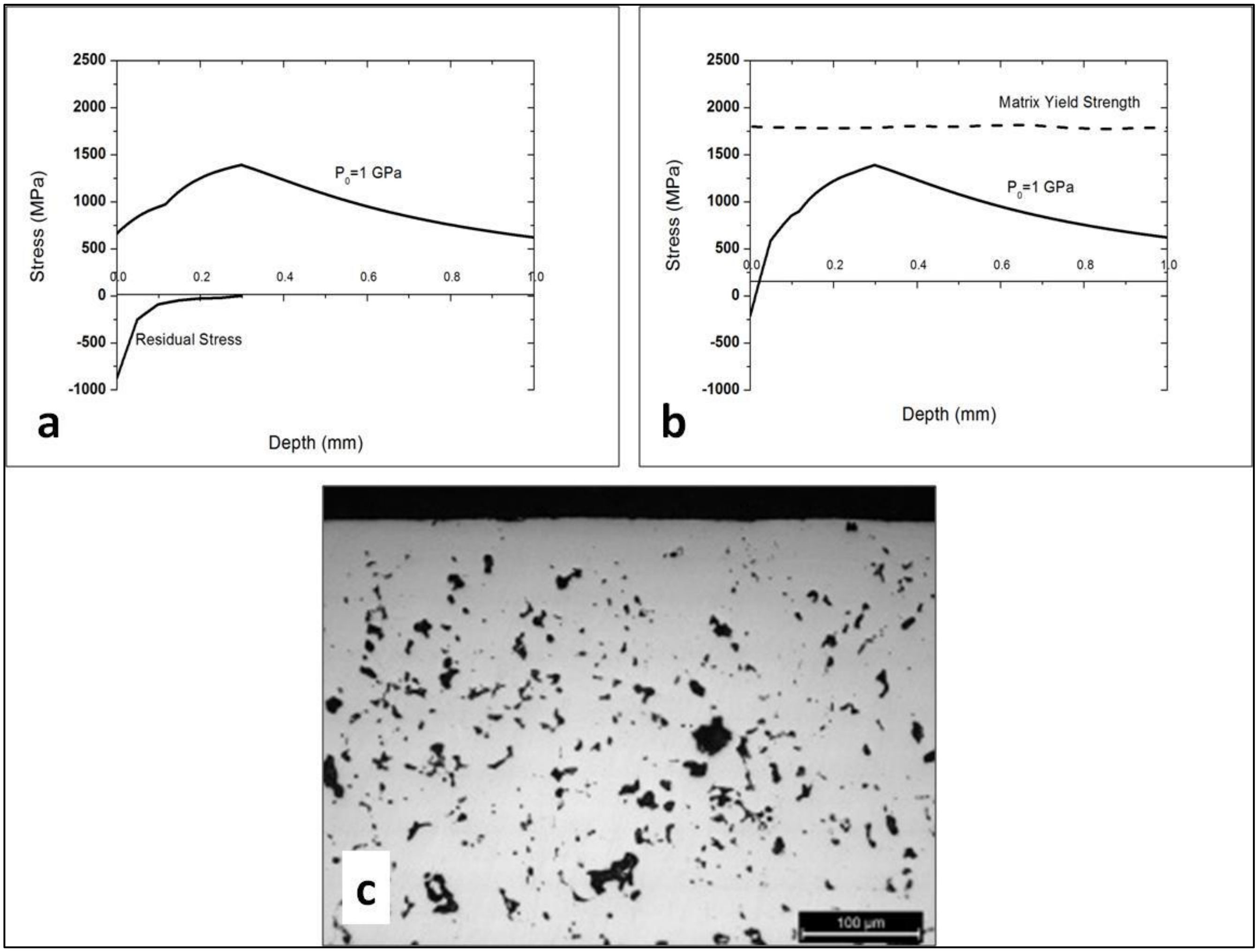

Figure 4.2.37. 73-AS4300C75 a) Stress at 1 GPa mean pressure and residual stresses after shot peening, b) Stress at 1 GPa mean pressure by introducing residual stresses c) microstructure after the test

Shot peening increases the performance of 73-AS4300C75 at 1 GPa: no cracks were predicted and actually observed after the validation test.

The mean pressure was increased step by step to 1.1, 1.15, 1.25 and 1.4 GPa and calculations are shown in Figure 4.2.38, along with the microstructure of the materials after the validation tests.

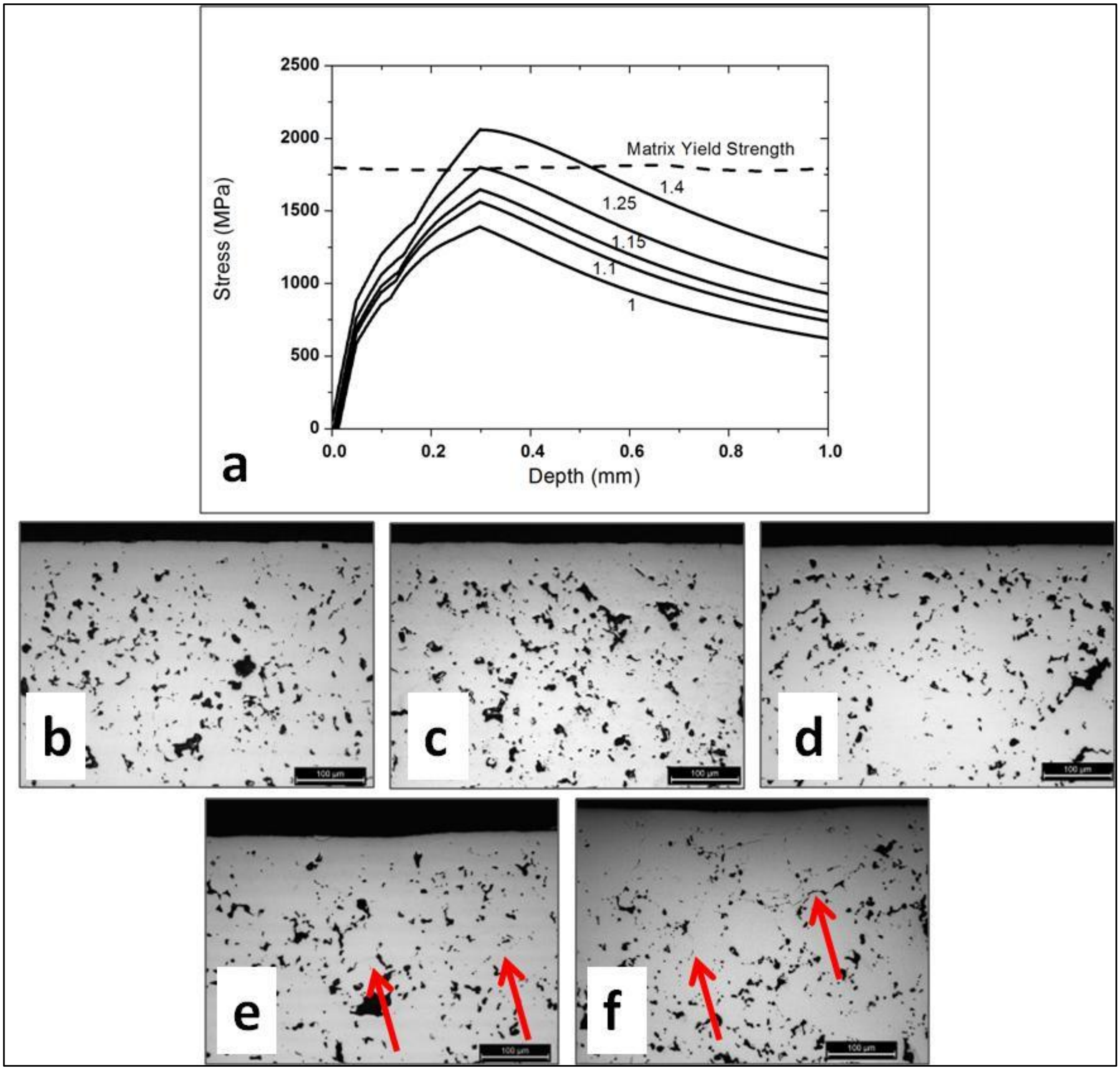

Figure 4.2.38. a) Theoretical calculations for different mean pressures for 73-AS4300C75, Microstructures after the tests at b) 1 GPa c) 1.1 GPa, d) 1.15 GPa, e) 1.25 GPa, f) 1.4 GPa

As the other two materials, the CF resistance of 73-AS4300C75 was also increased after shot peening. According to the tests, crack nucleation started when 1.25 GPa mean pressure was applied. Table 4.2.12 summarizes the theoretical predictions and experiments validations after all tests on shot peened materials. "No" represents that no cracks were expected in theoretical prediction and no cracks were observed in experimental results. On the other hand, "Yes" represents the prediction of possible cracks by theory and the actual observation of cracks in experimental results.

Material Name	**Mean Pressure (GPa)**													
	0.6		**0.8**		**1.0**		**1.1**		**1.15**		**1.25**		**1.4**	
	Theoretical Prediction	**Experimental Result**	**Theoretical Prediction**	**Experimental Result**	**Theoretical Prediction**	**Experimental Result**	**Theoretical Prediction**	**Experimental Result**	**Theoretical Prediction**	**Experimental Result**	**Theoretical Prediction**	**Experimental Result**	**Theoretical Prediction**	**Experimental Result**
73-DDH2-HD	--	--	--	--	No Cracks	No Cracks	No Cracks	No Cracks	No Cracks	No Cracks	No Cracks	No Cracks	Cracks	Cracks
73-DAE2-HD	No Cracks	No Cracks	Cracks	Cracks	--	--	--	--	--	--	--	--	--	--
73-AS4300C75	--	--	--	--	No Cracks	No Cracks	No Cracks	No Cracks	No Cracks	No Cracks	Cracks	Cracks	Cracks	Cracks

Table 4.2.12. Summary of theoretical predictions and experimental validations after rolling sliding tests

Theoretical resistance for each material in as sintered condition and after shot peening is listed in Table 4.2.13.

Material	**As sintered CF resistance Mean pressure (GPa)**	**Shot peened CF resistance Mean pressure (GPa)**	**Improvement (%)**
73-DDH2-HD	1.07	1.34	25
73-DAE2-HD	0.53	0.63	19
73-AS4300C75	0.97	1.22	26

Table 4.2.13. The maximum limit of mean pressure for 73-DDH2-HD, 73-DAE2-HD and 73-AS4300C75 after shot peening

As it is shown in Table 4.2.13, shot peening improved the CF performances of 73-DDH2-HD, 73-DAE2-HD and 73-AS4300C75 by 25%, 19% and 26% respectively.

4.2.4 Summary

In the first part of the work, a conservative approach to predict the contact fatigue behavior of three different sintered and heat treated steels, 73-DDH2-HD, 73-DAE2-HD and 73-AS4300C75, was proposed. It was based on the nucleation of the fatigue crack, rather than on its possible propagation within the expected lifetime of the parts. The nucleation of the fatigue crack is anticipated by the local plastic deformation of the material, which occurs when the maximum local stress exceeds the yield strength of the matrix. In absence of local plastic deformation no cracks will nucleate. The model was validated with experimental tests.

The heterogeneous microstructure of the materials studied has to be considered developing a model to predict fatigue crack nucleation, the success of which will depend from a local approach. Considering that fatigue cracks most often nucleate in correspondence of the largest, more irregular pores, it is necessary to evaluate the characteristics of the largest pores, and the microhardness of the microstructural constituents where they are localized. The local plastic deformation, indeed, occurs in correspondence of the large and irregular pores, depending on the local mechanical resistance of the material. Using the mean porosity characteristics and the mean microhardness to calculate the maximum local stress and the yield strength of the matrix will lead to failing predictions.

The model may be applied to predict the effect of any microstructural modification introduced by compaction and sintering, as well as any modification provided by chemical composition and secondary operations suitable to increase the mechanical resistance of the PM steels.

On the basis of the results concerning contact fatigue behavior of the investigated steels, 73-DDH2-HD, 73-DAE2-HD and 73-AS4300C75, shot peening was proposed to improve the contact fatigue resistance.

At first, two different shot peening methods, ceramic and steel+ceramic, were considered. 73-DDH2-HD was used to choose the shot peening type, since it was the best performing material in CF tests on the as sintered materials. Ceramic shot peening was done with ceramic shots in one step while steel+ceramic shot peening was done by using steel shots first and ceramic shots in the second step. The effect of both shot peening methods was investigated by considering the introduced residual stresses and the densification on the surface of the materials, which resulted in the change in porosity, fraction of load bearing section and the elastic modulus of the material. After all calculations, it was discovered that both ceramic and steel+ceramic shot peening methods affected the CF behavior similarly. Therefore, considering that steel+ceramic shot peening determined a worsening in surface finishing, ceramic shot peening was chosen.

Ceramic shot peening was applied on all investigated materials, 73-DDH2-HD, 73-DAE2-HD, and 73-AS4300C75. All materials were again investigated after ceramic shot peening and the change in porosity, elastic modulus and the fraction of load bearing section was recalculated in the compressive residual stress affected zone. After those calculations, the model was applied to estimate the maximum mean pressure, at which the shot peened material is expected to survive, and the theoretical prediction has been confirmed experimentally. Shot peening increased the contact fatigue resistance of 73-DDH2-HD, 73-DAE2-HD, and 73-AS4300C75 by 25%, 19%, and 26% respectively.

5. Conclusions

In this work, the dry sliding and contact fatigue behavior of different high density Ni-Cu-Mo PM steels, either sinterhardened or heat treated, has been investigated.

In the first part, the study of dry sliding behavior was made by carrying out dry sliding tests at different pressures and different speeds. that the results may be summarized as follows;

- All investigated materials show a better wear resistance at lower speed and lower mean pressures.
- At lower speeds and mean pressures a protective oxide layer which reduces the wear rate forms, giving rise to a low velocity triboxidative wear mechanism; in the other conditions, typical adhesive wear is observed
- The presence of nickel (Ni) in the material reduces the dry sliding wear resistance of the materials due to the soft Ni-rich austenite.
- The effect of Ni is directly correlated to its amount; the increase in Ni amount decreases dry sliding resistance.
- The Ni-rich austenite has a lower resistance to plastic deformation than the bainitic/martensitic matrix; this leads to localized plastic deformation which reduces the mechanical stability of the surface increasing wear rate even in case of a triboxidative wear mechanism.

Design guideline was proposed for all investigated materials by considering the wear thickness as the basis of the calculations. Wear thicknesses of all materials were calculated from the wear rate after one million of cycles and compared to the dimensional tolerance of the part diameter defined by ISO Standards, as a failure criterion. The results lead to the following conclusions:

- In most of the cases the wear thickness of the materials was higher than failure criterion, especially at higher speeds.
- When materials did not meet the failure criterion, two different approaches were considered to reduce wear thickness and, in turn, the working life of the components: increase in the contact length and increase in the hardness of the materials,
- With these two approaches, some improvement was observed in the working life of the components.

- Calculations showed that increasing contact length was more effective approach than increasing hardness of the materials.

In the second part of the study, the contact fatigue behavior of three different PM steels was investigated. A theoretical model was developed to predict the nucleation of the contact fatigue crack, by considering the peculiar characteristics of PM materials: porosity and the microstructural heterogeneity. Theoretical calculations were done on the basis of the model and validated by experimental methods. Considering that the fatigue crack nucleation is anticipated by plastic deformation, and that plastic deformation occurs when the maximum local stress exceeds the yield strength of the matrix, the main results of the study may be summarized as follows.

- If the fraction of the load bearing section is calculated considering the whole of the pore population, the theoretical model does not predict crack nucleation properly; this is due to the observation that the crack nucleates in correspondence of the larger pores.
- The fraction of the load bearing section has to be calculated considering the larger pores corresponding to 10% of their population.
- Even in this case, the theoretical model does not work properly if the yield strength of the matrix is calculated from the mean microhardness of the matrix.
- The yield strength of the matrix has to be calculated considering the microhardness of the microstructural constituent where the large pores are localized.
- The presence of Ni reduces the resistance to contact fatigue since anticipated plastic deformation, and the consequent nucleation of the crack, occur in the soft Ni-austenite

After defining the contact fatigue limits of investigated materials, shot peening was proposed to improve their contact fatigue behaviors. Steel+ceramic and ceramic shot peening were considered as two different methods and their effects were compared. Calculations showed that ceramic shot peening was the more suitable one. Shot peening causes surface densification and strain hardening, in addition to the accumulation of compressive residual stresses. Therefore elastic properties, the fraction of the load bearing section and the microhardness are modified by shot peening. The theoretical model has to account for these modifications. Theoretical predictions and experimental tests indicate that shot peening increases the contact fatigue resistance of all investigated materials.

6. References

1. W.O. Winer, MB Peterson (Eds.), "Wear Control Handbook", 1980.

2. R.G. Bayer, Wear Analysis for Engineers, 2002.

3. ASM Handbook, "Friction, Lubrication and Wear Technology", Volume 18, 1992.

4. R.G. Bayer, "Mechanical Wear Prediction and Prevention", 1994.

5. G. Straffelini, "Attrito e Usura, Metodologie di Progettazione e Controllo", 2007.

6. http://www.oerlikon.com/balzers/en/know-how/wear-tribology/, accessed in April 2014.

7. G.W. Stachowiak, A.W. Batchelor, "Engineering Tribology", 2005.

8. G.W. Stachowiak, A.W. Batchelor, G.B. Stachowiak, "Experimental Methods in Tribology", 2004.

9. Khorsand, H., Habibi, S. M., Yoozbashizadea, H., Janghorban, K., Reihani, S. M. S., Rahmani Seraji, H., & Ashtari, M., "The role of heat treatment on wear behavior of powder metallurgy low alloy steels." Materials & design 23.7 (2002): 667-670.

10. Wang, Jun'an, and Herbert Danninger. "Dry sliding wear behavior of molybdenum alloyed sintered steels." Wear 222.1 (1998): 49-56.

11. Tekeli, S., A. Güral, and D. Özyürek. "Dry sliding wear behavior of low carbon dual phase powder metallurgy steels." Materials & design 28.5 (2007): 1685-1688.

12. Matsui, M., and H. Kakishima. "Improvement of tribological performance of steel by solid lubricant shot-peening in dry rolling/sliding contact wear tests." Wear260.6 (2006): 669-673.

13. Ceschini, Lorella, et al. "Friction and wear behaviour of sintered steels submitted to sliding and abrasion tests." Tribology international 39.8 (2006): 748-755.

14. A.I. Taskinen, M.H.Tikkanen, Wear resistance of sintered steels, Modern Development in Powder Metallurgy 17 (1984) 545-567.

15. E.R. Leheup, D. Zhang, J.R. Moon, The effect of density on fretting wear of sintered iron, Wear 176 (1994) 111-119.

16. G. Straffelini, A. Molinari, Effect of hardness on rolling-sliding damage mechanisms in PM steels, Powder Metallurgy 44 (4) (2001) 344-350.

17. B. Dubrujeaud, M. Vardavoulias, M. Jeandin, The role of porosity in the dry sliding wear of a sintered ferrous alloy, Wear 174 (1995) 155-161.

18. G. Straffelini, A. Molinari, Dry sliding wear of ferrous PM materials, Powder Metallurgy 44 (3) (2001) 248-252.

19. A. Molinari, G. Straffelini, P. Campestrini, Influence of microstructure on impact and wear behaviour of sintered Cr and Mo steel, Powder Metallurgy 42 (3) (1999) 235-241.

20. G. Straffelini, T. Marcu Puscas, A. Molinari, Identification of rolling-sliding damage mechanisms in porous alloys, Metallurgical and Materials Transactions A 31 (12) (2000) 3091-3099.

21. Nickel Development Institute Reference Book, Series No 11 006.

22. Davis, Joseph R., ed. Nickel, cobalt, and their alloys. ASM international, 2000.

23. V. Stoyanova, A. Molinari, Vacuum sintering and sinter-hardening of Mo and Ni low alloyed steels, Powder Metallurgy Progress 4 (2) (2004) 79-87.

24. B. Maroli, S. Berg, U. Engstrom and P. Thorme, Sinter-Hardening and heat treatment of materials based on Astaloy CrM, Advances in Powder Metallurgy and Particulate Materials 1 (2003) 45–51.

25. N. Anton, J.L. Delgado, F. Velasco, J.M. Torralba, Influence of alloying element additions on tribological behaviour of sintered steels with high content in manganese–nickel, Journal of Materials Processing Technologies 143-144 (2003) 475-480.

26. P. Vieira Muterlle, G. Straffelini, A. Molinari, W. Pahl, Microstructural effects in wear of hardened sintered steels produced by diffusion bonded and prealloyed powders, Powder Metallurgy 53 (3) (2010) 201-207.

27. G. Pahl, W. Beitz, J. Feldhusen, K.H. Grote, “Engineering Design: A systematic approach”, 3rd ed., 2007, Springer, Berlin.

28. ASM Handbook: materials selection and design, vol. 20, 1997, ASM International.

29. M.M. Farag, “Materials and process selection for engineering design”, 2008, CRC Press, Taylor & Francis Group.

30. I. Cristofolini, A. Molinari, G. Straffelini, A systematic approach to design against wear for Powder Metallurgy (PM) steel parts: The case of dry rolling-sliding wear, Materials and Design 32 (2011) 2191–2198.

31. I. Cristofolini, M. Pilla, A. Molinari: Optimization of PM parts for wear resistance. Design criteria for dry rolling-sliding wear, Advances in Powder Metallurgy & Particulate Materials 9 (2011) 47-56.

32. K.L. Johnson, “Contact Mechanics”, 1985, Cambridge University Press.

33. K. Mao, Y. Sun, and T. Bell, Surface Engineering 10(4) (1994) 297-306.

34. C. Santus, M. Beghini, I. Bartilotta, M. Facchini, International Journal of Fatigue 45 (2012) 71–81.

35. M. Šraml, J. Flašker, I. Potrč, International Journal of Fatigue 25 (7) (2003) 585-595.

36. C.M. Sonsino, K. Lipp, Paper No. 99M-9, SAE International Congress and exhibition, Detroit, Michigan, March 1-4, 1999.

37. K. Lipp, C.M. Sonsino, D. Pohl, Proceedings of Powder Metallurgy World Congress & Exhibition, Granada, Spain, 18-22 October 1998, ed. EPMA Shrewsbury UK, vol. 3, pp. 143-148.

38. C.M. Sonsino, Proceedings of Euro-PM2001, September 12-14 September 2001, Nice, France, ed. EPMA Shrewsbury UK, vol. 3, pp. 80-109.

39. R. Haynes, Powder Metall., 1970, 13, 397, 465, 475.

40. R. Haynes, ‘The mechanical behavior of sintered metals’, 1981.

41. F. J. Esper and C. M. Sonsino, ‘Fatigue design for PM components’; 1994.

42. D.A Gerard, D.A. Koss, “Low Cycle Fatigue Crack Initiation: Modeling the Effect of Porosity,” The International Journal of Powder Metallurgy, 26:4 (1990), 337-343.

43. H. Danninger, D. Spoljaric, B. Weiss, “Microstructural Features Limiting the Performance of P/M Steels,” The International Journal of Powder Metallurgy, 33:4 (1997), 43-53.

44. K.D. Christian, R.M. German, “Relation Between Pore Structure and Fatigue Behavior in Sintered Iron-Copper-Carbon,” The International Journal of Powder Metallurgy, 31:1 (1995), 51-61.

45. U. Lindstedt, B., Karlsson, R. Masini, “Influence of Porosity on Deformation and Fatigue Behavior of P/M Austenitic Stainless Steels,” The International Journal of Powder Metallurgy, 33:8 (1997), 49-61.

46. K.V. Sudhakar, “Fatigue Behavior of a High Density Powder Metallurgy Steel,” International Journal of Fatigue, 22 (2000), 729-734.

47. H. Drar, “Metallographic and Fractographic Examination of Fatigue Loaded PM-Steel With and Without MnS Additive,” Materials Characterization, 45 (2000), 211-220.

48. Bergmark, A. (2001). Influence of Density on P/M Steel Fatigue Crack Initiation and Propagation. Advances in Powder Metallurgy and Particulate Materials, (10), 10-95.

49. B. Karlson, I. Bertilsson "Mechanical Properties of Sintered Steels", Modern Developments in Powder Metallurgy, 11:6 (1982), 267.

50. Andersson, Michael. "The role of porosity in fatigue of PM materials." Powder Metallurgy Progress 11.1-2 (2011): 21-31.

51. Bergmark, Anders. "Influence of maximum pore size on the fatigue performance of PM steel." Powder Metallurgy Progress 5.3 (2005): 131.

52. Kubicki, B. "Stress concentration at pores in sintered materials." Powder metallurgy 38.4 (1995): 295-298.

53. Danninger, H., et al. "Microstructure and mechanical properties of sintered iron. I: Basic considerations and review of literature." PMI. Powder metallurgy international 25.3 (1993): 111-117.

54. Heckel R., "A new approach to the study of powder compaction". Progress in Powder Met., 17 (1961), 66-88.

55. Fischmeister H.F., Arzt E., "Densification of powders by particle deformation", Powder Met., 26 (1983), 82-88.

56. Lenel F.V., Powder Metallurgy, Principles and Applications, MPIF, Princeton, USA (1980).

57. Fortes M.A., "The Kinetics of Powder Densification Due to Capillary Forces", Powder Metallurgy International, 14 (1982), 96-100.

58. Haynes R., "Mechanical properties of sintered metals", 1981.

59. Karlsson B., Bertilsson I., "Mechanical properties of sintered steels", Scandinavian Journal of Metallurgy, 11 (1982), 267-275.

60. Straffelini, G., V. Fontanari, and A. Molinari. "True and apparent Young's modulus in ferrous porous alloys." Materials Science and Engineering: A 260.1 (1999): 197-202.

61. Chawla, N., and X. Deng. "Microstructure and mechanical behavior of porous sintered steels." Materials Science and Engineering: A 390.1 (2005): 98-112.

62. Bergman, O., & Bergmark, A. (2003). Influence of microstructure on the fatigue performance of PM steels. Advances in Powder Metallurgy and Particulate Materials, (7), 7-270.

63. Andersson, O., & Lindqvist, B. (1990). Benefits of heterogeneous structures for the fatigue behaviour of PM steels. Metal Powder Report, 45 (11), 765-768.

64. Abdoos, H., H. Khorsand, and A. R. Shahani. "Fatigue behavior of diffusion bonded powder metallurgy steel with heterogeneous microstructure." Materials & Design 30.4 (2009): 1026-1031.

65. Engström, U., C. Lindberg, and J. Tengzelius. "Powders and processes for high performance PM steels." Powder metallurgy 35.1 (1992): 67-73.

66. G. Donzella, C. Petrogalli, International Journal of Fatigue 32 (2010) 256-268.

67. C.M. Sonsino, G. Schlieper, and W. J. Huppmann, 'Modern developments in powder metallurgy', Vols. 15–17, 33–48; 1985.

68. C. M. Sonsino et al., 'Modern developments in powder metallurgy', Vols. 18–21,55–66; 1988, Princeton, NJ, MPIF.

69. C. M. Sonsino et al., Int. J. Fatigue, 1992, 14, 3–13.

70. C. M. Sonsino et al., Met. Powder Rep., 1994, 49, 38–45.

71. R. A. Chernenkoff et al., Powder Metall., 1995, 38, 196–200.

72. S. Saritas et al., "Proc. Conf. Euro PM’97", Birmingham, UK, October 1997, EPMA, 196–203.

73. ASM Handbook, "Surface Engineering", Volume 5, 1994.

74. M. Guagliano, L. Vergani, Eng. Frac. Mech., 2004, Vol. 71, pp. 501-507.

75. S. Wang, Y. Li, M, Yao, R, Wang, J. of Mater. Proc. Techno., 1998, Vol. 73, pp. 57-73.

76. H. Guechichi, L. Castex, J of Mater. Proc. Techno., 2006, Vol. 172, pp. 381-387.

77. M. Frija, T. Hassine, R. Fathallah, C. Bouraoui, A. Dogui, Mat. Sci. Eng., 2006, Vol. 426, pp. 173-180.

78. ‘SAE manual on shot peening’, 3rd edn, SAE HS-84, SAE, Warrendale, PA, 1992.

79. ‘Shot peening applications’, Metal Improvement Company Inc., 1997.

80. E. S. Campbell, "Shot peening for improved fatigue properties and stress-corrosion resistance", 1971.

81. J. Champaigne, Shot Peener, 1989, 10, 1–15.

82. Xiao, Hongbin, et al. "The effect of shot peening on rolling contact fatigue behaviour and its crack initiation and propagation in carburized steel." Wear151.1 (1991): 77-86.

83. Guo, Y. B., and A. W. Warren. "The Basic Relationship between Residual Stress Profile Patterns and Fatigue Life of Precision Machined Surfaces in Rolling Contact."

84. ISO 286-1:2010, Geometrical product specifications (GPS) -- ISO code system for tolerances on linear sizes -- Part 1: Basis of tolerances, deviations and fits.

85. ISO 286-2:2010, Geometrical product specifications (GPS) -- ISO code system for tolerances on linear sizes -- Part 2: Tables of standard tolerance classes and limit deviations for holes and shafts.

86. J. F. Archard, Contact and rubbing of flat surfaces, Journal of Applied Physics 24(1953) 981-988

87. I. Metinöz, I. Cristofolini, A. Molinari, " Dry sliding wear behavior of powder metallurgy steels and design criteria", Journal of Powder Metallurgy (in press).

88. F. H. Stott, The role of oxidation in the wear of materials, Tribology International 31 (1998) 61–7.

89. D. A. Rigney, L. H. Chen, M. G. S. Nayr, A. R. Rosenfeld, Wear processes in sliding systems, Wear 100 (1984) 195–219.

90. G. Straffelini, T. M. Puscas, A. Molinari, Identification of Rolling-Sliding Damage Mechanisms in Porous Alloys, Metallurgical and Materials Transactions A (2000) 31A 3091-3099.

91. I. Metinöz, I. Cristofolini, W. Pahl, A. DeNicolo, A. Molinari, " Studio della resistenza alla fatica di contatto di acciai sinterizzati trattati termicamente", La Metallurgia Italiana (in press).

92. H. Danninger et al., Powder Metall. Int. 25 (1993)170.

93. H.E. Exner, D. Pohl, Powder Metall. Int. 10 (1978)193.

94. M. Eudier, Powder Metall. 9 (1962) 278.

95. M.F. Ashby, L.J. Ginson, “Cellular Solids” Pergamon Press (1988).

96. H. Danninger et al., Adv. in Powder Metall. & Part. Mater. 5 (1992) 227.

97. A. Molinari, C. Menapace, E. Santuliana, G. Straffelini, A simplified model for the impact resistance of porous sintered steels, Powder Metallurgy Progress Vol.11, No. 1-2, pp. 12-20, 2011.

98. T. Bell and Y. Sun: Surf. Eng., (1990) vol. 6, pp. 133-42.

7. Publications

7.1 Journals

I. Metinöz, I. Cristofolini, A. Molinari, " Dry sliding wear behavior of powder metallurgy steels and design criteria", International Journal of Powder Metallurgy (in press)

I. Metinöz, I. Cristofolini, W. Pahl, A. DeNicolo, A. Molinari, " Studio della resistenza alla fatica di contatto di acciai sinterizzati trattati termicamente", La Metallurgia Italiana (in press)

I. Metinöz, I. Cristofolini, A. Molinari, " Influence of Ni on dry sliding wear behavior of sintered steels", Journal of Materials Engineering and Performance (accepted)

I. Metinoz, I. Cristofolini, W. Pahl, A. DeNicolo, P. Marconi, A. Molinari, "Theoretical and experimental study of the Contact Fatigue Behavior of a Mo-Cu steel produced by Powder Metallurgy", Materials Science and Engineering (accepted)

7.2 Proceedings

I. Metinöz, I. Cristofolini, A. Molinari, " Dry sliding wear resistance of powder metallurgy steels and design criteria", 6th International Powder Metallurgy Conference and Exhibition, 5-9 October 2011, Ankara, Turkey

I. Metinöz, I. Cristofolini, A. Molinari, " The Effect of Ni on Dry Sliding Wear Behavior of Powder Metallurgy Steels", Advances in Applied Physics and Material Science Congress (APMAS 2012), 26-29 April 2012, Antalya, Turkey

I. Metinöz, I. Cristofolini, A. Molinari, W. Pahl, A. DeNicolo, " Comportamento a fatica di contatto di acciai sinterizzati ad alta resistenza meccanica", 34^o Convegno Nazionale AIM, 7-9 November 2012, Trento, Italy

I. Metinöz, I. Cristofolini, A. Molinari, G. Straffelini, W. Pahl, A. DeNicolo, " The Contact Fatigue Behavior of PM Steels", Euro PM2013 Congress & Exhibition, 15 - 18 September 2013, Gothenburg, Sweden

8. Acknowledgements

First of all I would like to thank to Prof. Ilaria Cristofolini and Prof. Alberto Molinari for their guidance and unconditional support during my PhD study.

I also would like express gratitude to Alessandro DeNicolo, Wolfgang Pahl and Arno Steiner from GKN Sinter Metals for supplying materials and their support in this period.

My special thanks to all with whom I shared my days during this period: Iza for always being there; Marco, Zanza, Nicolò for everything; Thiago, Luiz for being awesome and amazing churrasco and feijoada; Cinzia for the help in the lab and being good! squash opponent; Laci, Judit for the trips that we made together; Melania for trekking on the mountains; Pedro for the sweets and cakes; Anna for trip advices; Nerio, Saliou, Elisa, Giulia, Ketner, Elena, Bisoffi, Faraz for their company and friendship.

Thanks also to Gerti, Elda, Eleonora, Traina, Annalisa, Çağrı, Sinan, John, Fede, Cami, Irina, Daniele and all the others for their valuable friendship.

In addition, thanks to Prof. Pellizzari, Prof. Straffelini, Lorena Maines and Emilio Busana for their advices and helps.

Lastly, I would like to thank my mother Mebrure, father Tahir and brother Cihan for their support. Without them nothing would be possible.

Ibrahim Metinöz

Trento 2014